CLINICAL IMPLEMENTATION OF IMAGE-GUIDED OPTICAL MODELING TOOLS FOR DOSIMETRY IN PANCREATIC CANCER PHOTODYNAMIC THERAPY

A Thesis

Submitted to the Faculty

in partial fulfillment of the requirements for the

degree of

Doctor of Philosophy

by

MICHAEL JERMYN

Thayer School of Engineering

Dartmouth College

Hanover, New Hampshire

December, 2013

Examining Committee:

Chairman_____
Brian W. Pogue

Member_____
Hamid Dehghani

Member_____
Keith D. Paulsen

Member_____
Tayyaba Hasan

_____
F. Jon Kull
Dean of Graduate Studies

Abstract

The goal of this work was to improve the computational tools for near-infrared light modeling for clinical applications in photodynamic therapy (PDT) analysis and eventual treatment planning. The tools to facilitate this modeling were developed in NIRFAST, which is a finite-element based open-source package for modeling near-infrared light transport in tissue for medical applications. It includes full-featured segmentation and mesh creation tools for quickly and easily creating high quality 3D finite-element meshes from medical images, as well as visualization capabilities. These tools were used to determine estimators of treatment response to PDT based on information from contrast CT scans of the pancreas in a retrospective analysis of data from the VERTPAC-01 trial, which investigated the safety and efficacy of verteporfin PDT in 15 patients with locally advanced pancreatic adenocarcinoma. Contrast CT information was used to determine venous and arterial blood content, which was then correlated with necrotic volume as determined from post-treatment CT scans, as well as used to estimate tissue absorption in the pancreas and nearby blood vessels. Light modeling was used to test for correlation between light dose map contours and measured necrotic volume. Both contrast-derived venous blood content and calculated light distribution contours yielded strong correlation with measured necrotic volume, having R^2 values of 0.85 and 0.91, respectively. This indicates that contrast CT can provide valuable information for estimating treatment response to photodynamic therapy, and also indicates that light attenuation is the dominant factor in treatment response, as opposed to other factors such as drug distribution. These R^2 values are much stronger than those

obtained by correlating the logarithm of energy delivered vs. necrotic volume in the VERTPAC-01 trial. This study demonstrates the effectiveness of using computational tools in light modeling for clinical applications, including the development of advanced segmentation, mesh creation, visualization, and modeling algorithms to allow for clinically viable processing. This is the first study to show that contrast CT provides needed surrogate dosimetry information to predict treatment response in a manner which uses standard-of-care clinical images, rather than invasive dosimetry methods.

Acknowledgements

I would like to thank all of my committee members for their efforts in guiding and supporting this research as well as my own academic development and wellbeing. My advisor, Brian Pogue, has always been insightful, helpful, motivating, and has encouraged me to be creative in my research endeavors. I hold this sort of creativity in high regard, and his support has been indispensable. Dr. Pogue has also provided advice based on his considerable experience in the field to ensure that the overall significance of a particular component of this research is considered carefully in the context of optics in cancer research. Hamid Dehghani has a great deal of knowledge in the areas of near-infrared light modeling and computational methods for optical tomography. His input and advice to this research have been significant, particularly in helping bridge my comfort in math/computer science over to the physical and biological aspects of light modeling. Keith Paulsen similarly has considerable experience in computational methods and modeling, proving to be an invaluable resource in this research. Tayyaba Hasan is an expert in the field of photodynamic therapy, and I am very thankful for her guidance and input over the course of my time at Thayer. The Optics in Medicine Laboratory at Dartmouth College has greatly assisted in the success of my research endeavors. I would also like to express gratitude to my family, for their constant support of my efforts.

This work has been funded by P01 CA84203 (T. Hasan, B. Pogue, M. Jermyn), RO1 CA132750 (B. Pogue, H. Dehghani, S. Davis, M. Jermyn), Department of Defense award W81XWH-09-1-0661 (S. Davis), and a Neukom Graduate Fellowship (M. Jermyn).

Table of Contents

List of Tables

List of Figures

Figure 29. (a) A single cropped section of the contrast CT scans showing the beam-hardening artifact caused by the biliary stent. The bidirectional red arrows indicate measurement locations affected by the artifact and unaffected by the artifact. (b) The grayscale bias of the stent artifact at different vertical positions in the image.

Figure 30. (a) A single axial DICOM slice around the pancreas is shown. Bright areas are contrast enhanced major blood vessels, while the dark areas in the top left and right are air. The remaining area is pancreas tissue or surrounding tissue. (b) Segmentation of the pancreas area into tissue types. Blue is pancreatic tissue, red indicates blood vessels, and black is air.

Figure 31. The NIRFAST interface for segmenting medical images into different tissue types, for use in creating the 3D tetrahedral mesh used for light modeling. The top left view shows a 3D volume rendering of the medical images, while the other three views show the 2D orthogonal views of the segmentation overlaid on the medical images. On the left menu are the various tools used for segmentation and image processing.

Figure 32. The NIRFAST interface for creating a 3D tetrahedral mesh from a stack of 2D segmentations. There are parameters for controlling element size, quality, and surface facet attributes.

Figure 33. The NIRFAST interface for defining the light source attributes. A custom module 'pdt_fiber' was created specifically for modeling the light-emitting fiber used in the VERTPAC-01 study.

Figure 34. (a) A single axial DICOM slice of the pancreas and surrounding tissue is shown from the pre-treatment contrast CT scans. Bright areas are indicative of contrast enhanced major blood

vessels, while the dark areas in the top left and top right are air. (b) Segmentation of the same axial slice into different regions based on tissue type: blue is pancreatic or surrounding tissue, red is blood vessels, and black is air. (c) Rendering of a 3D tetrahedral mesh of the pancreas and surrounding tissue in blue, and blood vessels in red. It is clipped by a plane to visualize the interior of the mesh.

Figure 35. The NIRFAST interface for modeling near-infrared light transport in tissue.

Figure 36. (a) A single axial slice of the pancreas from the post-treatment CT scans, indicating the dark area in the center as necrotic tissue. The two bright rings are biliary stents. (b) The same slice showing the segmentation of the necrotic tissue in pink. (c) A volume rendering of the segmentation of the necrotic volume. (d) The volume of the necrotic tissue region is shown for each patient in the study, as determined from the segmentation of the post-treatment CT scans. Energy delivered per cm of fiber size is shown for each patient. Note that 2 fibers were used for patient 16, and 3 fibers for patient 15. Each of the fibers for patient 15 were 2cm in length as opposed to the 1cm norm. Necrotic volume for patient 12 could not properly be measured due to pre-existing necrosis prior to treatment.

Figure 37. (a) Correlating necrotic volume with venous blood content, as derived from the contrast CT scans. (b) Necrotic volume is normalized as V/(n*d*log(E)), where V is the necrotic volume in cm^3, n is the number of fibers used in treatment, d is the fiber size in cm, and E is the energy delivered over the fiber in J/cm. This is then correlated with the contrast derived venous blood content.

Figure 38. (a) A single axial slice of the pancreas from the pre-treatment CT scans is overlaid with computed contours of light fluence levels around the fiber location. This was simulated using blood content information for tissue absorption from contrast CT. (b) The fluence of the light-

emitting fiber in a volume rendering of the area around the fiber in the pancreas, identifying major blood vessels.

Figure 39. Correlating actual necrotic volume with the estimated necrotic volume from light modeling, using absorption values estimated from contrast CT information and literature values for scattering. A particular energy threshold, $0.003 J/cm^3$, with the highest correlation was picked to determine the estimated necrotic volume using the contour defined by this threshold.

Figure 40. The effect of a nearby blood vessel on the light fluence field produced from light modeling. (a) Diagram of the relative locations of the blood vessel, light-emitting fiber, and point of measurement in the light fluence field. (b) Relative effect on the light fluence field, as compared with the light fluence unperturbed by the presence of a blood vessel.

Figure 41. The effect of optical heterogeneity on estimated necrotic volume, as compared with optical homogeneity. The observed heterogeneity specifies the range of expected optical heterogeneity, as determined from the pre- and post-contrast CT scans of the 15 patients.

Figure 42. The effect of the absorption value used for optical simulation on estimated necrotic volume, as compared with a representative absorption value for the patients of $0.087 mm^{-1}$.

Figure 43. The effect of the reduced scatter value used for optical simulation on estimated necrotic volume, as compared with a literature-based reduced scatter value of $0.5 mm^{-1}$ in pancreatic tissue and $0.98 mm^{-1}$ in blood vessels. The expected error range indicates the range of values found in literature for the pancreas for reduced scattering.

Figure 44. The effect of the venous oxygen saturation value used for optical simulation on estimated necrotic volume, as compared with a literature-based value of 70%. The expected error range indicates the range of values found in literature for venous blood oxygen saturation.

Figure 45. Correlating necrotic volume with venous grayscale values, as obtained from the post-contrast CT scans. Necrotic volume is normalized as V/(n*d*log(E)), where V is the necrotic volume in cm^3, n is the number of fibers used in treatment, d is the fiber size in cm, and E is the energy delivered over the fiber in J/cm.

Figure 46. Correlating necrotic volume with venous grayscale values, as obtained from the post-contrast CT scans. Venous grayscale values are normalized by the grayscale values in a major blood vessel. Necrotic volume is normalized as V/(n*d*log(E)), where V is the necrotic volume in cm^3, n is the number of fibers used in treatment, d is the fiber size in cm, and E is the energy delivered over the fiber in J/cm.

List of Acronyms

Photodynamic Therapy	PDT
Computed Tomography	CT
Magnetic Resonance Imaging	MRI
Diffuse Optical Tomography	DOT
5-aminolauvulinic acid	ALA
Near-infrared	NIR
Three Dimensional	3D
Deoxyribonucleic Acid	DNA
Eastern Cooperative Oncology Group Scale	ECOG

1. Introduction

This thesis focuses on the development and implementation of image-guided optical modeling software as a tool to analyze photodynamic therapy dosimetry. The exact application studied here was a light-activated treatment for pancreatic cancer, called photodynamic therapy. This introduction reviews the pertinent aspects of this particular cancer and the treatment planned, in the context of software tools to help analyze the results of a clinical trial.

Pancreatic cancer is the fourth leading cause of cancer-related death in the United States [1], with an estimated 37,390 deaths from the disease in 2012. The overall 5-year survival rate is estimated at 5.8%, and treatment options are limited, with surgical removal as an option for only 15% of patients [2]. Patients unable to undergo surgery are generally treated with chemotherapeutics which offer marginal improvements in survival, and thus an urgent need exists for alternative strategies to treat pancreatic cancer more effectively.

Photodynamic therapy (PDT) is a minimally invasive and nontoxic method of treating cancer using the interaction of light and a photosensitizer, in the presence of oxygen, to kill tumor cells [3]. A photosensitizer is a drug, usually injected intravenously, that is activated by a specific wavelength of light. Activation produces singlet oxygen from molecular oxygen which in turn causes necrosis [4]. There is also indirect cell death caused by induced hypoxia through tumor vasculature damage. Since the effect is photochemical, rather than thermal, there is no significant damage to connective tissues [5]. Despite the advantages of photodynamic therapy, the lack of effective treatment

response estimators has limited the viability of this treatment method. Validating light delivery and treatment response given limited access to the pancreas presents a significant challenge. Information garnered from contrast CT provides the opportunity for pre-treatment planning in order to address this issue. The means of determining this information, as well as the clinical study details will be described in this work.

Computational tools in light modeling provide the opportunity to assist in pre-treatment planning. Tools have been developed on an open-source platform, creating a full user workflow for modeling near-infrared light transport, starting from medical images, through tissue segmentation, finite-element mesh creation, source/detector modeling, light propagation modeling through biological tissue, and visualization of the optical solution. Multi-modal approaches which combine near-infrared light modeling with conventional imaging modalities represent a prevailing trend. These approaches typically involve applying anatomical templates from MRI/CT/US images to light modeling. However, merging these data sets using current technology requires multiple software packages, substantial expertise, significant time-commitment, and often results in unacceptably poor mesh quality for optical modeling, a reality which represents a significant roadblock for translational research of multi-modal near-infrared light modeling.

This work addresses these challenges directly by introducing automated DICOM image stack segmentation and a novel one-click 3D mesh generator optimized for multi-modal NIR imaging, and combining these capabilities with near-infrared light modeling tools into a single software package (available for free download) with a streamlined

workflow. The application of these tools is demonstrated in the use of near-infrared light modeling for dosimetry in photodynamic therapy of the pancreas.

Pieces of this work have already been published or submitted in peer reviewed journals, and so some of the text is drawn from these. In particular, components of the following chapters correspond to these papers:

Chapter 3:

Jermyn M., Ghadyani H., Mastanduno M.A., Turner W., Davis S.C., and Pogue B.W., "Fast segmentation and high-quality three-dimensional volume mesh creation from medical images for diffuse optical tomography," J. Biomed. Opt. 18(8), 086007 (August 12, 2013), doi: 10.1117/1.JBO.18.8.086007.

Chapter 4:

Jermyn M., Davis S.C., Dehghani H., Huggett M.T., Hasan T., Pereira S.P., Bown S.G., Pogue B.W., "CT contrast predicts pancreatic cancer treatment response to verteporfin-based photodynamic therapy," [Submitted for review].

Jermyn M., Davis S.C., Dehghani H., Huggett M., Hasan T., Pereira S.P., and Pogue B.W., "Photodynamic therapy light dose analysis of a patient based upon arterial and venous contrast CT information," SPIE Proc., vol. 8568-10 (2013) [Conference proceeding].

2. Background

2.1 Light-tissue interaction

There are a variety of different research areas and applications of the use of light in biological tissue, for disease treatment and imaging. When tissue is irradiated with light, it can result in absorption, scattering, reflection, and transmittance. This section will describe some of the basic concepts of light-tissue interaction, in the context of near-infrared optics.

2.1.1 Absorption

An absorption event occurs when the energy difference between two energy levels in a molecule match the incident photon energy. This is made possible because the frequency range of oscillation in the near-infrared part of the electromagnetic spectrum (650-900nm) is similar to the vibration frequencies of atoms and molecules. This allows energy transfer from the light radiation field to the molecule. The increased vibration amplitude will usually be lost in the form of heat via collisions with other particles. The term chromophore is used to describe a light-absorbing molecule. Due to the absorption spectra of the primary chromophores in biological tissue, near-infrared light is able to penetrate greater depths of tissue. Absorption causes increased attenuation - the reduced intensity of light propagating through tissue. The effect of optical absorption on attenuation is described by the Beer-Lambert law:

$$I/I_0 = 10^{-\alpha d} \quad (1)$$

I is the intensity of transmitted light, I_0 is the intensity of incident light, α is the absorption coefficient of the tissue, and d is the light path length. So there is a logarithmic relationship between light transmission and the absorption coefficient.

2.1.2 Scattering

A photon beam incident on biological tissue will be partially reflected by scattering, including specular reflection from the surface of the tissue as well as internal scattering. Optical scattering causes attenuation of the beam, due to reflection/refraction between tissue types with different refractive indices, re-radiation of absorbed photons in a new direction at the same wavelength, and reflection of photons by molecules in tissue. This re-emitting of photons is elastic, in that no energy is lost but the direction is changed. Biological tissue illuminated by near-infrared light is a case in which there is multiple scattering, leading to more complex models of light transport. In a homogeneous medium, the scattering coefficient μ_s is given by:

$$\mu_s = \int_{4\pi} d\mu_s(\hat{s}, \hat{s}')d\hat{s}' \quad (2)$$

Here $d\mu_s(\hat{s}, \hat{s}')$ is the differential scattering coefficient describing the probability of a photon in original direction $\hat{s}$ scattered in a new direction $\hat{s}'$. This assumes that scattering is independent of the incident photon angles. A construct for normalizing the differential scattering coefficient is found in the scattering phase function $f(\hat{s}, \hat{s}')$:

$$f(\hat{s}, \hat{s}') = d\mu_s(\hat{s}, \hat{s}')/ \mu_s \quad (3)$$

The anisotropy factor g, describing the relative directional bias of optical scattering, is given by:

$$g = \int_{4\pi} f(\theta)\cos(\theta)d\hat{s}' \quad (4)$$

Here θ is the angle between ŝ and ŝ'. Isotropic scattering is equivalent to a value of 0 for g. A higher value of g, closer to 1, corresponds to a more forward biased scattering profile. The assumption of isotropic scattering is made by the application of diffusion theory to modeling near-infrared light transport in tissue. The reduced scattering coefficient (often referred to as simply the scattering coefficient) μ_s' is given by:

$$\mu_s' = (1 - g)\ \mu_s \quad (5)$$

2.2 Near-Infrared light modeling

Diffuse optical tomography is a non-invasive means of functional imaging for tissue. Near infrared light (650-900nm) is used to detect soft tissue lesions, by measuring functional tissue parameters such as blood oxygen saturation, water content, and lipid concentration [6]. The functional information provided by near infrared imaging gives it the potential to be useful for detecting breast cancer [7], imaging brain function [8], and small animal imaging [9]. Optical fibers are typically used to inject the light into the tissue, and the resulting measurements are then obtained via detectors such as charged coupled devices. The measured data is then used to reconstruct the optical properties of the tissue. There are two notable problems to be addressed:

1. The Forward Problem: Given a light source distribution q in a domain Ω, and the tissue optical properties p in Ω, find the light fluence and the resulting boundary data y.

2. The Inverse Problem: Given a light source distribution q in a domain Ω, and the boundary data y, find the tissue optical properties p in Ω.

The forward problem will be the focus of discussion, due to its application in providing dosimetry information for photodynamic therapy. The radiative transport equation describes the propagation of radiation through a medium, as influenced by absorption, scattering, and anisotropy. It is given by:

$$\left\{\hat{\boldsymbol{s}}\cdot\nabla+\mu_{\mathrm{a}}(\boldsymbol{r})+\mu_{\mathrm{s}}(\boldsymbol{r})+\frac{\partial}{c\partial t}\right\}I(\boldsymbol{r},\hat{\boldsymbol{s}},t)= q(\hat{\boldsymbol{s}},\hat{\boldsymbol{r}},t)+\mu_s(\boldsymbol{r})\int(f(\hat{\boldsymbol{s}}',\hat{\boldsymbol{s}},\boldsymbol{r})I(\hat{\boldsymbol{r}},\hat{\boldsymbol{s}}',t))\mathrm{d}^2\hat{\boldsymbol{s}}' \tag{6}$$

where $I(r,\hat{s},t)$ is the radiance at time t at position r in direction $\hat{s}$, $q(r,\hat{s},t)$ is the source term, μ_a and μ_s are the absorption and scattering coefficients, c is the speed of light, and $f(\hat{s}',\hat{s},r)$ is the scattering phase function [10]. The absorption and scattering coefficients determine the likely depth of penetration of light into a medium before an absorption or scattering event occurs. Analytic models can provide direct solutions to this equation for some geometries, however for more complex geometries other modeling techniques are

required. Statistical models such as Monte-Carlo methods can be used for complex geometries, and with sufficient photon counts and fine resolution in geometry can give very accurate results. However the very long computational time makes these techniques prohibitive for most applications. For diffuse optical tomography, we can use the diffusion approximation to the radiative transport equation:

$$\frac{1}{c}\frac{\partial \Phi(\boldsymbol{r},t)}{\partial t} - \nabla \cdot \Phi(\boldsymbol{r})\nabla\kappa(\boldsymbol{r},t) + \mu_{\mathrm{a}}(\boldsymbol{r})\Phi(\boldsymbol{r},t) = q_0(\boldsymbol{r},t) \tag{7}$$

where $q_0(r,t)$ is an isotropic source, $\Phi(r)$ is the photon fluence rate, and $\kappa = 1/3(\mu_a + \mu_s')$ is the diffusion coefficient [10]. The approximation operates on the assumption that the optical source is isotropic, which is valid for large source-detector separations due to the dominance of scattering over absorption in tissue [6]. A further assumption is made that detector times must not be too soon after input times. The approximation is used because it provides a much more tractable problem computationally. The time-domain diffusion equation can be Fourier transformed to give the frequency-domain diffusion equation:

$$-\nabla\kappa(\boldsymbol{r})\nabla\hat{\Phi}(\boldsymbol{r},\omega) + \left(\mu_{\mathrm{a}}(\boldsymbol{r}) + \frac{\mathrm{i}\omega}{c}\right)\hat{\Phi}(\boldsymbol{r},\omega) = \hat{Q}_0(\boldsymbol{r},\omega) \tag{8}$$

where ω is the modulation frequency [10].

To solve the forward problem, a finite-element based method can be used. By taking the Galerkin formulation of the diffusion equation, a matrix equation can be derived and subsequently solved for the photon fluence and resulting boundary data.

2.2.1 Imaging with near-infrared light

Diffuse optical tomography (DOT) is a volumetric optical imaging technique which relies on modeling light transport in tissue using the diffusion approximation which is generally applicable in scatter dominated systems. The spectral measure of the diffuse transport of near-infrared light through soft tissue can provide the ability to image functional tissue information such as hemoglobin oxygenation and water fraction, which can be useful as a non-invasive means of identifying cancer [11-13]. This method has also been proved successful by the use of luminescence probes using for example, fluorescence markers to allow quantitative molecular imaging of functional exogenous reporters [14,15]. The spectral characteristics of biological tissue in the near-infrared region can help in the diagnosis of malignant tissue from healthy tissue. In particular, hemoglobin has been shown to be an effective parameter for diagnosis in optical breast imaging. Near-infrared imaging uses non-ionizing light which provides a further advantage over some conventional imaging modalities such as CT. DOT works by delivering near-infrared light (typically between 600 and 1000nm) to multiple locations on the surface of the domain, and measuring the intensity detected at locations on the surface. These measurements of reflection and/or transmission can be used to reconstruct the distribution of optical properties within the domain. Due to the fact that biological tissue is highly scattering, light transmission is significantly reduced. The dominant scattering also creates the need for complex reconstruction algorithms. Another disadvantage of DOT is the generally poor spatial resolution. There are many advantages of DOT over other imaging modalities, including its relative cost, ability to produce clinically relevant functional information, and safety. However, the computational tools available for DOT

have historically lacked the ability to encompass the entire light modeling workflow, from medical images to the visualization of optical solutions. Robustness and numerical issues have further made DOT unreliable and only accessible to expert users. The work presented in chapter 3 of this thesis outlines advances made in providing the computational tools needed to improve the usability of near-infrared light modeling for clinical applications.

2.3 Cancer & treatment options based upon light delivery

Light delivery is used for some forms of cancer treatment, and so a brief review of treatment options and the particular cancer treated here is outlined. Cancer is a disease which causes abnormal cell growth and division. It is the second leading cause of death in the United States [16]. In a process called metastasis, cancer cells can spread throughout the body through the blood and lymphatic systems. Cancer development is initiated by exposure to carcinogens such as harmful chemicals, microbial varieties, viruses, and sources of ionizing radiation. This exposure can cause cell damage by means of DNA mutations, leading to uncontrolled cell division and growth. Carcinoma describes cancers beginning in the skin or boundary tissue of organs. Sarcoma describes cancers beginning in connective or supporting tissues. Leukemia describes cancers beginning in blood-forming tissues. Lymphoma describes cancers beginning in the immune system of the body. Nervous system cancer describes cancers beginning in the spinal cord or brain.

Treatment options depend on the type, location, and stage of the disease. These options include chemotherapy, radiotherapy, surgery, immunotherapy, photodynamic therapy, hyperthermia, and more. Chemotherapy uses anticancer drugs to eliminate cancer cells or inhibit cancer cell growth. These drugs are often preferentially taken up by cancer cells, allowing for selectivity in treatment. This treatment method is often used in conjunction with surgery, either by reducing tumor size to make resection more viable or to decrease relapse rates post-surgery. It can also be used to relieve some of the symptoms associated with various forms of cancer to improve quality of life in patients. Chemotherapy has the potential to cause healthy tissue damage, and drug resistance can significantly hamper its efficacy. Radiotherapy uses ionizing radiation to kill cancer cells by damaging the DNA, in an effort to inhibit cell growth and division among cancer cells. The lack of selectivity means that healthy cells will also be damaged; however healthy cells can often recover from this damage to function normally. This treatment method can be used in much the same way as chemotherapy, either pre-operatively to reduce tumor size or post-operatively to decrease the chance of recurrence. Radiotherapy is largely ineffective against tumors with hypoxic regions because of their resistance to ionizing radiation. Surgery is the most common method of treatment, particularly for solid tumors, involving the removal of the tumor and sometimes surrounding tissue/organ. It is often used to diagnose the cancer type, stage, and location as well. Solid tumors can be cured using surgery if there is complete removal; however recurrence from residual tumor cells is a possibility. Furthermore, metastatic cancers can be impossible to remove fully using surgery, and the surgery itself carries its own risks.

2.3.1 Pancreatic cancer

Pancreatic cancer is most often found in the form of an adenocarcinoma, and has one of the worst 5-year survival rates among cancer types. It is seldom detected early due to the lack of early symptoms, which is a major contributing factor to the poor survival rate. Later symptoms include jaundice, discolored urine/stool, abdominal pain, loss of weight/appetite, and fatigue. A common reason for surgery not being an option in patients with pancreatic cancer is tumor involvement of major blood vessels, including the superior mesenteric and portal veins [17]. Pancreatic tumors are often resistant to treatment methods such as chemotherapy and radiotherapy.

2.3.2 Phototherapy, photochemotherapy & photodynamic therapy

Phototherapy is the use of light for therapeutic functions, and has been used historically for a variety of medical conditions including cutaneous tuberculosis, seasonal affective disorder, jaundice, dermatological issues, and more. Phototherapy involves the direct interaction of light and tissue without the effect of a photosensitive drug. The light can be administered using diodes, lasers, and various types of lamps. The most common applications for this type of treatment are dermatological, such as psoriasis, acne, and eczema. The treatment of skin conditions can be accomplished either by directed phototherapy to a specific location on the skin, or by non-targeted phototherapy. Light therapy has also proven to be an effective treatment for seasonal affective disorder, by using light boxes to ameliorate the negative mood effects caused by low sunlight seasons.

Photochemotherapy is the use of light therapy to treat tissue with an exogenous agent sensitizing the tissue. An application of photochemotherapy is the dermatological

light treatment method using ultraviolet irradiation with psoralens, for psoriasis and other conditions.

Photodynamic therapy (PDT) is a type of photochemotherapy, which describes treatment using an exogenous sensitizing agent and irradiation. In PDT, there is the additional dependence on the presence of oxygen in the treatment region. The use of photodynamic therapy to induce cell death based on the interaction of light and photosensitive chemicals originates from the medical student Oscar Raab [18], and the potential medical applications of this were first described by Tappeiner and Jesionek [19]. PDT is a non-invasive technique which is used to treat a variety of cancer tumor types, including cancers of the prostate, bladder, head and neck, skin, and lung. It also has applications in non-cancer conditions such as macular degeneration and psoriasis. In age-related macular degeneration, PDT can reduce the rate of vision loss in adults and can treat more cases than the previous standard of treatment (photocoagulation). There are further applications of PDT in treating local viral diseases and dermatological conditions such as acne. In addition to direct cell death, PDT can cause vascular and blood vessel damage, as well as inciting the immune system, all of which can help inhibit tumor growth. A potential side effect of PDT is temporary photosensitivity following treatment. It is a treatment method which can be used in conjunction with other therapies such as surgery, chemotherapy, and radiotherapy.

2.3.3 Photosensitizers

A photosensitizer is a molecule which reacts with light of a particular wavelength by absorbing a photon and thereby reaching an excited singlet state. Many types of tumors

preferentially accumulate certain photosensitizers, as compared with surrounding tissue, which can improve the effectiveness of photodynamic therapy. A photosensitizer will ideally have low toxicity, high selectivity to tumor tissue, easy elimination from the body, efficient singlet oxygen production, and absorption in the red/near-infrared light region to allow for deep tissue penetration of light. Eosin was used as a photosensitizer in 1900 to treat epilepsy, which was the first reported use of a photosensitizer in humans [20]. It was discovered to cause dermatitis, which resulted in its subsequent use for treating skin tumors [19]. Hematoporphyrin was first used as a photosensitizer in 1911 for in vitro studies of paramecium and red blood cells, as well as to study its affect in light treatment of mouse skin [21]. In 1948 the tumor-localization of porphyrins was investigated for tumor diagnosis and treatment [22]. The porphyrins are a group of organic compounds which have proved to have desirable qualities for photosensitization. When hematoporphyrin derivative was developed, and its purified form (Photophrin®), consistent response was reported in human tumor treatment using hematoporphyrin derivative-based photodynamic therapy in 1978 [23]. The approved applications of first-generation photosensitizers such as Photophrin® were limited due to the risk of photo-toxic reactions. Second-generation photosensitizers such as 5-aminolauvulinic acid (ALA), benzoporphyrin derivatives, and chlorins have since been developed which are highly selective and safe. Verteporfin is a benzoporphyrin derivative photosensitizer with a number of applications, including use for treating macular degeneration and malignant melanoma. Its absorption peak is at 690nm, a wavelength which allows for increased light penetration in biological tissue. This increases the suitability of the photosensitizer to the lesions of pancreatic cancer [24]. An advantage of Verteporfin over the first

generation photosensitizers is its rapid clearance via excretion in bile, which makes it a much more attractive choice for photodynamic therapy. The usual period of photosensitivity is 24 hours, and Verteporfin reaches its peak concentration much faster, within 30-60 minutes of being administered. This makes the timing easier for treatment protocol, and decreases the period of time post-treatment during which patients must avoid bright sunlight. Verteporfin-based photodynamic therapy has been shown to be effective at causing cell death when there has been sufficient diffusion and permeation of the photosensitizer in the tumor tissue [25, 26]. Given the close relationship between photosensitizer distribution and permeation, light dose, and treatment response in photodynamic therapy, there is significant value in finding effective dosimetry methods.

2.3.4 Dosimetry

There is a thresholding effect in photodynamic therapy for causing cell death, based on the number of photons absorbed by the photosensitizer [27]. A sharp transition between the necrotic and normal tissue has been observed in the liver using second generation photosensitizers, the boundary being defined by Evans Blue dye-exclusion. This boundary indicates the existence of a minimum concentration of singlet oxygen needed to cause necrosis. This in turn suggests a minimum threshold for light dose and photosensitizer concentration. It is not plausible to measure this threshold value accurately *in vivo*, due to the complexity of tissue optics and the amount of heterogeneity. The threshold value has been measured in largely homogeneous tissue regions. One study investigated the threshold values in rabbit intracranial tissue for several photosensitizers (Photofrin, 5-animolevulinic acid-induced Propoporphyrin IX, Tin Ethyl Etiopurpurin,

and chloroaluminum phthalocyanine) [28]. There have also been measurements in C26 colon carcinoma of mice, using Photofrin, 5-animolevulinic acid-induced Propoporphyrin IX, and chlorin e_6 [29]. Another study investigated the rat liver, using Photofrin and monosulfonated aluminum chlorophthalocyanine [30]. For in vivo work in heterogeneous tissue, effective dosimetry methods are needed. The gold standard for estimating the effectiveness of photodynamic therapy is singlet oxygen detection. When singlet oxygen returns to the ground state, a weak phosphorescence signal is emitted at 1270nm. However singlet oxygen detection is technically challenging due to the weak signal of singlet oxygen emission, caused by the low radiative rate in biological tissue and the short lifetime. This problem of low quantum yield is compounded by the difficulty in distinguishing the singlet oxygen emission signal from other sources of emission. Therefore there is motivation for technically feasible dosimetry methods in photodynamic therapy.

The degree of necrosis is determined partly by photosensitizer dose and distribution, light dose, and tissue oxygenation [31]. When necrosis is achieved, the threshold effect creates a sharp boundary to the necrotic region [32, 33]. A major hindrance in identifying the appropriate threshold value is the lack of *in vivo* light dosimetry information, due in part to the difficulties associated with finding consistent tissue optical properties [3]. Furthermore, there are vital structures very close to the pancreas such as the stomach, major blood vessels, biliary tree, and duodenum. Although necrosis has been shown to heal safely in some of these structures, there is a potential risk of significant complications [17]. Thus it would be valuable to provide an estimator for patient treatment response to photodynamic therapy based on the threshold of necrosis,

with the intent of informing treatment parameters to achieve improved treatment outcomes. The notion of planning treatment based solely on photosensitizer and light dose does not account for differences due to optical properties in the tissue and heterogeneity, particularly with regard to high attenuation from blood content. Blood volume can greatly change the optical absorption in a region of interest due to the presence of oxyhemoglobin. Thus there is significant improvement that can be made to clinical dosimetry methodology, by accounting for variation among patients in optical properties as described in this work. The clinical state of photodynamic therapy can greatly improved by the development of dosimetry methods which show high correlation with treatment response.

3. NIRFAST: a custom tool for near-infrared light modeling

The advent of using light modeling to give surrogate dosimetry information in photodynamic therapy requires extensive computational capabilities in optics that have been previously unavailable in a single comprehensive package. In particular, there is significant need for innovative tissue segmentation, image processing, and mesh creation algorithms which incorporate image-guidance from other modalities into the light modeling process using modality-specific contrast characteristics. Exploiting the contrast profile details of image guidance from MR, CT, US, and other modalities for clinical application requires novel methods that are capable of automation. This chapter presents tools developed which achieve this goal. The computational packages available for near-infrared light modeling have only provided certain components of the light modeling

workflow, rather than encompassing the entire process. Furthermore, the segmentation and mesh creation tools available have suffered from poor robustness to the variety of contrast profiles and imaging domains used in optical modeling. In this work, an integrated and freely available software package is outlined and tested which allows users to go all the way from import of standard DICOM images (and other related formats) to segmentation and meshing, through to light simulation and property recovery. These tools include innovative algorithms for handling the image processing and modeling needs specific to optical modeling problems.

Image-guided diffuse optical tomography is very dependent on the ability to easily produce high quality 3D volume meshes from medical images, and the process of mesh creation is a significantly underappreciated but complex issue, which is directly solved in many cases by software such as this. There are various mesh creation tools available either commercially or freely, but each has its own limitations in application to optical tomography. For example, MeshLab is an open source tool for creating unstructured 3D triangular meshes, but has no semi-automated segmentation routines [34], and is also lacking some workflow features such as the ability to undo the last action. Mimics is a commonly used commercial package designed for medical image processing, but mesh creation requires a great deal of manual input, and it has difficulty with multiple-region problems [35]. Netgen is a freely available 3D tetrahedral mesh generator, but has limitations with multiple-region problems [36]. Some other mesh creation tools include DistMesh [37], iso2mesh [38], and QMG [39], but these are not linked to segmentation tools per se. In this work, novel methods have been developed for advanced segmentation of tissue types and 3D tetrahedral mesh creation from medical

images. Segmentation is used to identify boundaries of organs and different tissue types in medical images, for use in creating geometric representations to use in light modeling. Previously, generic segmentation and meshing algorithms have been used to handle complex tissue contrast profiles. Region growing is a frequently used segmentation method which uses seed points and analyzes nearby pixels for inclusion in the region based on relative grayscale value [80]. Edge detection is often used to determine tissue regions based on the sharp transition in grayscale value at the interfaces between regions [81]. Level set methods represent the contours corresponding to tissue boundaries as a signed function, and asses the function for its best match to the image [82]. All of the commonly used segmentation methods have drawbacks when approaching problems with indistinct boundaries, high noise, intricate multi-part geometries, and other contrast profile characteristics commonly found in medical images. The application of these algorithms has proved insufficient in many cases due to these types of specific contrast details. For example, in small animal MR imaging there are frequently different tissue regions, such as the brain and surrounding tissue, which have similar grayscale values and indistinct boundaries which are only easily discerned visually. In MR breast imaging the skin and glandular tissue often have this same issue, and the glandular tissue can consist of numerous disjoint parts of extreme geometries. Additionally MR images contain low frequency gradients, forming bright areas and dark areas in different sections of the image. These types of problems make the use of conventional algorithms like watershed, thresholding, and region growing very difficult. The usability of light modeling in clinical applications is dependent on creating advanced segmentation methods capable of handling complex contrast profiles, and thereby automating the

image processing needs. The algorithms described in this Chapter are innovations which address this need. These include new methods for defining and handling noise/holes in tissue segmentations, which previously was managed using basic morphological operations such as erosion and dilation based algorithms. Multi-region problems require more advanced solutions to ensure complete noise removal and avoid misclassifying tissue types. Also included is a technique for automatically identifying the skin layer in medical images, for removal or inclusion in modeling at the user's discretion. This is essential in applications where the skin layer may be mistakenly classified with another tissue type due to indistinct boundaries, poor contrast, or similar grayscale value ranges. This is the first existing technique to handle skin identification in medical image contrast profiles such as breast MR imaging. Previously, skin segmentation had to be done manually in these situations, often taking many hours and thus being prohibitive to clinical translation. The new methods presented in this work demonstrate a significant advancement in segmentation and meshing algorithms for improving the viability of clinical optical modeling.

Although optical modeling can be done stochastically, using Monte Carlo simulation packages such as MCML [40], the computational time needed is often prohibitive to use. There are several software packages which model near-infrared light transport using the diffusion approximation to the radiative transport equation. TOAST is a free package designed for image reconstruction in diffuse optical tomography, but does not include tissue segmentation or advanced 3D mesh generation tools [41]. NAVI is a software package used for FEM modeling, but has no tissue segmentation capability [42]. There are also commercial packages such as COMSOL Multiphysics (previously

FEMLAB) [43]. There is no freely available tool that incorporates all of the workflow elements needed for segmentation and mesh creation in optical tomography in a seamless manner. The new tools in NIRFAST help to address these issues, and in this study, their capabilities are tested and quantified in a series of cases which are representative of key application areas. Since the core FEM code of Nirfast is based in MATLAB, this has in the past hindered its ability to allow for easy coupling to highly complex 3D meshing tools. One issue stems from the inability of MATLAB to efficiently visualize large 3D meshes, while another issue is the necessity for custom image processing tools when dealing with an assortment of different medical image types and formats. Using a VTK/ITK based platform which itself is an open source application for segmentation & meshing has helped to address these issues by providing a seamless coupling within Nirfast. Providing new image processing and modeling methods, with the workflow needed to create an FEM mesh from a variety of different types of medical images, and seamlessly using this mesh for light transport modeling are essential to making DOT accessible and useful.

3.1 Open-source light modeling package

The software tool developed at Dartmouth College and University of Birmingham, UK, called NIRFAST, is a finite-element based package for modeling near-infrared light transport in tissue for medical applications [6, 44]. It is open source, free, and cross platform as developed under MATLAB (Mathworks Inc.) which also allows user-friendly understanding and modifications. Applications of NIRFAST are diverse, including

optical modeling for small animal molecular imaging [45-48], optical imaging for breast cancer [49], and brain functional imaging based upon vascular dynamics [11, 50]. NIRFAST is kept under publicly accessible version control (http://nirfast.googlecode.com), with a submission system to encourage collaborations and contributions from the NIR community. In an effort to extend the user base of these tools, workshops have been run at the OSA Biomed conference (Miami, FL), the Thayer School of Engineering at Dartmouth College (Hanover, NH), and SPIE Photonics West conference (San Francisco, CA). These workshops serve to provide instruction in the use of NIRFAST, as well as obtaining useful feedback for improvements/changes and the future direction of NIRFAST.

3.2 Seamless light modeling workflow

NIRFAST incorporates tools for segmentation, fiducial placement, meshing, modeling, and visualization. Figure 1 shows a map of the toolboxes and capabilities in NIRFAST, illustrating many of the developments described in this work.

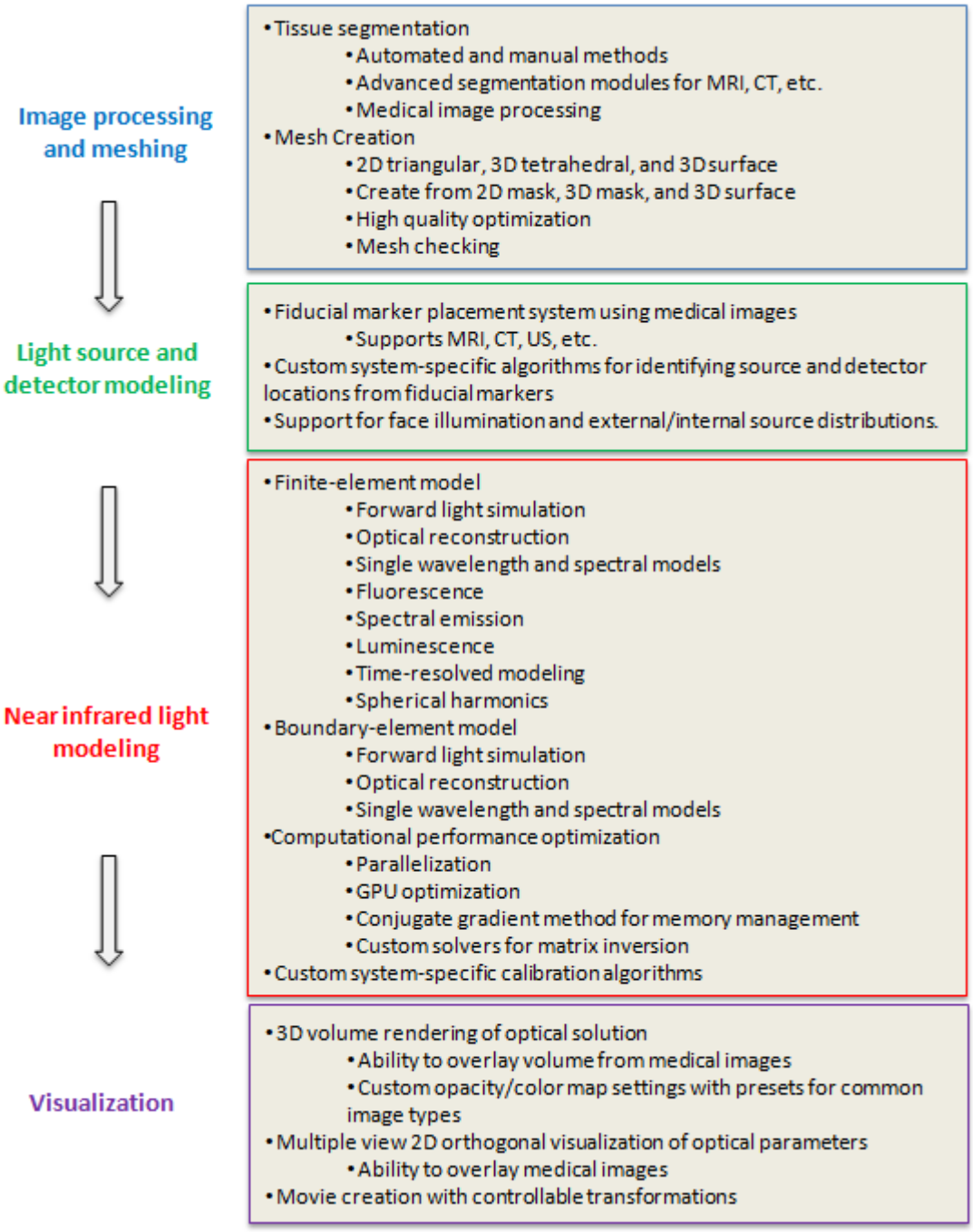

Figure 1. An overview map of the toolboxes and capabilities present in NIRFAST, organized according to the typical workflow used for light modeling.

The segmentation tool allows for easy automated or manual delineation of different tissue types in medical images. Along with any identified fiducial markers, the segmentation can then be used to create a 3D finite element mesh. Once source/detector positions are determined from fiducial positions, the mesh can be used to model light propagation and produce an optical solution of clinically relevant parameters inside the tissue. This optical solution can then be displayed by overlaying the optical parameter map onto the original medical images. These tools are linked with a graphic user interface (GUI) in a seamless manner, allowing for a full user-enabled workflow from the original medical images and data to the resulting optical solution. In 3D, the workflow consists of the following stages:

1. Segmentation: Medical images (typically CT or MR) are used to identify tissue types as different regions in the domain. This process involves the use of automatic segmentation algorithms, manual editing, morphological operations, cropping, hole-filling, region-growing, and more. The region information can be useful for the purposes of simulation as well as when reconstructing with real data. Furthermore, the overall segmentation provides the information needed to create a 3D mesh (see below).

2. Mesh Creation: Based on the segmentation produced in stage 1, a 3D tetrahedral mesh is created consisting of node positions and an element connectivity list. If multiple tissue types were identified in the segmentation process, this mesh will consist of regions by assigning each node a region number. Mesh parameters and

geometric quality assessment of the mesh can have a significant impact on the resulting modeling and optical solution.

3. Source/Detector Placement: Physical indicators known as fiducial markers are often used when imaging to indicate the positions of the light sources and detectors. They are designed to produce contrast in the imaging modality used, so that they are readily visible in the medical images. The proper localization of these is imperative for properly modeling light transport in the domain. The fiducial locations are used to identify the actual source/detector positions. This is entirely dependent on the geometry used and the relative positions of the fiducial markers to the sources and detectors. A generally customizable solution is present to provide users the flexibility to specify these relationships.

4. Simulation/Reconstruction: Finite-element based modeling of the diffusion equation is performed on the mesh, using the source/detector locations, to produce an optical solution at each node in the mesh. Reconstruction recovery of optical interaction parameters or chromophore and scattering parameters is done with an iterative modified Newton method with regularized inversion of the Hessian matrix. Substantial study of this methodology has occurred over the past decade to optimize this approach.

5. Visualization: The computed optical solution is displayed as a 3D volume rendering, with three orthogonal views of movable 2D slices. This solution must

then be overlaid on the original medical images with adjustable threshold values to produce useful visualizations of the result.

NIRFAST provides a workflow that seamlessly combines each of these stages. The following sections describe the developments in each stage of the light modeling workflow.

3.2.1 Segmentation of medical images and finite-element mesh creation

Due to the generally poor spatial resolution of diffuse optical tomography, the prevailing trend in the field is towards combining it with other imaging modalities and incorporating high-resolution tissue structural information in the image recovery algorithm. Notable examples of this include CT or MRI-guided diffuse optical tomography, and these techniques provide the potential for increased accuracy. The time spent segmenting tissue types in these medical images has in the past hindered the usage of image-guided DOT. In this work we have developed tools which allow for increased automation, improving the clinical potential of using image-guidance with optical imaging. Accurate diffusion modeling in optical tomography requires a 3D geometry since the photon scattering is in all directions [51]. The current version of NIRFAST includes full-featured segmentation and mesh creation tools for quickly and easily creating high quality 3D finite-element meshes from medical images [52]. The interface for this is shown in Figures 2 and 3. The segmentation tools have been developed in collaboration with Kitware Inc. (Clifton Park, NY)

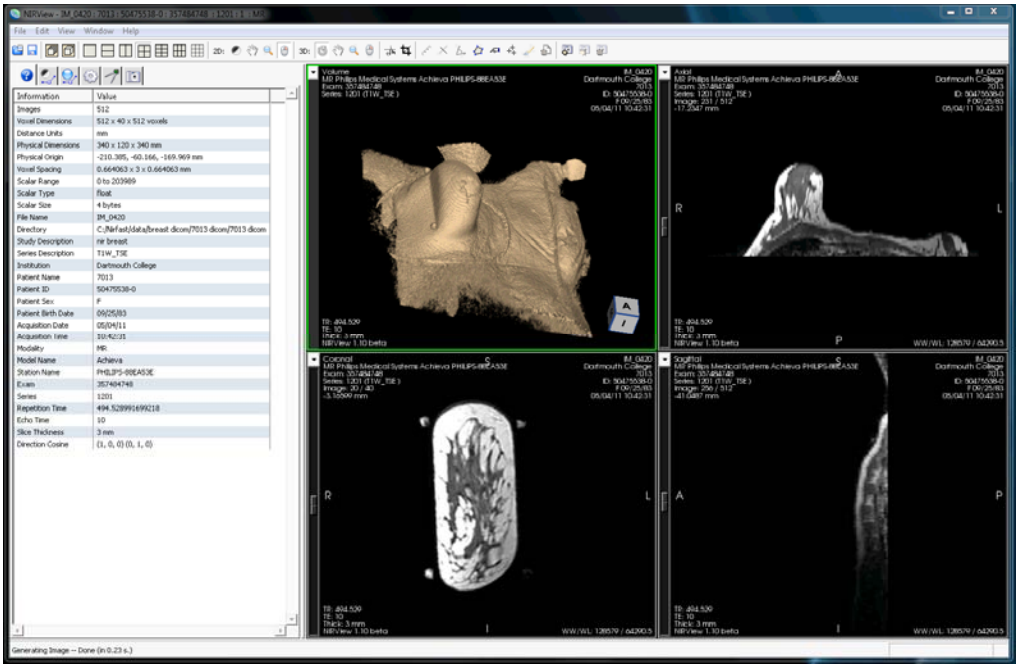

Figure 2. The NIRFAST tool for segmentation of MR/CT DICOMs as produced in collaboration with Kitware Inc. This is the starting point for a higher-end GUI for expert users, allowing high flexibility in segmentation & mesh creation for input.

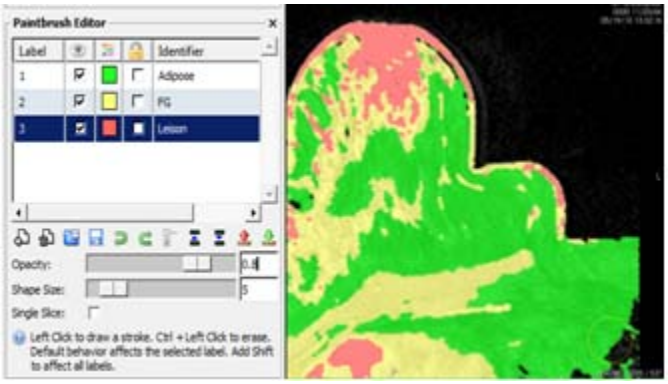

Figure 3. The NIRFAST tool for segmentation medical images, showing a segmentation of fat and glandular tissue in breast tissue containing cancer.

3.2.1.1 Medical image processing

The segmentation and mesh creation tools in NIRFAST allow for a variety of different inputs, including standard DICOM formats for medical images, general image formats (stacks of bmp, jpg, png, etc.), and structured geometry formats (vtk, mha, etc.). It can be used for a variety of different medical imaging modalities, such as CT, MR, Ultrasound, and microCT. The browser for parsing and selecting DICOM sets is shown in Figure 4. The DICOM browser finds all sequences within a folder and displays important sequence information, in addition to a preview of the image sequence. The images can be sliced through, and window/level settings can be adjusted. The flexibility to a variety of different medical image formats is essential for applications in optical modeling, which use a diverse set of images. Both automatic and manual means of segmenting these images have been provided, and mesh creation is fully automated with customizable parameters.

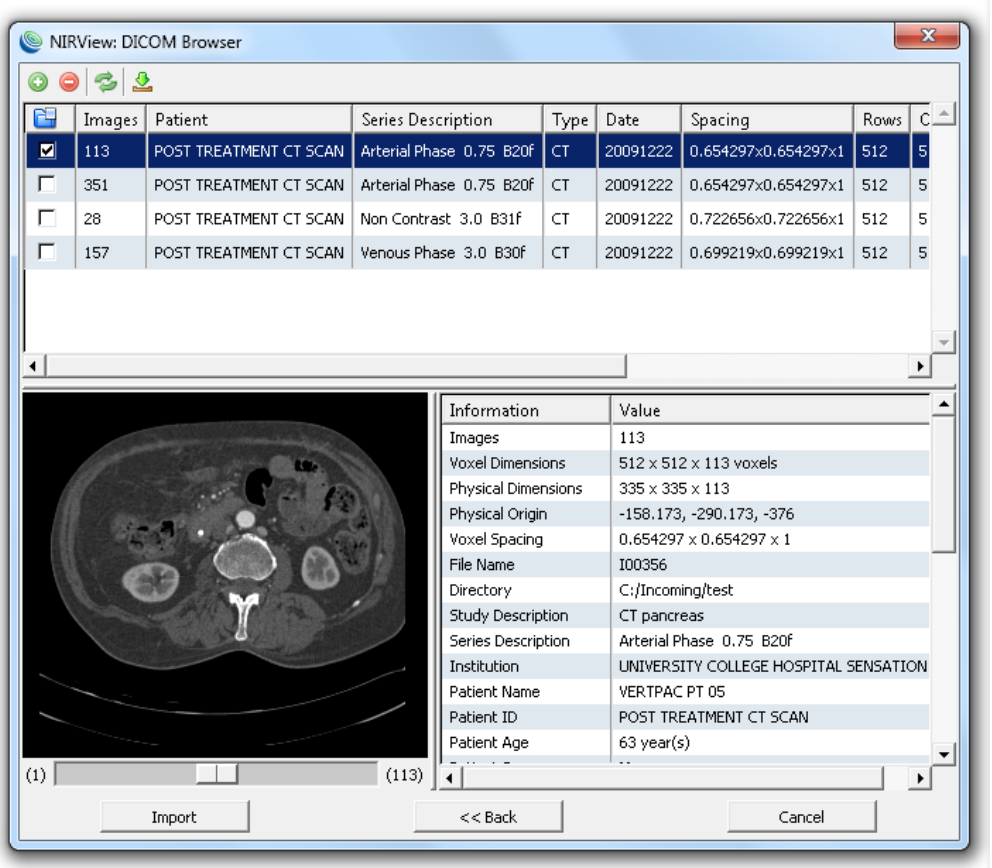

Figure 4. DICOM browser for selecting a set of medical images. The browser will parse an entire folder of medical images into sequences and show relevant sequence information as well as a preview of the images set.

The capability of these tools is demonstrated on 4 different cases that are relevant to modeling of light propagation in tissue and optical tomography: small animal imaging, breast imaging, brain imaging, and light dose modeling in photodynamic therapy of the pancreas. These applications have been chosen to emphasize the applicability of the methods presented in this work to the large variety of applications in near-infrared light modeling. The small animal example used a stack of CT images of the front portion of a

mouse, consisting of 30 axial slices of 256 by 256 pixels, with a slice thickness of 0.35mm. The images were taken on a Phillips MR Achieva medical system, in the form of a DICOM stack. The breast example used a stack of T1-weighted MR images, consisting of 149 coronal slices of 360 by 360 pixels, with a slice thickness of 0.64mm. The images were taken on a Phillips MR Achieva medical system, in the form of a DICOM stack. The brain example used a stack of T1-weighted MR images, consisting of 256 axial slices of 256 by 256 pixels, with a slice thickness of 1mm. The images were taken on a Siemens Trio 3T scanner, and are stored in .hdr and .img files. The pancreas example used a stack of arterial phase CT images, consisting of 90 axial slices of 512 by 512 pixels, with a slice thickness of 1mm. The images were taken on a Seimens Sensation 64 CT system, in the form of a DICOM stack. In each case, the appropriate modules were used to maximize the quality of the resulting mesh, and increase the speed of the entire process.

3.2.1.2 Segmentation of tissue types

The general procedure for processing the images follows: First, the medical images are imported into the segmentation interface. Then window/level settings are adjusted for the 2D orthogonal views of the medical images to improve the desired contrast profile. Color/opacity can also be adjusted of the 3D volume rendering to provide a better global sense of geometry for the user. Next, automatic segmentation modules are used to identify different tissue types and regions as accurately as possible. See Table 1 for the steps used in each case, as well as parameter values. The modules and their respective

parameters are detailed in Table 2. Explanations of the major segmentation modules are described below.

Brain

Step	Time (min)	Parameters
Importing DICOMs	0.15	
K-Means	0.72	6 classes, 0.001 error tol., 1 smoothing factor, 100 iter.
Iterative Hole Filling	0.17	1 radius, 1 majority threshold, 10 maximum iterations
Manual Touch-Up	2.20	fixing larger holes that weren't caught by hole filling
Launching Mesher	0.12	
Mesh Creation	2.28	2.00mm tet/facet size, default values
TOTAL	**5.64**	

Breast

Step	Time (min)	Parameters
Importing DICOMs	0.10	
Cropping	0.01	bounding left breast
Bias Correction	0.10	4 downsample factor, 100x50x50 iter., 200 spline dist.
Skin Extraction	0.22	100 thresh., 1 open. rad., 30 iter., 25 maj. thresh., 1 dil. rad.
K-Means	0.05	3 classes, 0.001 error tol., 1 smoothing factor, 100 iter.
Region Dilation	0.08	1 dilation radius
Iterative Hole Filling	0.01	1 radius, 1 majority threshold, 10 maximum iterations
Manual Touch-Up	16.05	fixing artifacts near chest wall, and stray pixels
Launching Mesher	0.12	
Mesh Creation	0.50	1.29mm tet/facet size, default values
TOTAL	**17.24**	

Small Animal

Step	Time (min)	Parameters
Importing DICOMs	0.15	
Cropping	0.01	bounding the animal
Thresholding	0.03	140 lower threshold, 7023 upper threshold
Iterative Hole Filling	0.01	1 radius, 1 majority threshold, 10 maximum iterations
Manual Touch-Up	14.13	creating interior regions, fixing stray pixels
Launching Mesher	0.16	
Mesh Creation	0.08	0.70mm tet/facet size, default values
TOTAL	**14.57**	

Pancreas

Step	Time (min)	Parameters
Importing DICOMs	0.15	
Cropping	0.01	bounding the pancreas
K-Means	0.13	3 classes, 0.001 error tol., 1 smoothing factor, 100 iter.
Iterative Hole Filling	0.43	1 radius, 1 majority threshold, 10 maximum iterations

Manual Touch-Up	9.88	fixing misclassified blood vessels, stray pixels
Launching Mesher	0.17	
Mesh Creation	1.58	1.40mm tet/facet size, default values
TOTAL	**12.35**	

Table 1. Time benchmarks for the segmentation and mesh creation of 4 different imaging cases: brain, pancreas, breast, and small animal, with the key steps in accurate segmentation identified and the time required for each step specified.

Segmentation Module	User-Controlled Parameters
Iterative hole filling	• Desired hole radius • Majority threshold – number of pixels over 50% required to fill a pixel; this has to do with the curvature of target holes • Number of iterations
K-Means classification and Markov random field	• Number of classes to identify as different regions (tissue types) • Error tolerance for clustering grayscale values into different classes • Degree of smoothness on the classified regions • Number of iterations
MR bias field correction	• Downsample factor – downsamples the image to improve computational time of bias correction • Number of iterations – 3 values controlling the computational time of a 3 part process in bias correction • Spline distance – controls grid resolution, which will affect computational time
MR breast skin extraction	• Threshold below which tissue is considered to be skin/air • Radius of the morphological opening kernel for extracting the largest component of the image (the breast) • Number of iterations • Majority threshold – number of pixels over 50% required to fill a pixel; this has to do with the curvature of the breast • Dilation radius – thickness of the skin
Thresholding	• Lower and upper thresholds – values between which grayscale values are classified as a region
Region Dilation and Erosion	• Dilation or erosion radius – amount by which to dilate or erode the region

Table 2. List of automated segmentation modules available for identifying tissue types, including an explanation of the parameters in each case.

3.2.1.3 Custom segmentation algorithms

Common segmentation algorithms found in software designed for generic image processing frequently do not provide sufficient capabilities for handling the complex contrast profiles encountered in optical modeling applications. For example, methods such as thresholding, clustering, and watershed do not handle boundary delineation well in organs for modalities such as MR, CT, and US. Boundary issues and tissue heterogeneity are a common occurrence in medical images, further confounding the problem. More specific advancements are needed to reduce the need for significant manual segmentation. The clinical viability of light modeling applications depends on advanced segmentation and mesh creation methods for automation in contrast profiles not suitable for standard methods (thresholding, watershed, etc). In the context of segmentation for pancreatic PDT, classifying the necrotic tissue in post-treatment CT scans provides an excellent case for more advanced segmentation algorithms. This is because the boundary between necrotic tissue and normal tissue is extremely diffuse, with high heterogeneity on either side. Generic algorithms such as thresholding or watershed fall short in such an example, whereas using iterative hole-filling combined with k-means and markov random field filtering provides a much more accurate segmentation.

The iterative hole-filling algorithm classifies small volumes within a larger region as part of the outer region. It evolves a contour by applying voting rules until all holes are filled or the maximum number of iterations is reached. In each iteration, a voting

algorithm determines whether each pixel is filled based on the percentage of surrounding pixels that are filled, a ratio defined as the majority threshold [53]. The number of iterations controls the maximum size of holes and cavities filled. This is useful as a final step for any segmentation, to ensure that each tissue type region is homogeneous and lacking unintended holes. It is also synergistic with the connected component thresholding algorithm, which has been developed for the removal of noise in medical images. This method allows any selection of tissue regions in a segmentation to be considered a single volume, and then removes noise exterior to that volume. The filter selects all pixels in a particular set of regions connected to a seed point in the main volume of the segmentation, using a cross-region pixel by pixel expansion. This means that stray or misclassified pixels and small volumes can be handled automatically, without the need for any manual manipulation. There is also a parameter to control whether connected components are preserved or removed, which can allow the noise to be separated and used in Boolean operations. In combination with the iterative hole filling algorithm, noise and holes can be fixed in any exterior or interior tissue type. This is particularly important for medical images with many disjoint parts and/or noise, such as glandular tissue in the breast and brain tissue boundaries. The capabilities of connected component thresholding are demonstrated in Figure X on a segmentation of the brain. There are multiple tissue types, and the filters are able to remove noise and fill holes interior and exterior to each region.

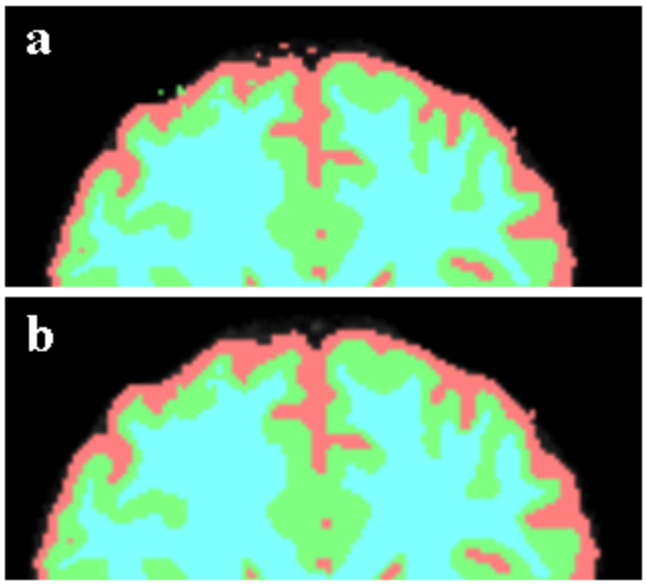

Figure X. (a) Segmented tissue types in the brain, using K-means clustering with Markov random field filtering, overlaid on the original MR slice. (b) The same segmented slice of the brain, with connected component thresholding and iterative hole filling applied to remove noise and fill holes interior and exterior to each tissue region.

There are methods for handling noise based on a single region using basic morphological operations, but the connected component threshold algorithm in conjunction with iterative hole filling is the first existing method with the flexibility to handle noise profiles in any combination of tissue types. It represents a major step towards the automation of segmentation methods for medical images in optical modeling, especially for tissue locations and imaging modalities with complex or multi-part internal tissue geometries.

The K-Means and Markov random field module performs a classification using a K-Means algorithm to cluster grayscale values and then further refines the classification by taking spatial coherence into account [54]. The refinement is done with a Markov Random Field algorithm. The essential minimization function governing this module is

given below, where x is the set of grayscale values, S is the k sets of classification groups, and u is the set of mean values in each S.

$$\arg\min_S \sum_{i=1}^{k} \sum_{x_j \in S_i} \| x_j - u_i \|^2 \quad (9)$$

This method is most relevant to situations where the grayscale values and spatial location of different tissue types show significant differences. It is used as a first step in the segmentation process after any image processing has been applied to the medical images.

The MR bias field correction module removes the low frequency gradient often seen in MR images, based on the non-uniform intensity normalization (N3) approach [55, 56]. This bias is largely caused by the spatial dependence of the receiving coil, and can cause other segmentation methods to be ineffective due to the range of grayscale values produced in each region. The bias field correction is performed by matching a parametric Gaussian model to the bias field in log space. The algorithm iterates between sharpening the intensity histogram of the corrected image and spatially smoothing those results with a BSpline scalar field estimate of the bias. This module is useful for all MRI data, as well as other imaging modalities which may produce low frequency gradients in the images. It is applied before any segmentation modules, to ensure that the gradient does not adversely affect the segmentation process. Figure 5 shows an example of MR bias field correction applied to MR breast images.

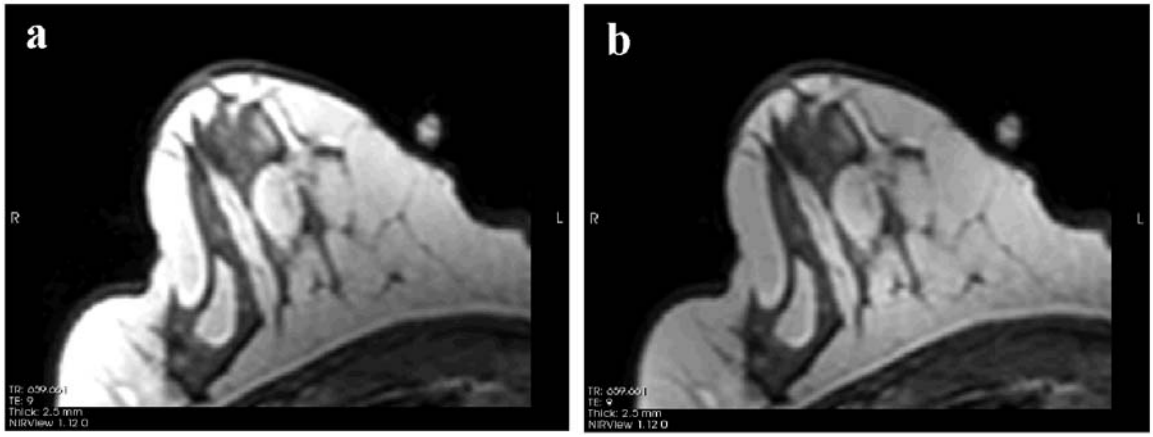

Figure 5. (a) Original MRI axial slice of the breast with a low frequency gradient visible, the bright regions on the left fading into lower values on the right, (b) same axial slice of the breast with MR bias field correction applied to remove the low frequency gradient.

In combination with MR bias field correction, the MR breast skin extraction module helps extract the skin in MR breast images, as it is often lumped in with the glandular region by other automatic modules. Since the grayscale values of the skin are so similar to those of the glandular tissue, the problem is in differentiating the two tissue types. It is also applicable to other imaging modalities and tissue locations where the skin must be segmented out. Previously, this often had to be dealt with by manually segmenting out the skin region using packages like Mimics, a process which can take several hours and is therefore prohibitive to clinical use of optical imaging for these applications. The method presented here directly addresses this problem using a specially designed module which uses several other filters in performing the skin extraction. First a threshold is applied to distinguish the tissue volume (including all tissue types) from the background value of air in the medical images. The threshold value for this can be user-defined, but is by default automatically calculated by analyzing the image intensity range. The pixels in this range are divided into two classes by a threshold which maximizes the inter-class variance.

Then a morphological opening kernel is applied to threshold region. This involves sweeping the opening kernel around the inside of the region, where the opening kernel has been defined as a sphere. This opening process is only performed at the interface between the threshold region and air, and adapts sphere size relative to changes in grayscale value, so as to avoid misclassifying internal tissue types as skin. Figure X illustrates the sweeping process of the morphological opening kernel on an MR breast example.

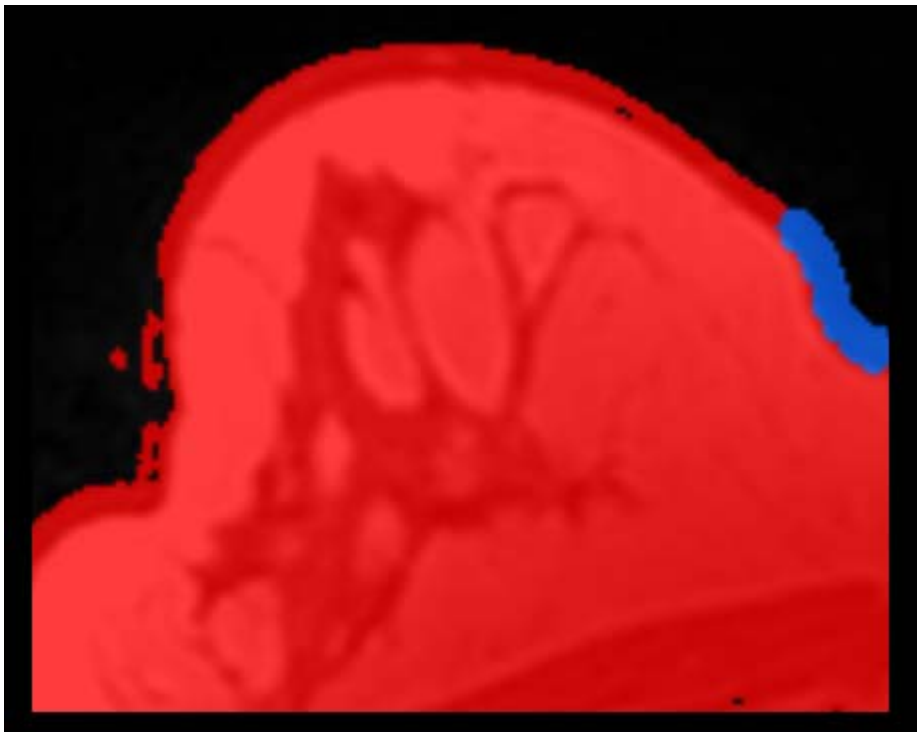

Figure X. An MR slice of the breast, showing a step in the skin extraction process. Red identifies the breast tissue region determined with thresholding. Blue indicates the effect of the spherical morphological opening kernel, as it is in the process of sweeping across the threshold line, as part of the process to determine the skin tissue location.

Noise is then removed from the region defined by the morphological opening kernel, using connected component thresholding. Iterative hole filling is then applied to fix holes within the newly defined skin region. Finally, dilation is used to counteract the innate erosion caused by the morphological opening kernel. The final result of this pipeline is that the skin tissue has been identified as a distinct region, allowing for either inclusion or exclusion in light modeling, based on the modeling needs of the user. This should be used as a first step after medical image processing for MR breast data, or any imaging modality where the skin is visible. Figure 6 shows an example of MR breast skin extraction applied to a segmentation of MR breast images. In this example the skin has been removed from the remaining tissue segmentation, using Boolean operations. This is the only existing segmentation method for skin extraction in the presence of indistinct boundaries and cases of grayscale value overlap; it is essential for automatic segmentation of tissue types in MR breast imaging.

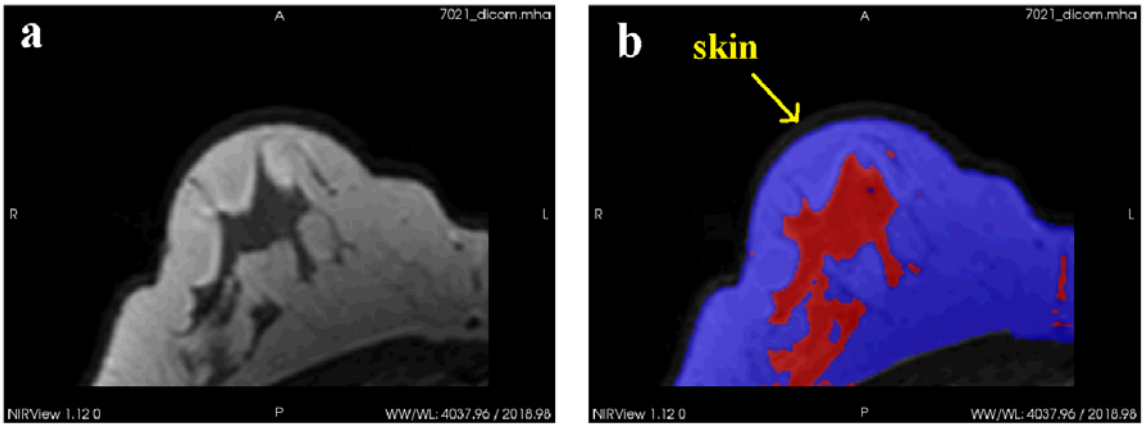

Figure 6. (a) Original MRI axial slice of the breast, (b) same axial slice of the breast with the glandular and other breast tissue segmented in red and blue respectively; MR breast skin extraction has allowed the skin to be separated from other tissue types, and removed from the segmentation.

Thresholding is a fundamental module which identifies a particular range of grayscale values as a single region [57]. It is most useful when tissue types have distinct ranges of grayscale values with negligible overlap, and is used at many stages in segmentation to identify and separate regions. Region dilation and erosion expand or contract a single region by a specified number of pixels in all directions [58]. This can be useful as an alternate method of hole filling, by performing a dilation followed by an erosion of the same magnitude. It can also be used to remove insubstantial components of a volume by performing an erosion followed by a dilation of the same magnitude. An example of this would be removing the ears in a mouse model, due to the extremely small volume. Finally, dilation and erosion can be used to correct region sizing in cases where K-means has produced regions that are too small or large.

3.2.1.4 Tetrahedral mesh creation

After automatic segmentation, the regions are manually touched-up using a paintbrush in order to fix any remaining issues with the segmentation such as stray pixels or holes. Finally, the segmentation is provided as an input to the meshing routine, which creates a 3D tetrahedral mesh from the stack of 2D masks in a single run. This eliminates intermediate steps such as creating 3D surfaces and thus requires less mesh preprocessing. The resulting mesh is multi-region, and can preserve the structural boundaries of segmented tissues. The user has control over element size, quality, and approximation error; see Figure 7 for the interface. For ease of use, these values are set automatically

based on the segmentation and medical image information, and no prior knowledge of mesh generation is required to use the tool.

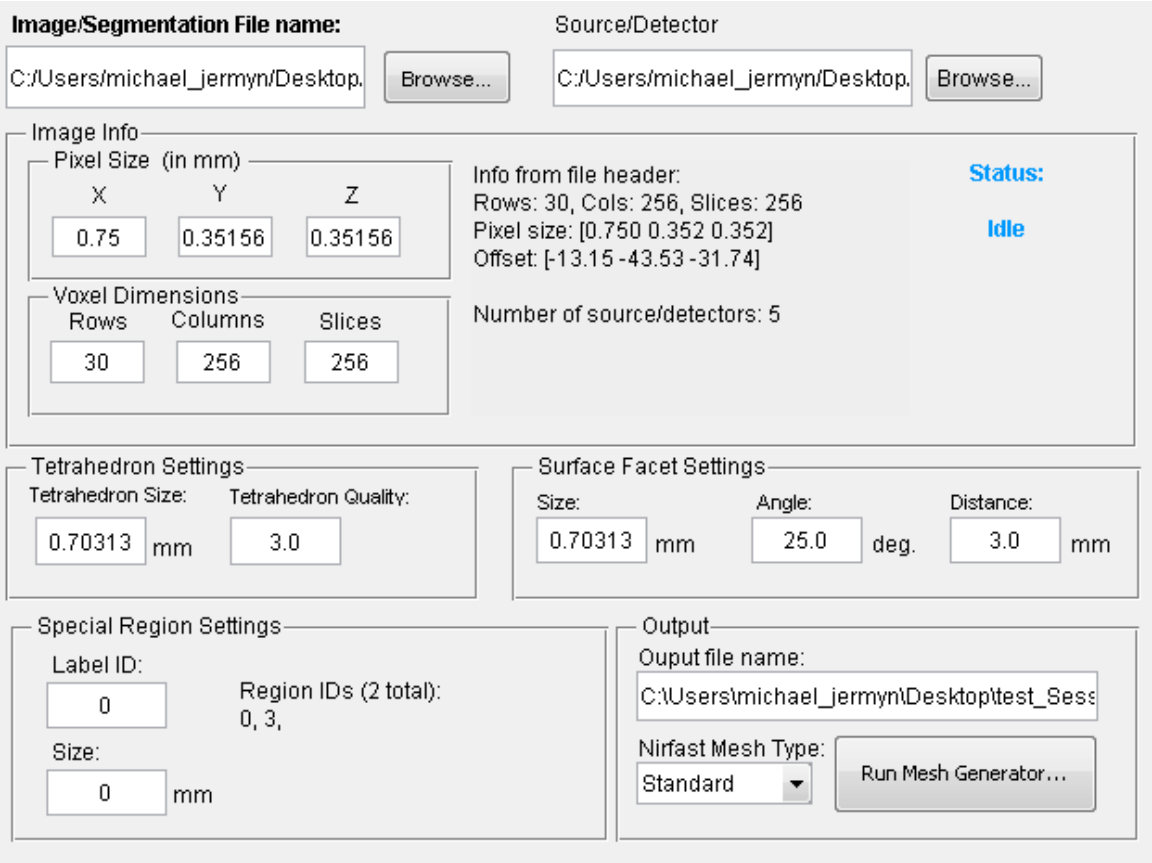

Figure 7. NIRFAST interface for creating a 3D tetrahedral mesh from a stack of segmented images. There are parameters for element size, quality, and approximation error.

The volume meshing algorithm is unique and based on the CGAL libraries [59] and consists of several novel features and implementations that are briefly outlined. The CGAL mesh generation libraries are based on a meshing engine utilizing the method of Delaunay refinement [60]. It uses the method of restricted Delaunay triangulation to approximate 1-dimensional curved features and curved surface patches from a finite set

of point samples on a surface [61, 62] to achieve accurate representation of boundary and subdividing surfaces in the mesh. One very important feature that is of importance is that the domain to be meshed is a region of 3D space which has to be bounded and the region may be connected or composed of multiple components and/or subdivided in several sub domains. The flexibility of this volume meshing algorithm allows the creation of 3D volumes consisting of several non-overlapping regions allowing the utilization of structural prior information in diffuse optical imaging. The output mesh includes sub complexes that approximate each input domain feature as defined in the segmented mask described above. During the meshing phase, several parameters can be defined to allow optimization of 3D meshing, consisting of surface facet settings and tetrahedron size, which are detailed in Table 3.

Meshing Parameter	Description
Angle	This parameter controls the shape of surface facets. It is a lower bound for the angle (in degree) of surface facets. When boundary surfaces are smooth, the termination of the meshing process is guaranteed if the angular bound is at most 30 degrees.
Size	This parameter controls the size of surface facets. Each surface facet has a surface Delaunay ball which is a ball circumscribing the surface facet and centered on the surface patch. The parameter facet_size is either a constant or a spatially variable scalar field, providing an upper bound for the radii of surface Delaunay balls.
Distance	This parameter controls the approximation error of boundary and subdivision surfaces. It is either a constant or a spatially variable scalar field. It provides an upper bound for the distance between the circumcenter of a surface facet and the center of a surface Delaunay ball of this facet.
Tetrahedron quality	This parameter controls the shape of mesh cells. It is an upper bound for the ratio between the circum-radius of a mesh tetrahedron and its shortest edge.
Tetrahedron size	This parameter controls the size of mesh tetrahedra. It is set as a scalar (mm) and provides an upper bound on the circum-radii of the mesh tetrahedra.

Table 3. List of parameters controlling the 3D tetrahedral mesh creation, including description of the function of each parameter.

Once the volumetric mesh has been created, a novel feature has been added to allow the users to further optimize the 3D mesh utilizing the Stellar mesh improvement algorithm. [63]. This optimization routine improves tetrahedral meshes so that their worst tetrahedra have high quality, making them more suitable for finite element analysis. Stellar employs a broad selection of improvement operations, including vertex smoothing by nonsmooth optimization, stellar flips and other topological transformations, vertex insertion, and edge contraction. If the domain shape has no small angles, Stellar routinely improves meshes so that the smallest dihedral angle is larger than 30 degrees and the largest dihedral angle is smaller than 140 degrees. These optimization schemes are essential for accurate optical modeling, and are particularly important for an application like photodynamic therapy in the pancreas, where ensuring accuracy at small distances from the fiber location is extremely important for effective dosimetry.

3.2.1.5 Metric comparisons of speed, quality, and reconstruction

The time of each step in segmentation and meshing was recorded for all cases, and the results are shown in Table 1. A visualization of a mesh for the brain and breast is shown in Figures 8 and 9 for illustration. Using the case of the pancreas, the time taken for segmenting and creating a mesh using the tools in NIRFAST was compared with that of the commercial package Mimics, designed for medical image processing [64]. As seen in

Figure 10, NIRFAST shows drastic improvements in the speed of both segmentation and meshing.

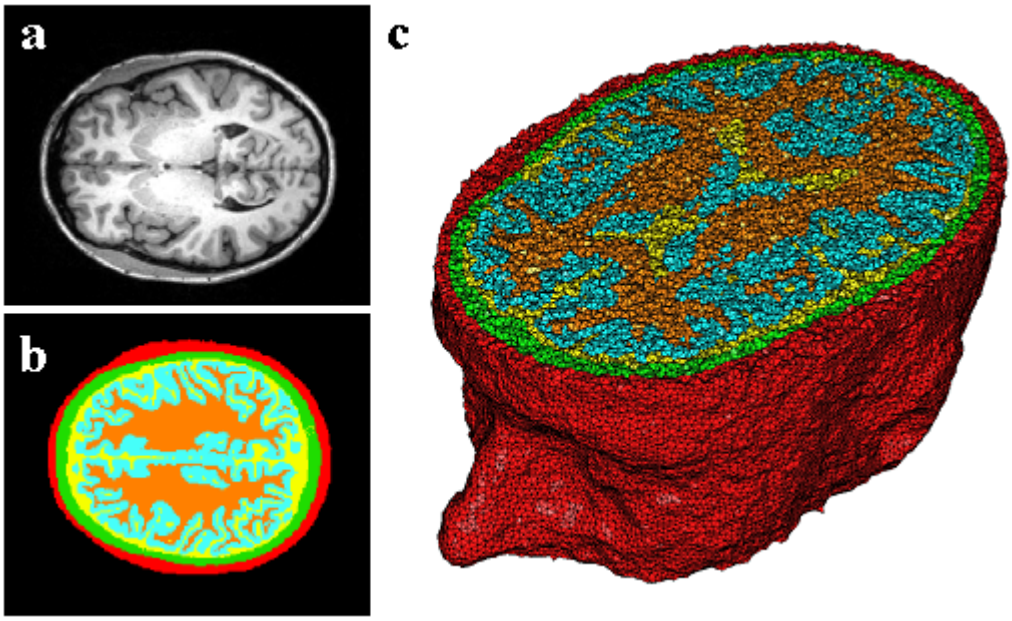

Figure 8. (a) Original MRI axial slice of the brain, (b) segmentation of different tissue types, and (c) the 3D tetrahedral mesh for the brain, showing the regions as different colors: red is the skin, yellow is the cerebral spinal fluid, green is the skull, blue is the white matter, and orange is the gray matter.

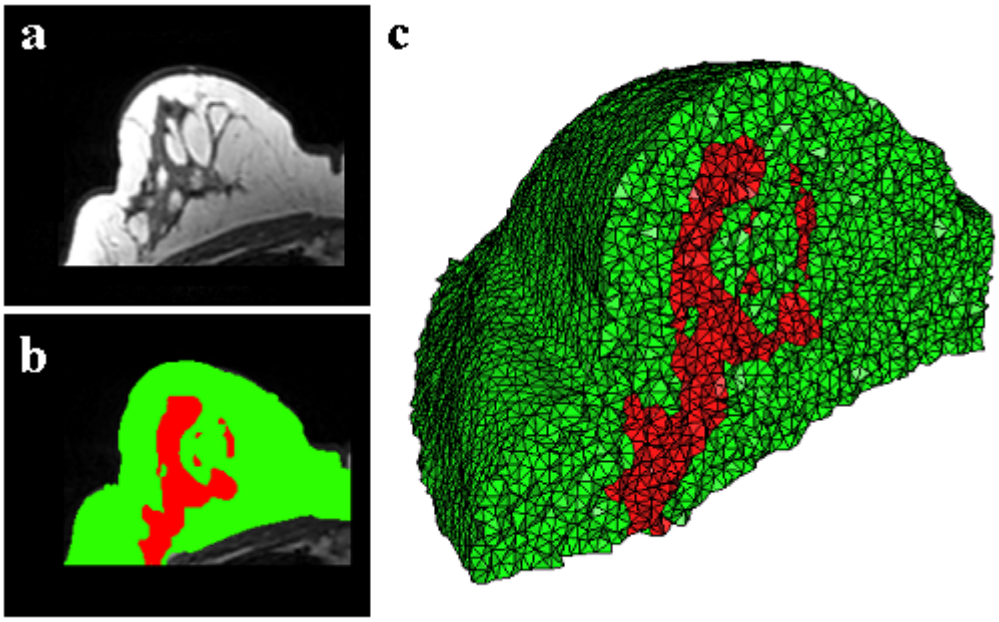

Figure 9. (a) Original MRI slice of the breast, (b) segmentation of different tissue types, and (c) the 3D tetrahedral mesh for the breast, showing the regions as different colors: red is the glandular tissue, and green is other breast tissue.

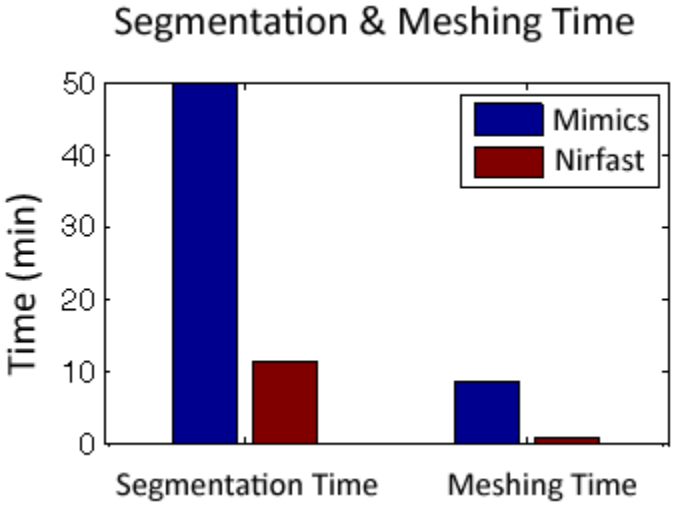

Figure 10. Time comparison of segmentation and mesh creation from Pancreas CT between NIRFAST and the commercial package Mimics.

The resulting 3D tetrahedral meshes from both programs were then analyzed to assess element quality. Also analyzed was a new mesh optimization feature in NIRFAST. This is an optional procedure that searches the mesh for poor quality elements and attempts to fix them to improve quality, as defined below. It can take a significant amount of time for large mesh sizes, but can vastly increase the quality. In this case, optimization took 15 minutes. The meshes were made to have a similar number of nodes: 224,049 for the Mimics mesh, 224,445 for the NIRFAST mesh, and 224,989 for the optimized NIRFAST mesh. The metric used for quality criterion is the sine of minimum dihedral angle of each tetrahedron. Values close to zero would indicate an almost flat element. Such elements can cause loss of numerical accuracy as well as making the stiffness matrix in the FEM formulation ill-conditioned. The optimal value of this quality would be $\sin(70.52^\circ) = 0.942$ for an equilateral tetrahedron; however the upper bound is 1.0. Figure 11 shows the quality histograms using Mimics, NIRFAST, and mesh optimization in NIRFAST. The minimum quality for each case respectively was 0.06, 0.12, and 0.65, with average quality values of 0.71, 0.73, and 0.77.

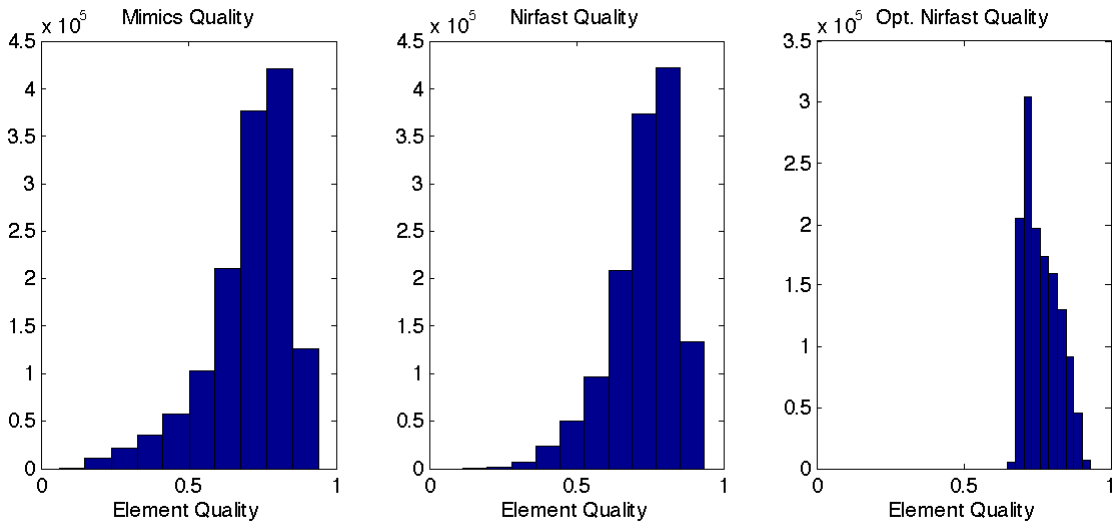

Figure 11. Histograms comparing mesh element quality between the commercial package Mimics and the tools developed in NIRFAST. Also shown is the quality histogram when using the mesh optimization feature in NIRFAST.

Reconstructions were performed for the small animal case with meshes created from segmentations in Mimics and NIRFAST, using the optimization tools in each respectively. The nude mouse was implanted with tumor cells in the animal's brain, injected with Licor IRDye-800CW EGF, and imaged at Dartmouth College with an MRI-FMT system using a protocol described in a previous publication [65]. Fluorescence optical data from 8 source and detector locations positioned evenly around the mouse head was calibrated in NIRFAST, and used in reconstruction. Figure 12 shows the reconstruction results in the mouse head using the Mimics mesh and the NIRFAST mesh, displaying fluorescence yield overlaid on the MR images. The recovered fluorescence yield for each region in both cases is reported in Table 4.

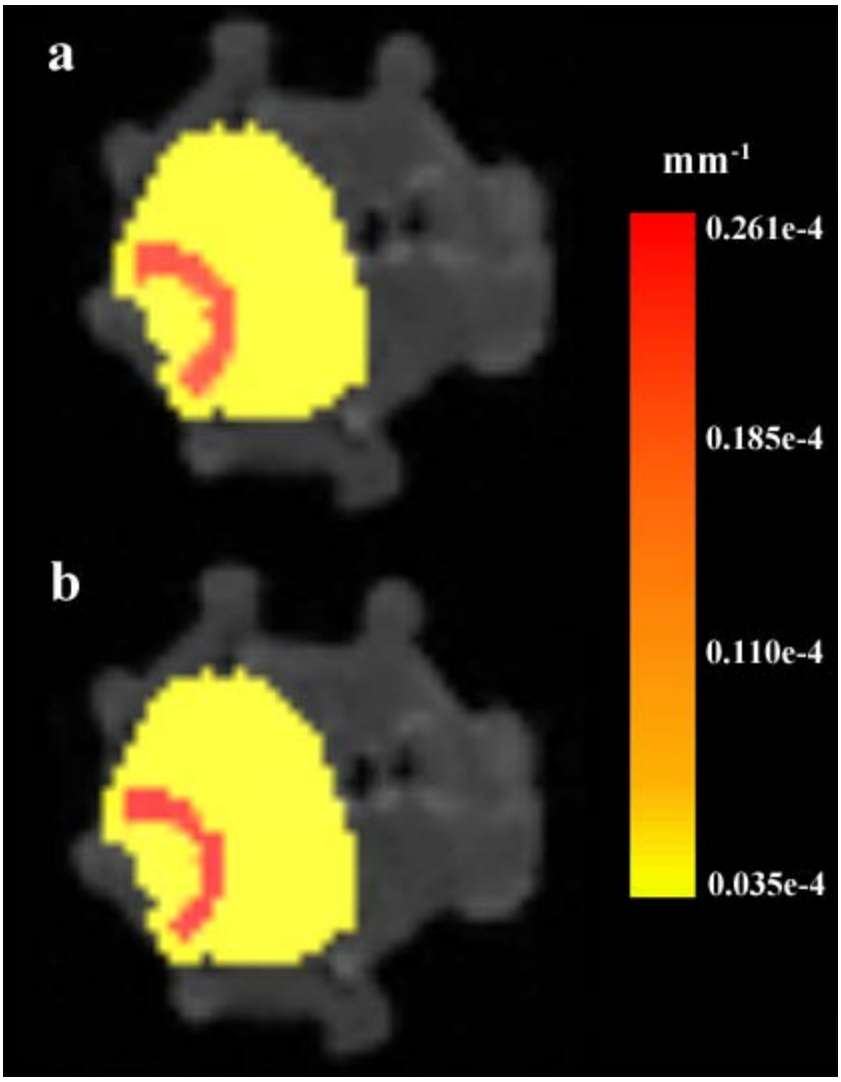

Figure 12. Reconstructed fluorescence yield overlaid on sagittal MR images of the mouse head, based on reconstructions on a mesh created in Mimics (a), and in NIRFAST (b). The fluorescence tomographic reconstructions are based on the segmentation of tissue types and region based reconstruction on the resulting tetrahedral meshes.

Tissue Region	Recovered Fluorescence Yield in Mimics Mesh (mm^{-1})	Recovered Fluorescence Yield in NIRFAST Mesh (mm^{-1})
Background Tissue	0.0352e-4	0.0350e-4
Brain	0.0802e-4	0.0793e-4
Tumor Boundary	0.2601e-4	0.2609e-4

Tumor	0.0865e-4	0.0870e-4

Table 4. Recovered fluorescence yield for each region in reconstruction using the mouse head. Results are reported on both the Mimics and NIRFAST created meshes.

New segmentation and mesh creation tools have been implemented in NIRFAST, with the ability to work from the variety of medical images encountered in optical tomography. The efficacy of these tools has been compared with the commercial package Mimics in a case study. The minimum and average tetrahedron element quality values are better using NIRFAST (especially when using mesh optimization). In particular the minimum quality is 62% higher relative to the optimal value using NIRFAST. Low quality elements can produce erroneous numerical solutions by several orders of magnitude, or even prevent a solution from being computed, so this improvement in the minimum quality threshold is essential for diffuse optical tomography. There is a large difference in the amount of time spent, with NIRFAST being far more efficient by ~5 fold. In segmentation, this is partly affected by the efficiency of the automatic segmentation methods, but also by the availability of many advanced segmentation tools that are particularly useful for the typical contrast profiles seen in MR/CT. A good example is breast imaging using MR guidance, where low frequency gradients are often seen in the images. In the past this has often hindered the ability to segment these images, as grayscale values of the same tissue type will no longer be in the same range [66]. These gradients can be easily removed using MR bias removal, thus greatly reducing the amount of manual touch-up needed after automatic segmentation. In meshing the improved computational time is in part due to the fact that the new meshing tools are

completely automatic, and do not require any fixing after mesh creation. The metrics used for speed and quality in comparison with Mimics account for all pre- and post-processing done using tools available in Mimics to improve mesh quality, but not any external tools that may be used separate from Mimics. For example, 3-matic is a tool also marketed by Materialise, capable of post-processing mesh quality improvement, which could significantly improve the quality of meshes produced by Mimics.

An advantage of the NIRFAST package that is not evident from the time benchmarks is the ease of use in the workflow. Since the entire package has been designed around seamlessly segmenting, creating a mesh, modeling light transport, and then visualizing the result, it is much easier to use than a combination of packages which are not optimized for optical tomography. In reconstruction results, as seen in Table 4, the recovered fluorescence yield is very similar between Mimics and NIRFAST. In fact there is a small improvement in the tumor and tumor boundary to background tissue fluorescence yield contrast recovered. This indicates that the new tools do not adversely affect reconstruction, despite saving significant time during segmentation and mesh creation. Furthermore, the higher minimum element qualities ensure that numerical issues do not arise with generating forward data on a poor quality mesh, which can often cause a reconstruction to fail entirely and terminate before converging upon a solution. One of the advantages of the meshing tools presented is the fact that interior region surfaces are maintained in the mesh, as opposed to simply labeling interior elements based on region proximity. This is very important in FEM modeling for optical tomography, as having the boundary of a surface inaccurately represented can lead to poor quantification [67].

3.2.2 Source and detector placement from fiducial markers

NIRFAST allows for custom system specifications for identifying light source and detector locations, either a priori based on the tetrahedral mesh geometry, or as determined from fiducial markers identified in medical images. The process for this involves first identifying fiber locations in the original medical images using the built-in fiducial specification system, as demonstrated in Figure 13.

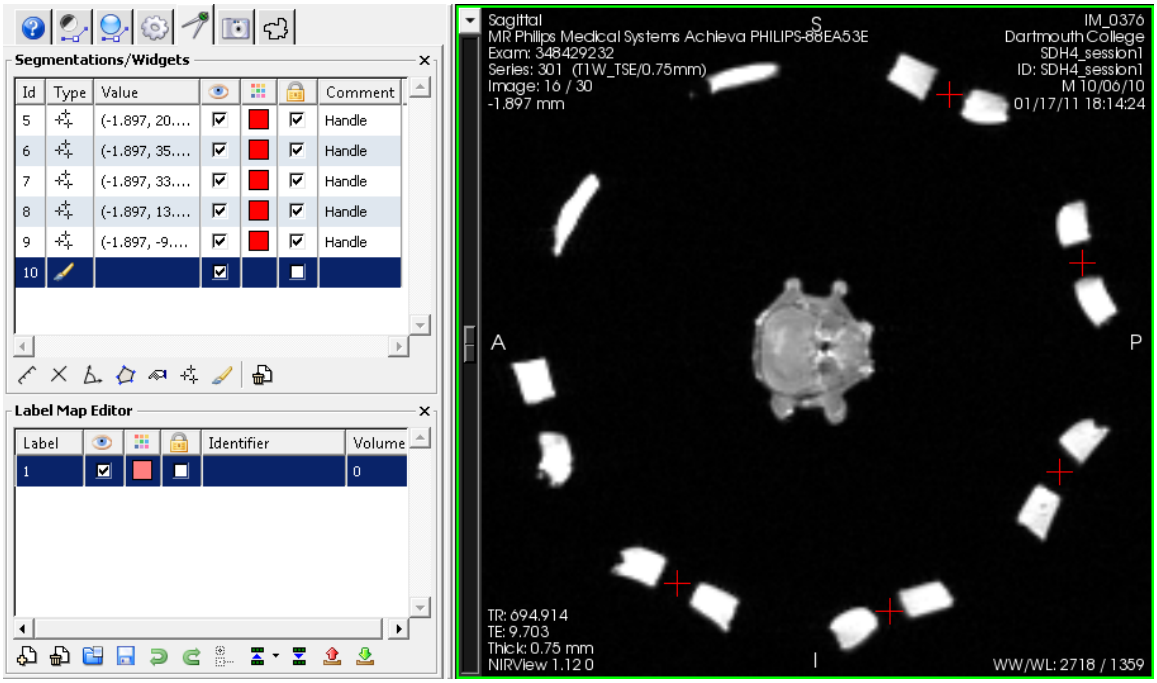

Figure 83. Fiducial marker identification system in NIRFAST, demonstrated on a small animal MR example. Red plus signs indicate fiducial locations of fibers identified in the sagittal orientation of the MR images.

The fiducial marker locations are then transferred through the mesh creation tools into the source/detector placement interface, shown in Figure 14. This allows for custom system setups in determining source and detector locations relative to the tetrahedral mesh, using the fiducial marker locations. Some of the source/detector geometries supported by default include circular, parallel plate, triangular, and light-emitting fibers. NIRFAST has the ability to support distributed illumination sources. The interface also has the capability for manual placement by clicking on the surface of the mesh.

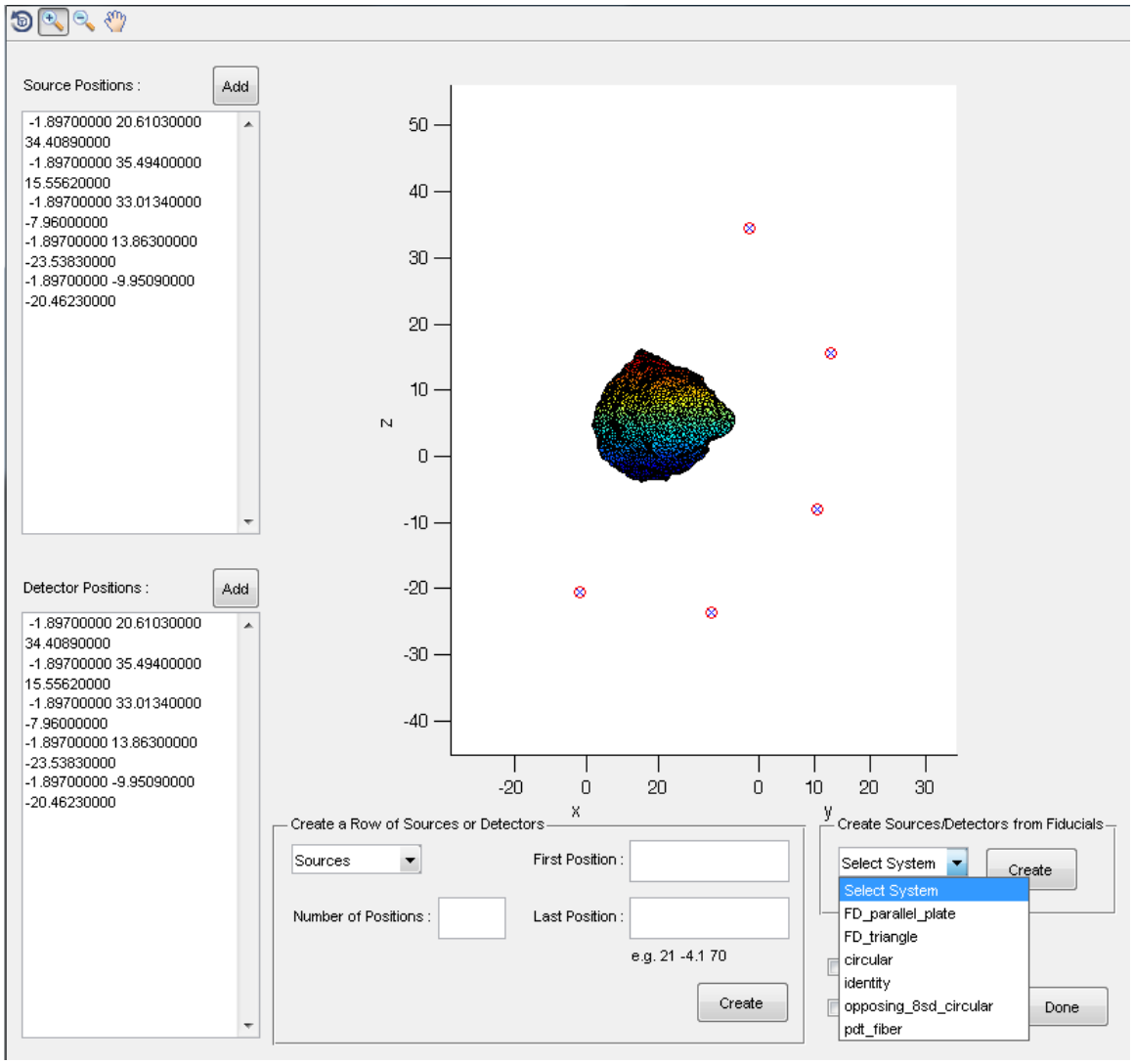

Figure 94. Source/detector placement interface in NIRFAST. This allows for source and detector positions to be determined from fiducial marker locations, based on the system geometry used.

3.2.3 Forward/ inverse light modeling developments

Strides have been made to improve the performance and capabilities of simulation and reconstruction in NIRFAST. Parallelization and GPU acceleration are being utilized to reduce reconstruction times to more realistic values for a clinical setting, in particular for computationally expensive calculation of the sensitivity matrix (Jacobian). A conjugate gradient based method has been developed to be able to handle data sets where memory limits would traditionally be a constraint on the size of the problem. Improvements have also being made to the structure of the code and data/mesh formats, in an effort to increase usability and make it easier to contribute changes/improvements to NIRFAST. A user interface has also been developed to improve ease-of-use and scalability to different user levels. This menu-driven system provides an easy workflow for novice users, while retaining the flexibility needed for expert users. Several elements of the interface have been improved to allow maximal customizability by creating an adaptable and scriptable user interface. A good example of this is the ability to easily add your own Matrix inversion solver to NIRFAST, and it will be automatically detected and included in the user interface, as illustrated in Figure 15.

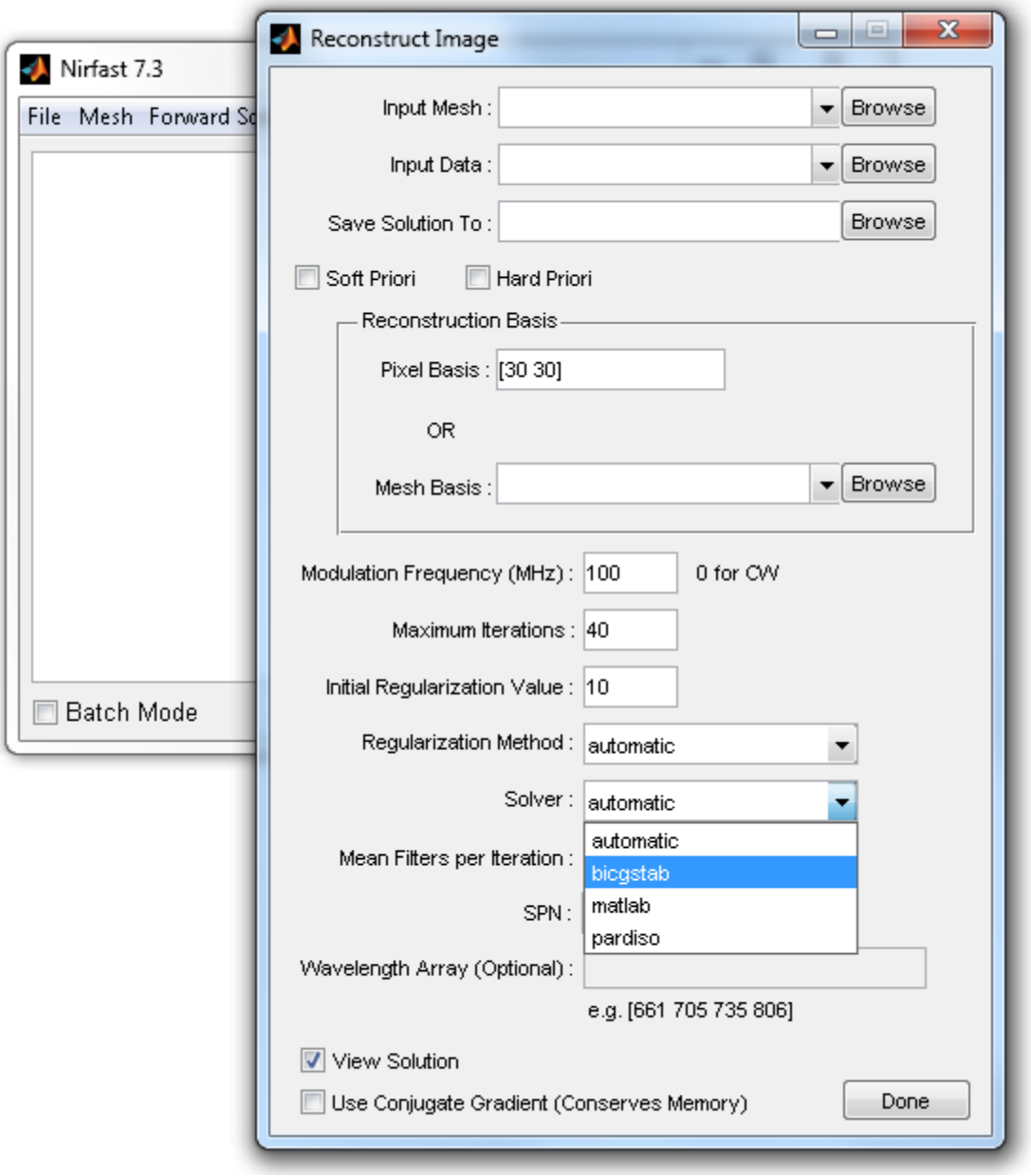

Figure 105. The reconstruction graphical interface for NIRFAST. The list of solvers for use in reconstruction is automatically populated with any custom scripts created by the user, as well as certain default options.

The robustness of NIRFAST has been increased by automatically checking for assumptions such as mesh tetrahedron quality, appropriate values for optical properties, unused mesh nodes, source/detector positioning, and more.

The boundary-element method (BEM) has been made available in NIRFAST as an alternative to FEM. The BEM toolbox has been fully integrated into NIRFAST, which uses 3D surfaces rather than volumes. The assumption is that each region is homogeneous. Under this assumption, computational gains can be made in speed and memory use [68]. BEM has been implemented for both single wavelength and spectral cases, and the toolbox makes use of parallel capabilities for further speed improvements using the open-MP and MPI standards. Modeling can also be performed using the spherical harmonics approximation, rather than the diffusion equation. The SPN toolbox allows for the forward solver and reconstruction functions to use the spherical harmonics approximation at n=1,3,5, or 7. This can allow for a more accurate model than the diffusion equation (n = 1) when the anisotropy factor (g) of the domain is known. It is particularly useful for small geometries and situations where the distances between sources and detectors are small [24]. Time-resolved code has been added to NIRFAST, allowing for the simulation of time-dependent data.

3.2.4 Visualization of optical solutions with medical images

Optical solutions from NIRFAST, either in the form of optical fluence/dose or optical properties such as oxygen saturation and water content, are data defined at each node in a tetrahedral mesh. This data can be visualized in 3D either on its own or

registered with a volume rendering of the original medical images used. An MR breast example of this visualization is shown in Figure 16, displaying the total hemoglobin reconstructed in the breast.

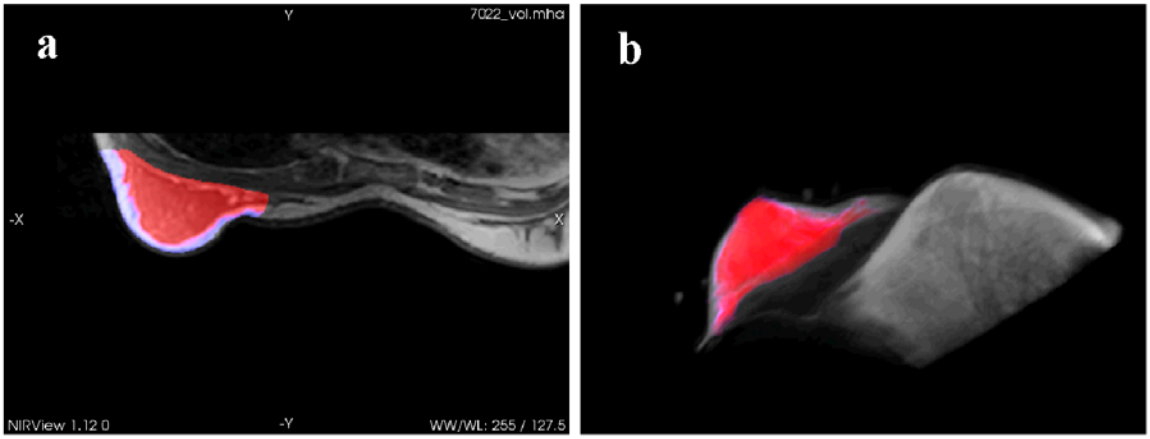

Figure 116. Visualization of the reconstructed values for total hemoglobin in the breast, rendered as an overlay of the original MR images of the breast with custom color/opacity settings. (a) Shows the optical solution overlay in 2D on a single MR slice; (b) Shows the optical solution overlay in 3D on the MR volume.

There are several presets available for adjusting the color and opacity maps of both the optical solution as well as the volume rendering of the medical images. Custom maps can also be created, and multiple parameters can be visualized together on the same medical image volume if desired. Figure 17 shows the interface for defining color and opacity maps. NIRFAST is capable of visualizing parameters as a volume rendering or a maximum intensity projection. These visualizations can also be used to create snapshots or animations, either in 2D or 3D. Formats supported in 3D are AVI and MPEG2, and in 2D are PNG, TIFF, and JPEG. The interface for this is shown

in Figure 18. The user can control automated animation triggers for transformation parameters such as rotation and zoom.

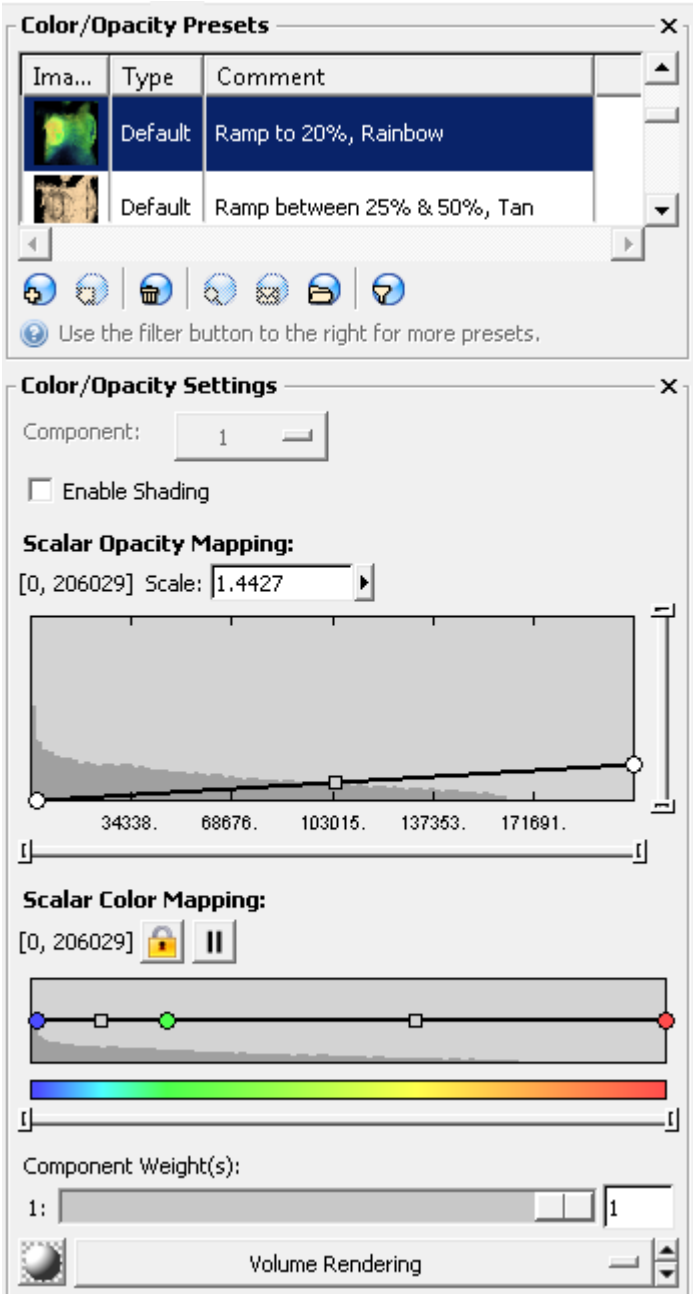

Figure 127. Interface for defining the color and opacity maps for the 3D visualization of optical solutions and medical image volume renderings. Multiple optical parameters can be visualized, each with its own color/opacity maps.

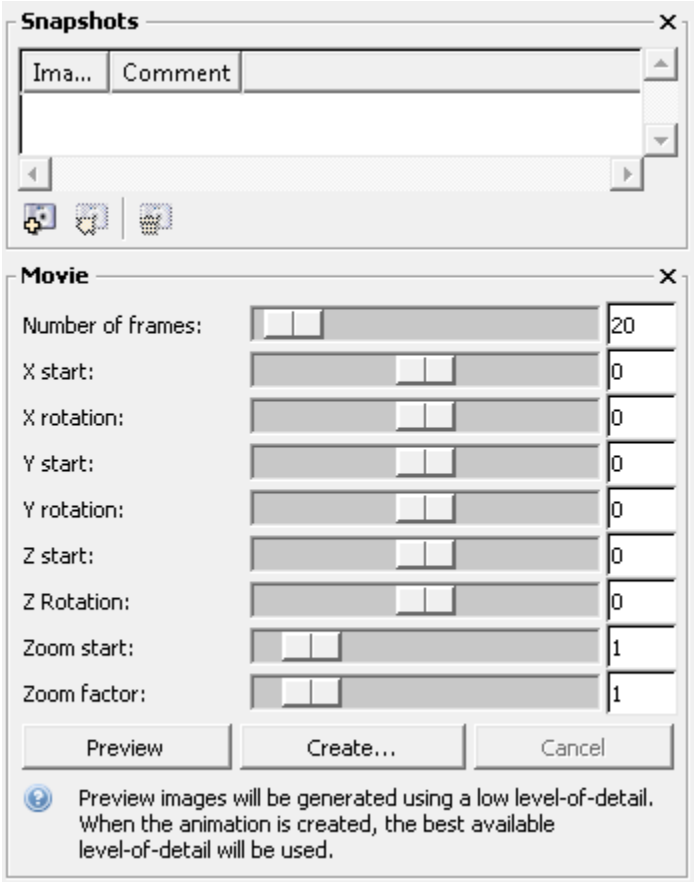

Figure 138. Interface for creating snapshots or movies of 2D or 3D visualizations of optical solutions. Animations can be triggered with automated rotations and other transformation factors.

3.3 Significance and innovation for clinical application

In 2009 optical modeling tools were limited in their capabilities to core light modeling of the forward and inverse problem, with very limited or no features for advanced visualization, image processing, and mesh creation. Presented in this work are tools which have allowed for advanced medical image segmentation, high quality 3D FEM mesh creation, system-specific light modeling, and fast visualization of optical solutions. These tools crucially include automated methods for handling processes which previously

required significant time and manual manipulation, designed to innovate how image-guided DOT is approached with a goal of clinical application. The ease and speed of segmentation and meshing is very useful in promoting the use of optical tomography, which has long suffered from long, difficult, and non-robust meshing procedures. Furthermore, the available automatic segmentation modules provide essential tools for many different types of medical images, particularly in regard to artifacts often seen in MR images. The tools are provided as part of a complete package designed for modeling diffuse light transport in tissue, allowing for a seamless workflow that has never before been available. NIRFAST has become a tool of great value in the optical imaging community, with over 80 unique downloads monthly and is used at many different institutions internationally: Washington University, University of Birmingham, University of Pennsylvania, Harvard University, University of Toronto, University of California: Irvine, and many more. It is an open source project that encourages and has benefitted from collaborations with other institutions. The new tools and methods described in this work have advanced the use of near-infrared imaging in fluorescence tomography of small animals, brain activation imaging, MR-guided breast spectroscopy, molecular luminescence imaging, and more. This is exemplified by the developments in MR bias field correction and skin extraction, which have significantly reduced the amount of time required for image-guided breast spectroscopy by automating much of the tissue segmentation process, making clinical translation much more feasible. The work presented uses innovations in image processing, meshing, and modeling to advance the use of near-infrared imaging clinically.

The optical tools described in this section have been developed with an aim towards improving the workflow for clinical applications of optical modeling, and in particular to assist in providing dosimetry information for photodynamic therapy in the pancreas. This is an application which requires accurate geometry representation as well as accurate optical modeling, due to the region of interest in close proximity to the light-emitting fiber. Furthermore, nearby blood vessels or areas of high blood content can cause very high attenuation, and there can be high intra- or inter-patient optical heterogeneity, all of which can significantly alter the expected response to treatment in a patient.

4. Clinical application: dosimetry for pancreatic photodynamic therapy

The goal of this work was to determine dominant factors affecting treatment response in pancreatic cancer photodynamic therapy (PDT), based on clinically available information in the VERTPAC-01 trial. Both contrast-derived venous blood content and necrotic volume from light modeling yielded strong correlations with observed necrotic volume (R^2=0.85 and 0.91, respectively). These correlations were much stronger than those obtained by correlating energy delivered vs. necrotic volume in the VERTPAC-01 study and in retrospective analysis from a prior clinical study. This demonstrates that contrast CT can provide key surrogate dosimetry information to assess treatment response. It also implies that light attenuation is likely the dominant factor in the VERTPAC treatment response, as opposed to other factors such as drug distribution. This study is the first to show that contrast CT provides needed surrogate dosimetry information to predict treatment response in a manner which uses standard-of-care clinical images, rather than invasive dosimetry methods.

4.1 VERTPAC-01 Trial

The VERTPAC-01 trial investigated the safety and efficacy of PDT in 15 patients with locally advanced pancreatic adenocarcinoma [24]. Patient eligibility was dependent on a confirmed histopathological/cytological diagnosis, sufficient biliary drainage, negative pregnancy, and an ECOG performance status of 0-2. Criteria for exclusion included porphyria, locally advanced disease involving more than half the circumference of the duodenum or a major artery, and metastatic disease. In total 15 patients were treated, 11 male and 4 female, out of 58 patients screened. Some of the patients had been treated

with chemotherapy, chemoradiotherapy, or immunotherapy prior to the VERTPAC-01 trial. The age range of the patients was 47 to 78. Verteporfin was used as the photosensitizer, with Benzoporphyrin Derivative as the photoactive constituent, at 0.4mg/kg bodyweight. Prophylactic intravenous ciprofloxacin was also delivered at 400mg. Patients were sedated using midazolam and fentanyl. Local anaesthesia was used inside the anterior abdominal wall. Light at 690nm was delivered via a light-emitting diffusing-cylindrical tip fiber through transcutaneous, translucent 19-gauge hollow metal needles into the tumor lesions, under CT guidance with a radiologist. The source was an OpadL, 0.3W diode laser. For 13 of the patients, a single 1cm fiber was used. For one patient, 3 fibers were used of length 2cm each. For one patient, 2 fibers were used of length 1cm each. The energy delivered per cm of fiber length was increased in a dose escalation protocol from 5J/cm for 3 patients, 10J/cm for 3 patients, 20J/cm for 3 patients, and 40J/cm for the remaining 6 patients. For 24-48 hours after treatment patients were kept in subdued lighting, followed by gradual reintroduction of normal light levels [24].

Figure 19 outlines the imaging, treatment, and follow-up process for the study. High resolution contrast and non-contrast CT scans were acquired approximately 60-90 minutes prior to treatment for each patient. The contrast scans were obtained for both arterial and venous phases. In addition to these scans, several low resolution CT scans were acquired about the plane of the tumor location to aid in needle/fiber placement. The limited volume captured by these low resolution scans was chosen to limit radiation dose to the patients. Verteporfin is cleared rapidly, leading to a short period of photosensitivity [24], and thus patients were treated approximately 60-90 minutes after administration.

Post-treatment high resolution contrast CT scans to identify response were taken 3-5 days after treatment, in arterial and venous phase.

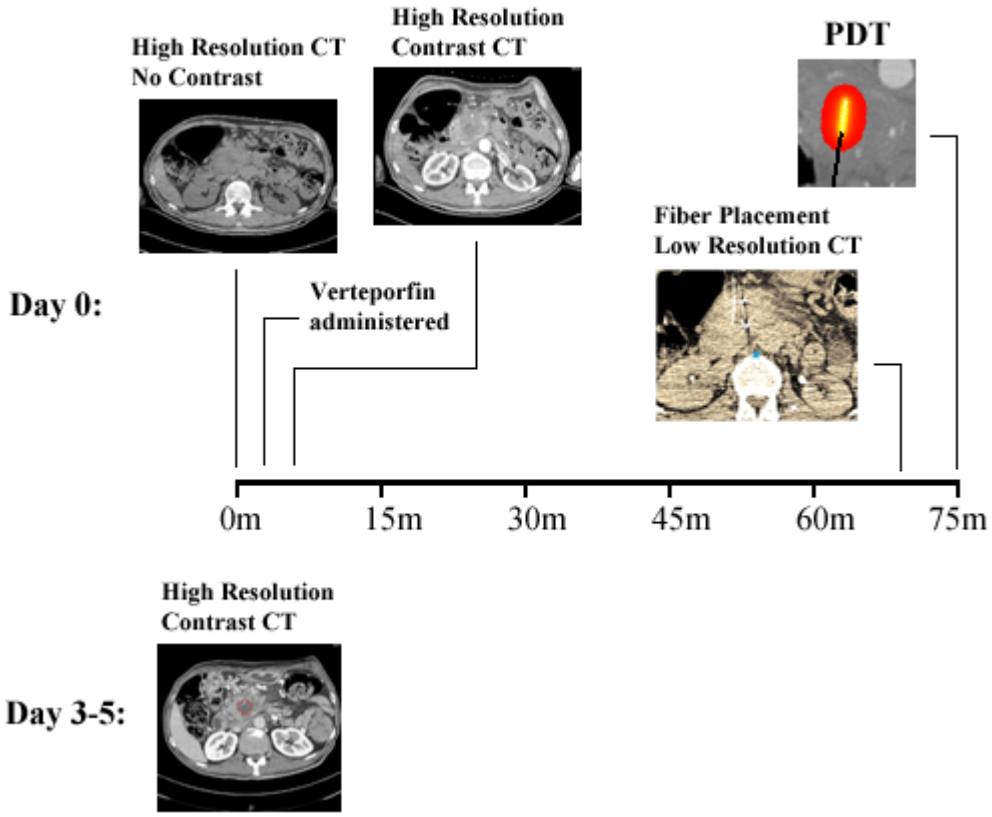

Figure 149. Patient imaging and treatment workflow. The initial two scans are high resolution, pre- and post-contrast. The lower resolution scan shows the fiducial markers on the fiber, evident in the CT scan as two bright spots with star artifacts from x-ray beam hardening. The post-treatment contrast CT scan shows necrotic tissue as a dark area, circled in red on the scan. The scans are all of axial orientation.

The post-treatment CT scans were used to estimate the major diameters of the zone of necrosis. Two stopping criteria were used in the VERTPAC-01 trial: a mean diameter of at least 12mm for the necrotic region, or an unacceptable level of toxicity. 28 days after treatment, an interval CT was performed for each patient. After this point patients were able to initiate oncological treatment if desired. Further CT scans were

taken every three months to assess treatment response, and patients were followed for survival data. There were no early complications for the single-fiber patients, including photosensitivity, bleeding, or biliary/duodenal obstruction. The two multiple-fiber patients showed inflammation anterior to the pancreas by the needle tract, in both cases showing no resulting change in their clinical state. The inflammation was not related with intra-abdominal collections or sepsis, and in both cases resolved by day 28. All late complications occurring at least 28 days after treatment were associated with tumor progression: obstructive jaundice in 2 patients, gastric outlet obstruction in 2 patients, fever in 1 patient, and Whipple's resection in 1 patient. The median survival among single-fiber patients was 11.4 months, ranging from 5.6 to 25.9 (alive) months. The two multiple-fiber patients survived for 4.1 and 5.6 months [24].

4.2 Biological parameters and modeling

The pre-treatment contrast CT scans were used to estimate values for arterial and venous blood content in the pancreas tissue as well as the blood vessels. Venous blood content was calculated as

$$\mathbf{v}_{\mathbf{tissue,\ ven}}/\mathbf{v}_{\mathbf{blood,\ ven}} \tag{10}$$

where $\mathbf{v}_{\mathbf{tissue,\ ven}}$ is the difference between the mean grayscale value in the region of interest in the venous contrast scan and the non-contrast scan, and $\mathbf{v}_{\mathbf{blood,\ ven}}$ is the difference between the mean grayscale value in a major blood vessel (the superior

mesenteric is used as reference) in the venous contrast scan and the non-contrast scan. This approach assumes that the difference value in blood corresponds to 100% blood content, and thus the difference values in tissue regions scale blood content relative to this value. Arterial blood content was calculated similarly using the arterial phase scans.

To investigate the ability to predict treatment response using light-dose modeling, the CT images were converted into numerical meshes suitable for light propagation calculations. All image processing and modeling was done using NIRFAST [6, 44], an open-source light modeling package.

4.3 Fiber fiducial registration

The needle placement scans cannot be used as priors for light modeling, because of the low resolution which does not provide sufficient quality to delineate tissues. Additionally the scan is done with a small number of slices (only 6 per series) in order to minimize dose and without the use of contrast injection. Thus it is necessary to register the fiber fiducial locations from the needle placement scans onto the high resolution contrast CT scans. This is challenging, but is done by identifying reference locations in and around the pancreas on both sets of scans, and then performing an affine transformation on the sets of points. A rigid transformation is not sufficient due to the high degree of deformation seen between the two sets of scans. This deformation can be caused by patient position, breathing, or other movements. Additional deformation is caused by the grid placed on the chest of the patient to assist in needle placement. The reference locations used were on the tip of the spinal vertebrate, at the pancreas/air interface, and at the interface of the pancreas and the superior mesenteric blood vessel located next to the spinal vertebrate. The general affine transformation in 3D is: p2 =

A*p1 + B, where p2 and p1 are points in R^3, and the matrix A and the vector B define the transformation. If we have reference points in the needle placement scans, and in the high resolution scans, A and B can be found by minimizing p2 - A*p1 + B over the set of points. The resulting transformation can then be applied to the fiducial locations. Registration was performed for all three fibers. Figure 20 shows the results of fiducial location registration on one of the fibers. Figure 21 shows the fiducial locations in a volume rendering of the major blood vessels from the high resolution CT volume.

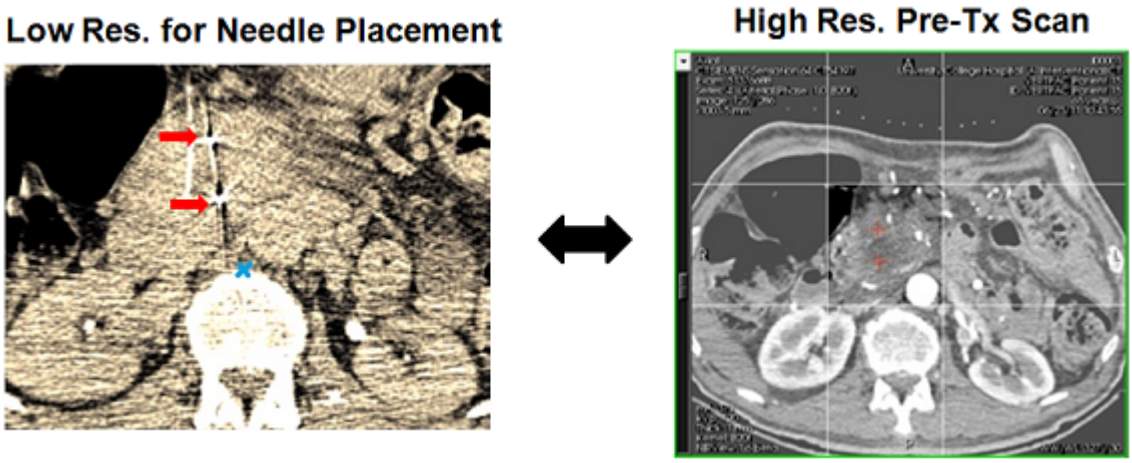

Figure 20. Fiducial locations present on the low resolution needle placement scans (left, shown by red arrows) are registered onto the high resolution contrast CT pre-treatment scans (right, shown by red + marks). The red markers indicate the fiducial locations, and the blue marker is the tip of the spinal vertebrate reference location used in image transformation.

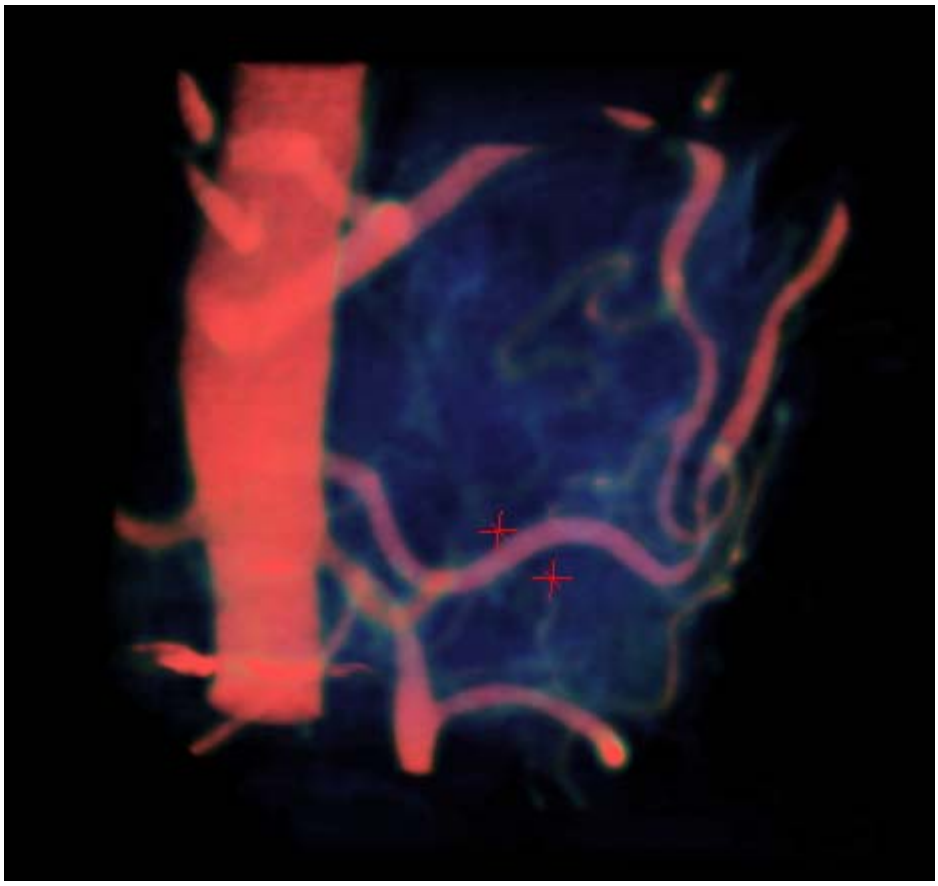

Figure 21. Fiducial locations identified as red plus signs in a volume rendering of the major blood vessels around the fiber location in the pancreas. The volume is derived from the high resolution CT scans.

4.4 Biliary stent artifact removal

Four of the patients in the VERTPAC-01 study had biliary stents which are visible in the CT scans and are located near the site of fiber placement. All four patients had a polyethylene Cotton Huibregtse stent (Figure 22) [69]. One of the patients additionally had a platinum/nickel titanium Boston Wallflex stent (Figure 23) [70].

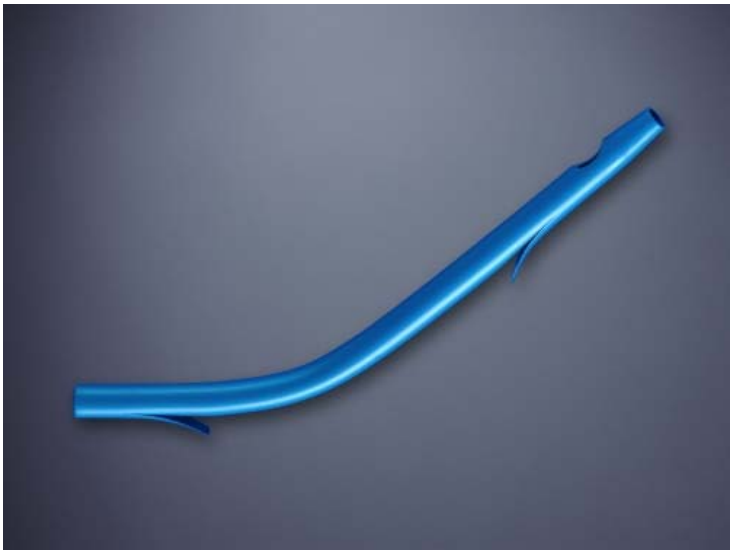

Figure 22. The polyethylene-based Cotton Huibregtse biliary stent used by four patients in the VERTPAC-01 trial. The purpose of the stent is to drain obstructed biliary ducts.

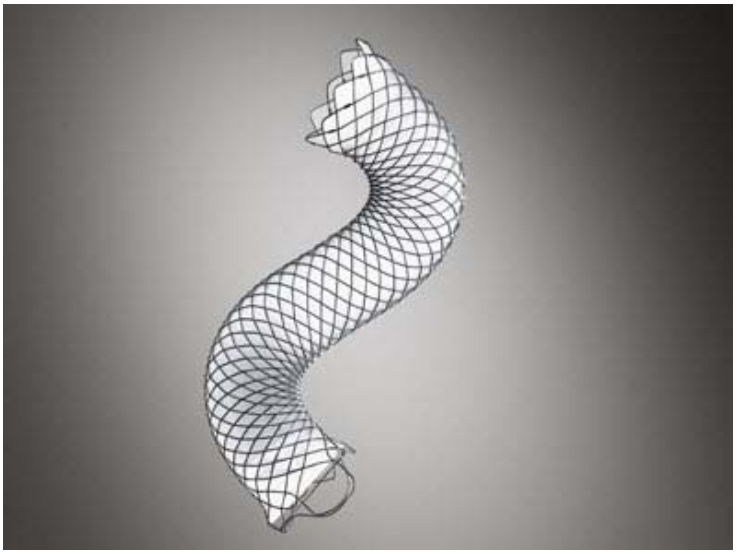

Figure 23. The platinum/nickel titanium Boston Wallflex biliary stent used by one patient in the VERTPAC-01 trial.

These biliary stents often produce CT beam-hardening artifacts characterized by radial striations around the stent location, as shown in Figure 24. In this study the Boston

Wallflex stent produced no significant artifacts, so only artifacts produced by Cotton Huibregtse stents were considered.

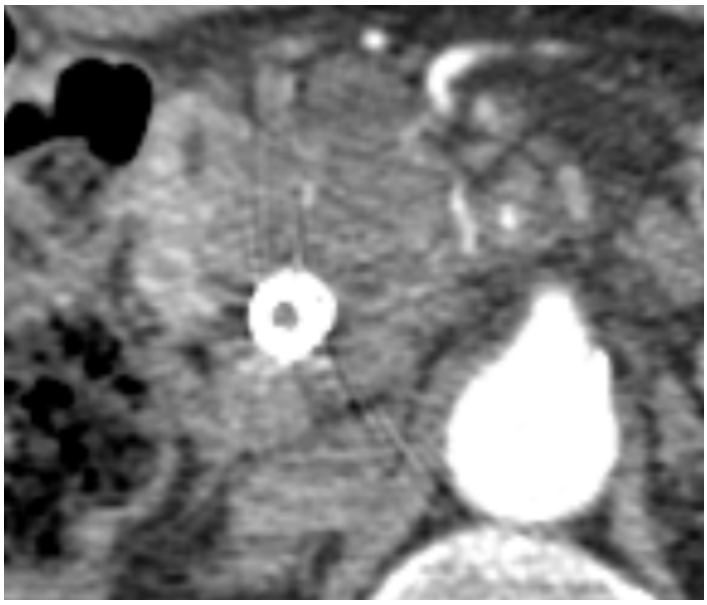

Figure 24. Contrast CT scans of a patient with the Cotton Huibregtse biliary stent, showing radial striation beam-hardening artifacts around the stent location. The stent is the bright ring near the center of the image.

These artifacts create two potential issues for using light modeling to predict treatment response to photodynamic therapy. Firstly, the artifacts perturb grayscale values around the fiber location, which are used to estimate optical and biological parameters in the patient. Secondly, the artifacts inhibit the proper segmentation of blood vessels and pancreatic tissues from the contrast CT scans. The artifact is low frequency, but of a similar frequency/magnitude to the heterogeneity seen in pancreatic tissue, making the application of conventional CT beam-hardening artifact removal methods

difficult. The following algorithm in Figure 25 describes the method used to remove the artifacts created by the stent from the CT scans.

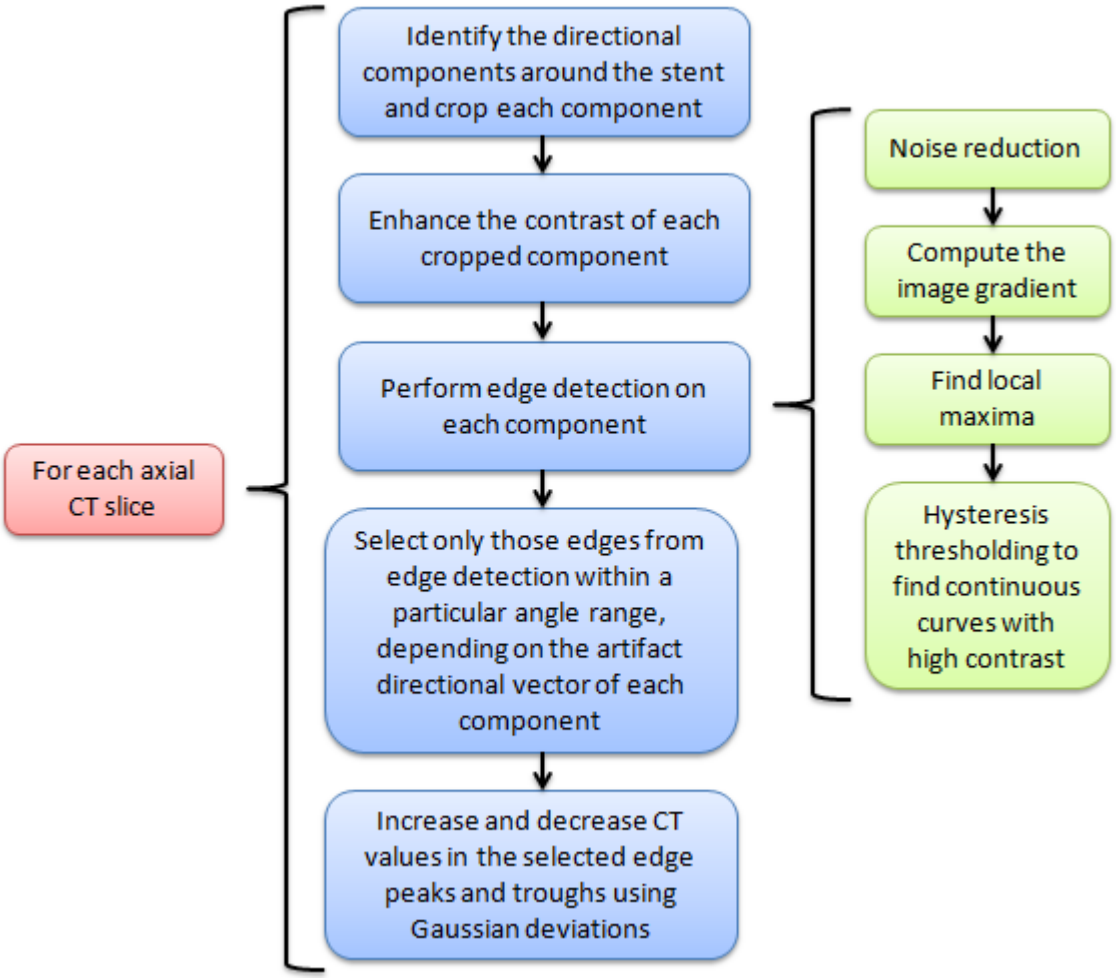

Figure 25. The algorithm used for removing beam-hardening artifacts caused by biliary stents in contrast CT scans.

The first step in the algorithm is identifying each directional component of the artifact around the stent, as illustrated in Figure 26.

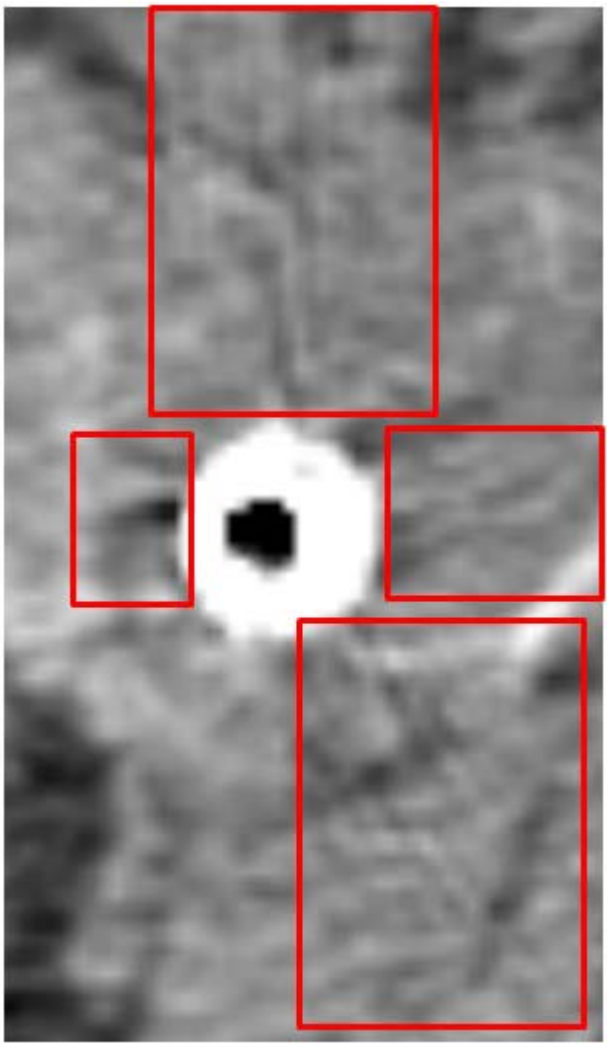

Figure 26. Contrast CT scans showing each identified directional component of the beam-hardening artifacts caused by biliary stents. The components are identified in red boxes indicating the crop extents.

Following this, the contrast of each component is enhanced and edge detection is applied to the image, as shown in Figure 27.

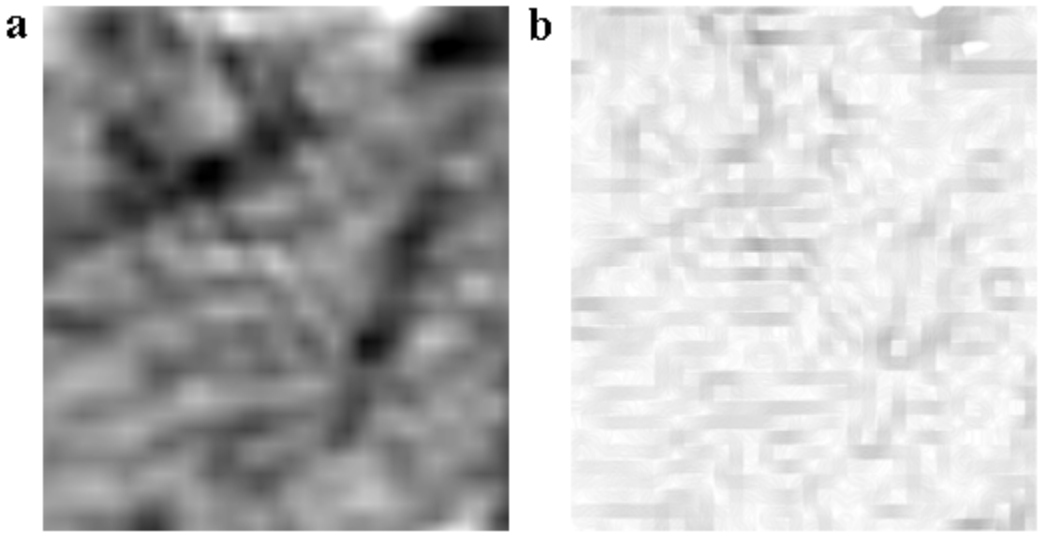

Figure 27. (a) A single cropped section of the contrast CT scans showing a directional component of the beam-hardening artifact caused by the biliary stent. (b) The same cropped section of the contrast CT scan after contrast enhancement and edge detection have been applied to the image.

This is followed by modifying the grayscale values of the image around the peaks and troughs of edges aligned with the direction of the artifact. Values are changed according to a Gaussian profile perpendicular to the direction of the artifact, with the center of the Gaussian at a peak or trough in the image, and width relative to the edge width. The final results of artifact removal are displayed in Figure 28.

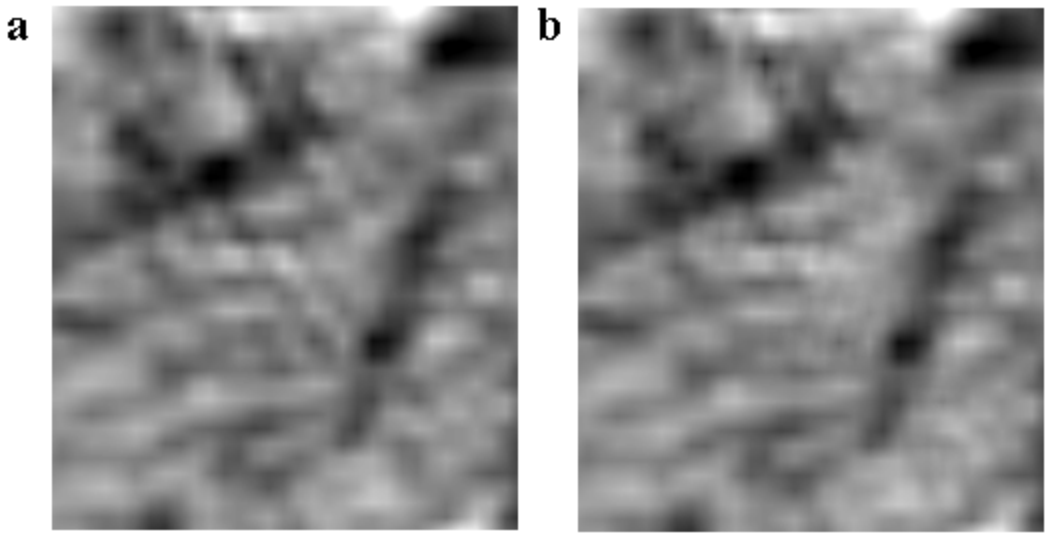

Figure 28. (a) A single cropped section of the contrast CT scans showing a directional component of the beam-hardening artifact caused by the biliary stent. (b) The same cropped section of the contrast CT scan after the artifact removal algorithm has been applied to the image.

In order to account for overall grayscale bias and avoid the assumption that the biliary stent artifacts have no net change to grayscale mean values, each component is adjusted by gradient. This gradient is equal to the net bias of the artifact at a particular column/row of the image, as compared with tissue regions unaffected by the artifact. Figure 29 shows the net bias produced by the artifact at different column locations in the image for a patient.

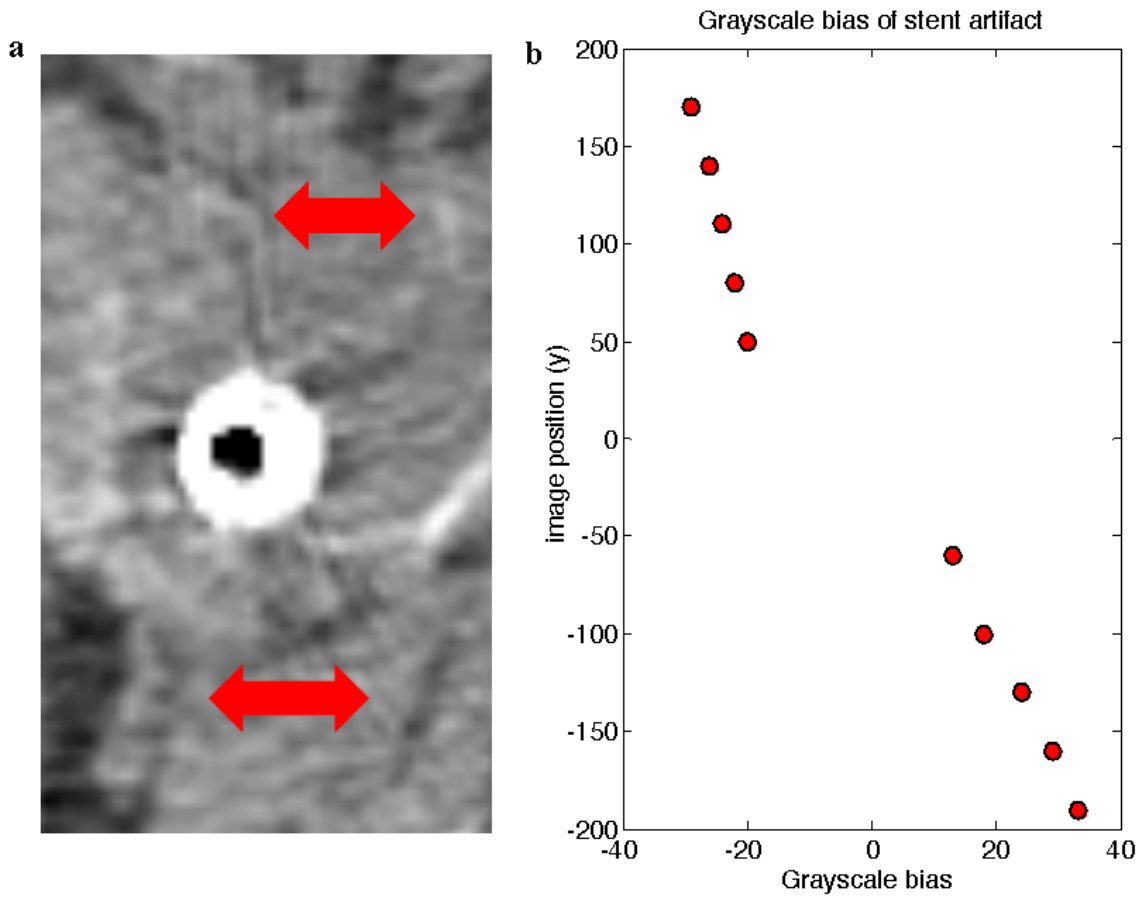

Figure 29. (a) A single cropped section of the contrast CT scans showing the beam-hardening artifact caused by the biliary stent. The bidirectional red arrows indicate measurement locations affected by the artifact and unaffected by the artifact. (b) The grayscale bias of the stent artifact at different vertical positions in the image.

4.5 Segmentation of tissue types

After the fiducial markers have been registered onto the high resolution pre-treatment CT scans, these scans are then segmented to classify pancreas tissue, blood vessels, and air. First the medical images are cropped around the pancreas. This is meant to reduce computational time in segmenting tissue types, creating a tetrahedral mesh from the resulting segmentation, and running simulations on the mesh, by reducing the volume of

interest. The area around the pancreas is then segmented using a K-Means and Markov random field filter, which groups clusters of common grayscale values to identify different regions. To separate air, pancreas tissue, and blood vessels, 3 classes were used for this filter. An error tolerance of 0.001 was used, with 100 maximum iterations. These two parameters help control the computational time. A smoothing factor of 1 was used, which helps controls the effect of noise on distinct volumes. Next iterative hole filling was applied to eliminate holes in each region and improve smoothness. A desired hole radius of 1 pixel was used, with 10 maximum iterations. A majority threshold of 1 was used, which specifies the number of pixels over 50% required to fill a pixel during each iteration of the hole filling process. The majority threshold parameter controls the curvature of the target holes. Finally the segmentation was manually touched-up to fix any remaining issues such as stray pixels or artifacts misclassified as blood vessels. Figure 30 shows a slice of the resulting segmentation of tissue types around the pancreas. Figure 31 shows the NIRFAST interface used for creating the segmentation from the CT scans.

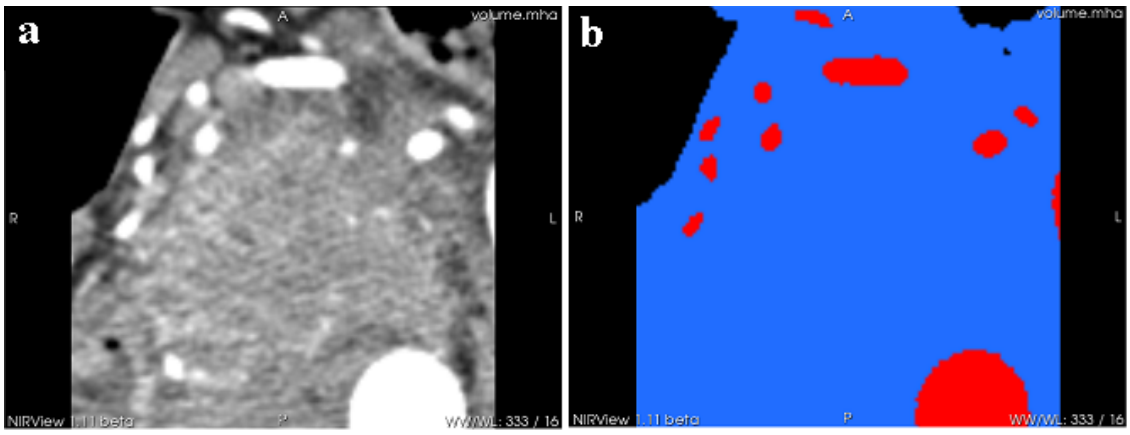

Figure 30. (a) A single axial DICOM slice around the pancreas is shown. Bright areas are contrast enhanced major blood vessels, while the dark areas in the top left and right are air. The remaining

area is pancreas tissue or surrounding tissue. (b) Segmentation of the pancreas area into tissue types. Blue is pancreatic tissue, red indicates blood vessels, and black is air.

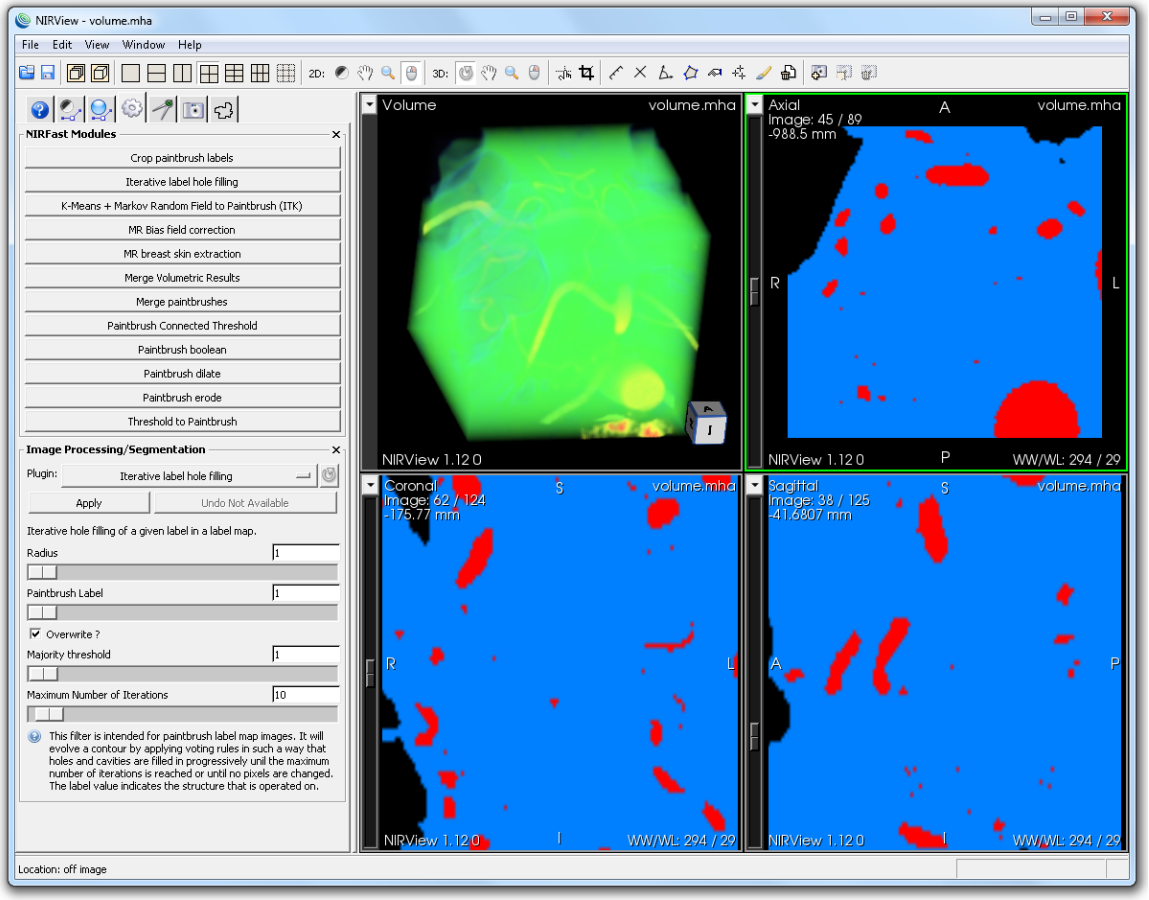

Figure 31. The NIRFAST interface for segmenting medical images into different tissue types, for use in creating the 3D tetrahedral mesh used for light modeling. The top left view shows a 3D volume rendering of the medical images, while the other three views show the 2D orthogonal views of the segmentation overlaid on the medical images. On the left menu are the various tools used for segmentation and image processing.

4.6 Tetrahedral mesh creation

After segmenting tissue types, a 3D tetrahedral mesh is then created using the meshing tools available in NIRFAST as shown in Figure 32. This process is automatic, with

default values for all relevant parameters, but also allows the user to modify these parameters or refine the mesh if desired. The values used for tetrahedral facet size varied between 0.8 and 1.4mm for the patients. The fiducial markers that were placed are used to identify the extents of the light-emitting fiber. This fiber is modeled as a distributed source that is a very thin cylinder, using a 'pdt_fiber' module available with NIRFAST, created for this purpose. Figure 33 shows the NIRFAST interface used for creating the model for the source fiber.

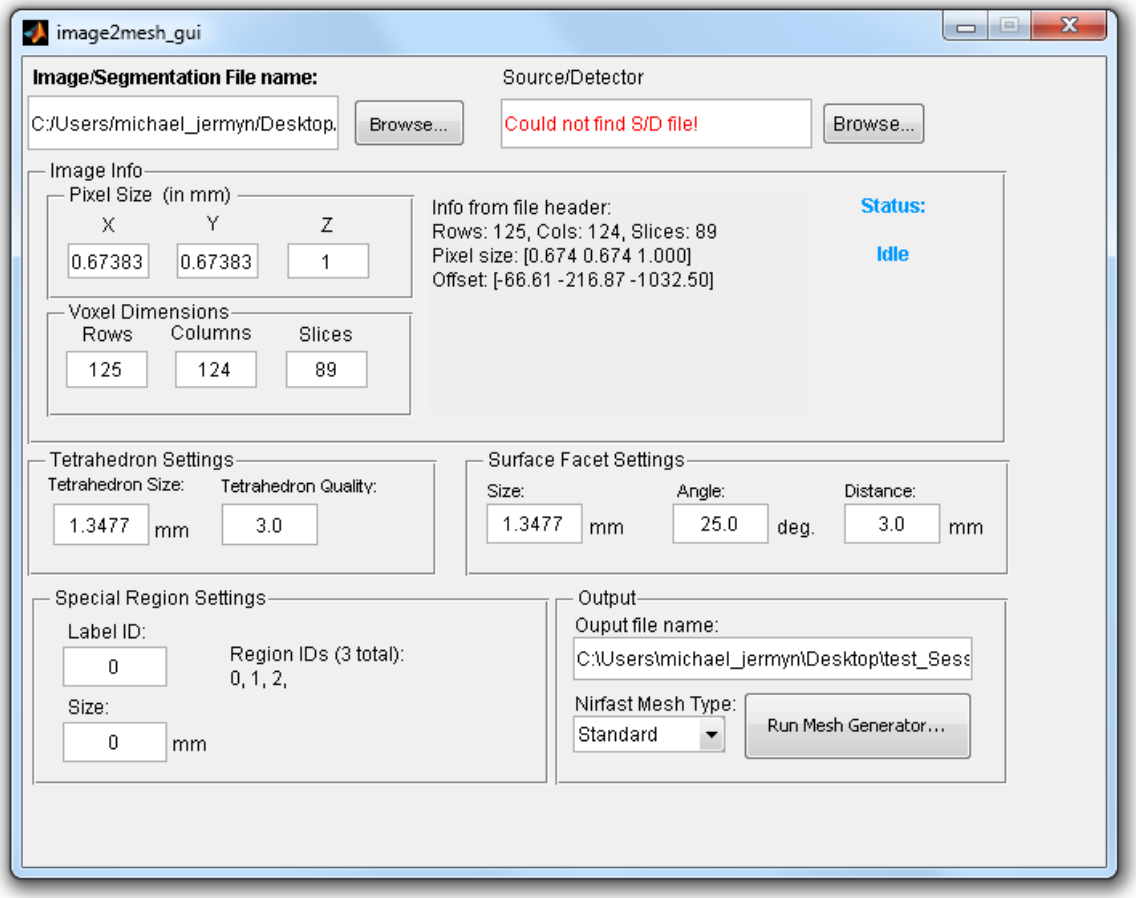

Figure 32. The NIRFAST interface for creating a 3D tetrahedral mesh from a stack of 2D segmentations. There are parameters for controlling element size, quality, and surface facet attributes.

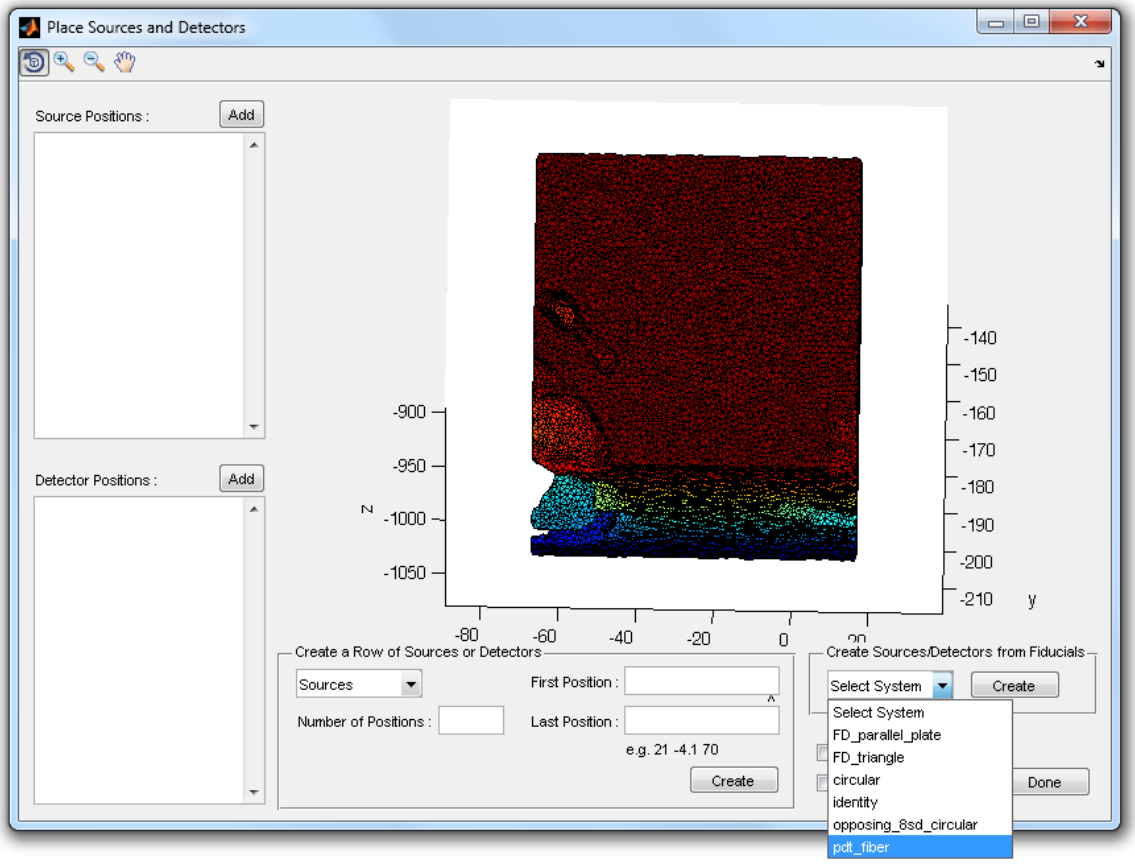

Figure 33. The NIRFAST interface for defining the light source attributes. A custom module 'pdt_fiber' was created specifically for modeling the light-emitting fiber used in the VERTPAC-01 study.

Figure 34 shows the tissue segmentation alongside the original medical images for a representative patient, and the resulting tetrahedral mesh. The volume considered contains the pancreas and nearby blood vessels, and was chosen to be large enough to ensure the boundaries have little effect on the light propagation modeling in the regions of interest.

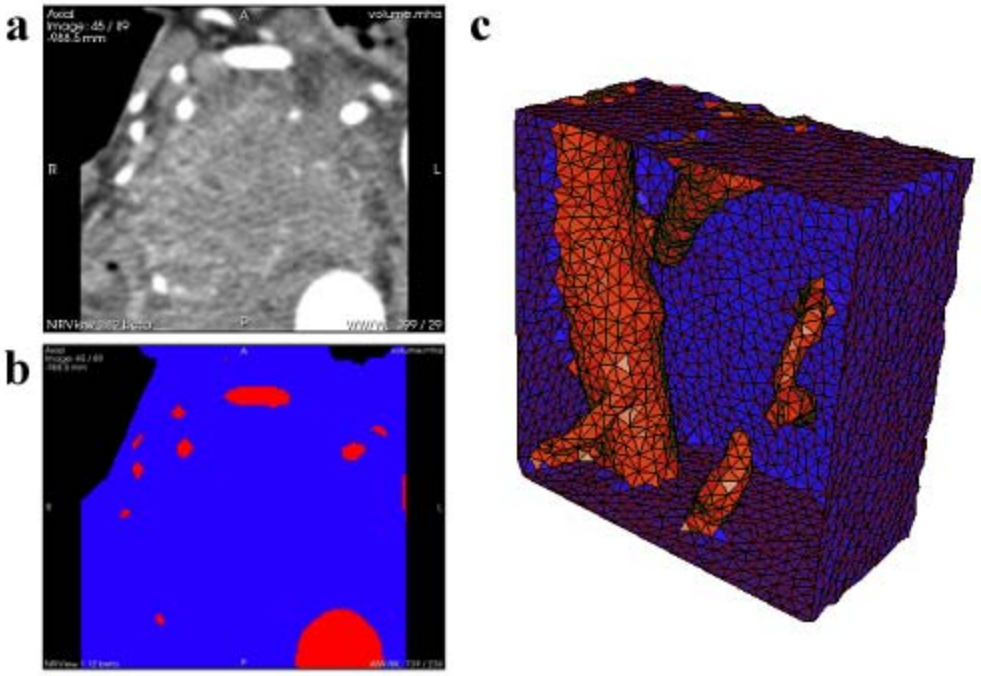

Figure 34. (a) A single axial DICOM slice of the pancreas and surrounding tissue is shown from the pre-treatment contrast CT scans. Bright areas are indicative of contrast enhanced major blood vessels, while the dark areas in the top left and top right are air. (b) Segmentation of the same axial slice into different regions based on tissue type: blue is pancreatic or surrounding tissue, red is blood vessels, and black is air. (c) Rendering of a 3D tetrahedral mesh of the pancreas and surrounding tissue in blue, and blood vessels in red. It is clipped by a plane to visualize the interior of the mesh.

4.7 Assigning optical properties and modeling

The venous and arterial blood content values were used to estimate optical absorption in the pancreas tissue and blood vessels based on known chromophore extinction spectra and estimates of venous and arterial oxygenation, in the following manner:

$$C_{deoxyHb} \simeq (1- R_{SO2,\,ven})*(v_{tissue,\,ven}/v_{blood,\,ven}) + (1- R_{SO2,\,art})*(v_{tissue,\,art}/v_{blood,\,art}) \quad (11)$$

$$C_{HbO} \simeq R_{SO2,\,ven}*(v_{tissue,\,ven}/v_{blood,\,ven}) + R_{SO2,\,art}*(v_{tissue,\,art}/v_{blood,\,art}) \quad (12)$$

$$\mu_a(\lambda=690nm) = \varepsilon_{water}*C_{water} + \varepsilon_{deoxyHb}*C_{deoxyHb} + \varepsilon_{HbO}*C_{HbO} \quad (13)$$

Here $C_{deoxyHb}$ and C_{HbO} are the concentration of deoxy-hemoglobin and oxy-hemoglobin respectively. $R_{SO2,\,ven}$ and $R_{SO2,\,art}$ are the blood oxygen saturation for venous and arterial phase, using literature values of 0.70 and 0.99 respectively [71-75]. ε is the molar absorption coefficient for each absorber at the wavelength of light used. Literature values of 0.5mm^{-1} and 0.98mm^{-1} were used for the reduced scattering coefficient in blood vessels and pancreatic tissue respectively [76-79]. These optical properties were assigned in the numerical mesh and the light distribution from the diffusing-tipped fibers was calculated using the NIRFAST interface shown in Figure 35, producing a light fluence field around the fiber location. Fluence fields were then converted into maps of light dose by scaling to the total energy distributed for each patient.

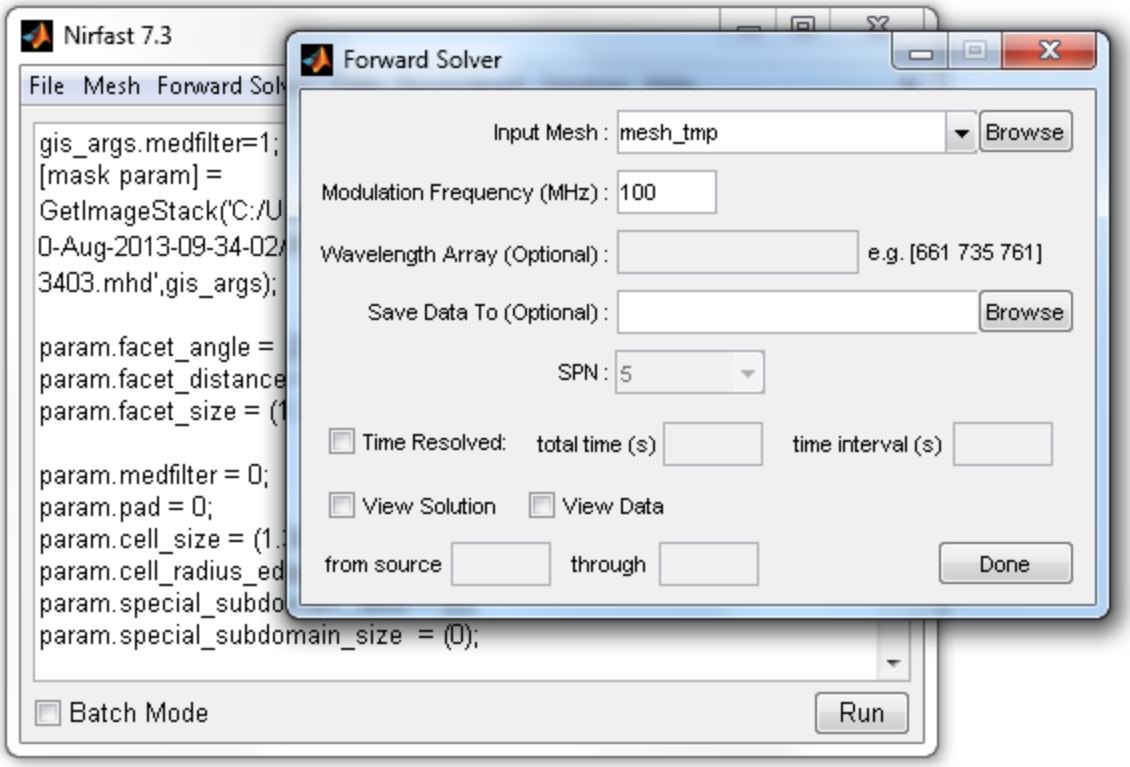

Figure 35. The NIRFAST interface for modeling near-infrared light transport in tissue.

4.8 Calculating necrotic volume

The post-treatment CT scans were used to identify the region of necrosis caused by treatment, distinguished as a dark area around the fiber location. Using guidance from radiologist-determined values of the two major diameters of necrosis, the necrotic volume was estimated for each patient. The necrotic region was segmented in each slice of the post-treatment CT scans in which necrosis was visible. The segmentation was then used to determine necrotic volume by computing the relevant volume contained by the segmentation in NIRFAST. Table 5 shows the radiologist-determined values for the two major diameters of the necrotic region of each patient.

Patient Number	Two major diameters of necrosis [cm, cm]
1	No Change
2	No Change
3	No Change
4	1.1, 1.3
5	0.7, 0.4
6	No Change
7	0.7, 0.5
8	2.0, 1.6
9	1.8, 0.7
10	2.0, 1.6
11	2.5, Not reported
12	No Change
14	1.7, 2.0
15	3.6, 4.0
16	3.0, 2.8

Table 5. (a) The radiologist determined values for the two major diameters of the region of necrotic tissue for each patient, as determined from post-treatment CT scans. No Change indicates that no necrosis was observed post-treatment. The second major diameter for Patient 11 was not determined.

Figure 36 (a) – (c) show a representative workflow for obtaining the necrotic volume for the post-treatment CT scan for one patient. Necrotic volumes determined for all patients, categorized by light energy delivered, are plotted in Figure 36 (d), and show a clear increase in necrotic volume vs. energy.

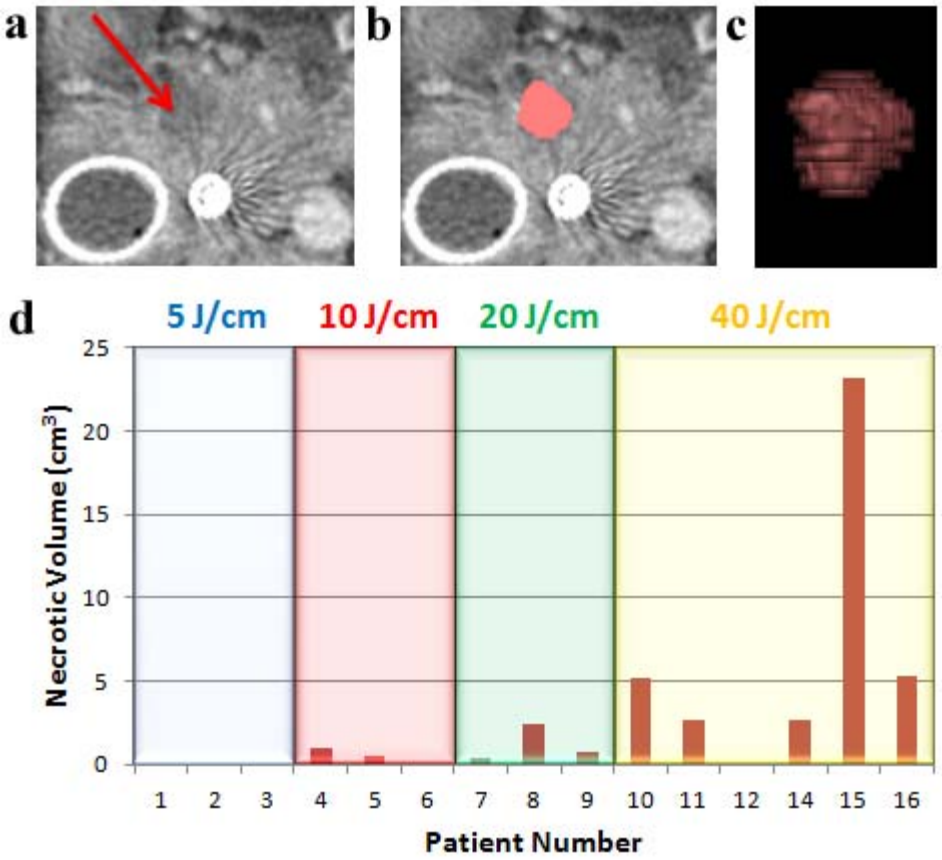

Figure 36. (a) A single axial slice of the pancreas from the post-treatment CT scans, indicating the dark area in the center as necrotic tissue. The two bright rings are biliary stents. (b) The same slice showing the segmentation of the necrotic tissue in pink. (c) A volume rendering of the segmentation of the necrotic volume. (d) The volume of the necrotic tissue region is shown for each patient in the study, as determined from the segmentation of the post-treatment CT scans. Energy delivered per cm of fiber size is shown for each patient. Note that 2 fibers were used for patient 16, and 3 fibers for patient 15. Each of the fibers for patient 15 were 2cm in length as opposed to the 1cm norm. Necrotic volume for patient 12 could not properly be measured due to pre-existing necrosis prior to treatment.

4.9 Contrast-derived venous blood content correlates with necrotic volume

Figure 37 (a) shows a plot of necrotic volume plotted as a function of the venous blood content values derived from contrast CT information. The three patients administered 5J/cm energy of light were omitted from analysis because there was no visible necrosis in the post-treatment scans, under the presumption that this energy level was too low to produce necrosis in human tissue. Patient 7, administered 20J/cm, was omitted because no pre-treatment arterial scan was acquired for that patient. Patient 12 was omitted because there was pre-existing necrosis prior to treatment, hampering the ability to measure necrosis caused by treatment. These data were re-analyzed by normalizing the necrotic volume based on energy delivered. Normalized necrotic volumes are plotted vs. venous blood content in Figure 37 (b). This approach produces a very high correlation with between these parameters ($R^2 = 0.85$). Note that these results are without the use of biliary stent CT artifact removal. Using artifact removal produces a correlation of $R^2 = 0.90$.

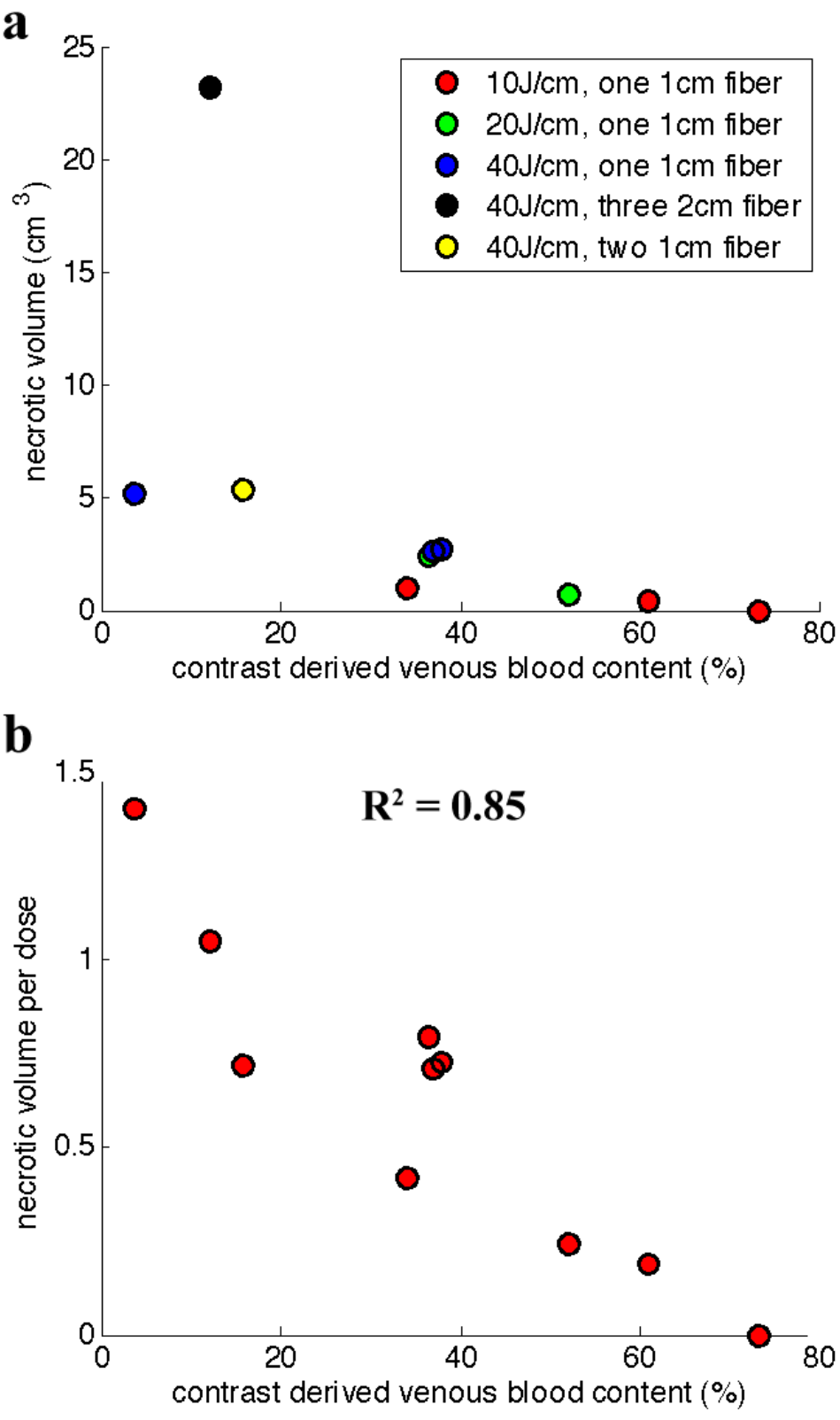
a
10J/cm, one 1cm fiber
20J/cm, one 1cm fiber
40J/cm, one 1cm fiber
40J/cm, three 2cm fiber
40J/cm, two 1cm fiber
necrotic volume (cm 3)
contrast derived venous blood content (%)
b
R² = 0.85
necrotic volume per dose
contrast derived venous blood content (%)

Figure 37. (a) Correlating necrotic volume with venous blood content, as derived from the contrast CT scans. (b) Necrotic volume is normalized as V/(n*d*log(E)), where V is the necrotic volume in cm^3, n is the number of fibers used in treatment, d is the fiber size in cm, and E is the energy delivered over the fiber in J/cm. This is then correlated with the contrast derived venous blood content.

4.10 Light modeling results correlate with necrotic volume

The light dose maps produced from light modeling can be used to estimate necrotic volume provided a suitable energy threshold value is determined. In this study, the threshold value is unknown, therefore, we determined the threshold value which exhibited the strongest correlation between predicted and measured volume of necrosis. This value was found to be $0.003 J/cm^3$, and defines a 3D contour of values greater than the threshold in the 3D light dose maps for each patient, which then defines an estimated volume of necrosis. Figure 38 shows visualizations of the light dose in a patient produced by light modeling, for use in estimating necrotic volume. Figure 39 demonstrates the strong correlation between predicted and measured necrotic volume using this value. Note that these results are without the use of biliary stent CT artifact removal. Using artifact removal produces a correlation of $R^2 = 0.92$.

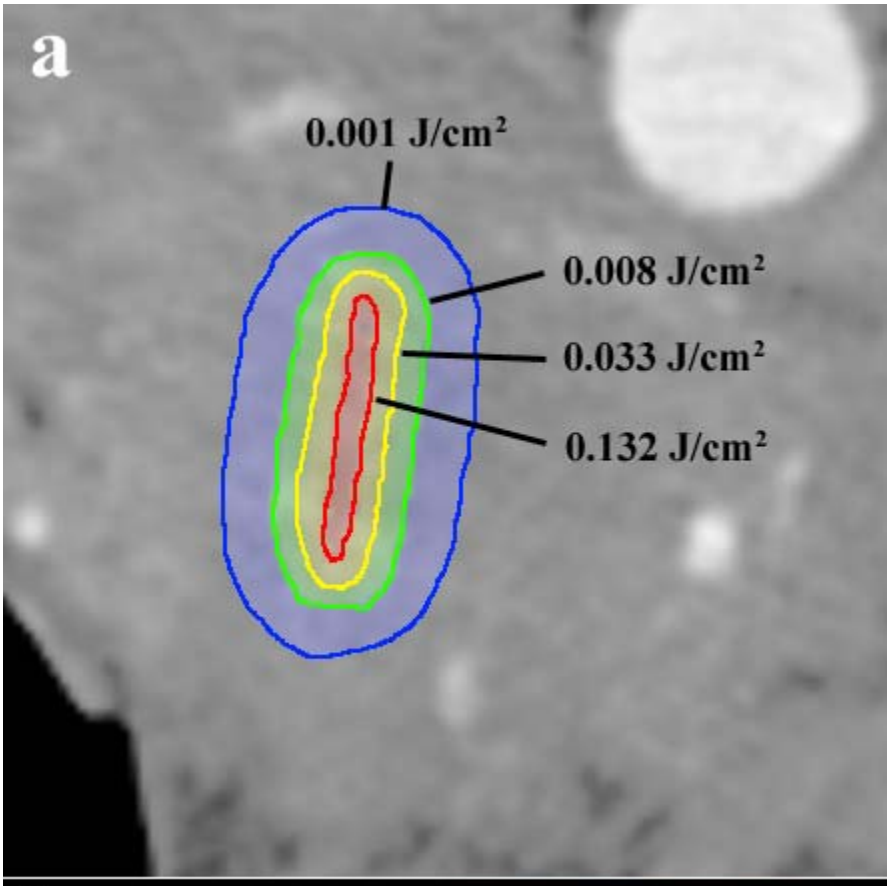
a
0.001 J/cm²
0.008 J/cm²
0.033 J/cm²
0.132 J/cm²

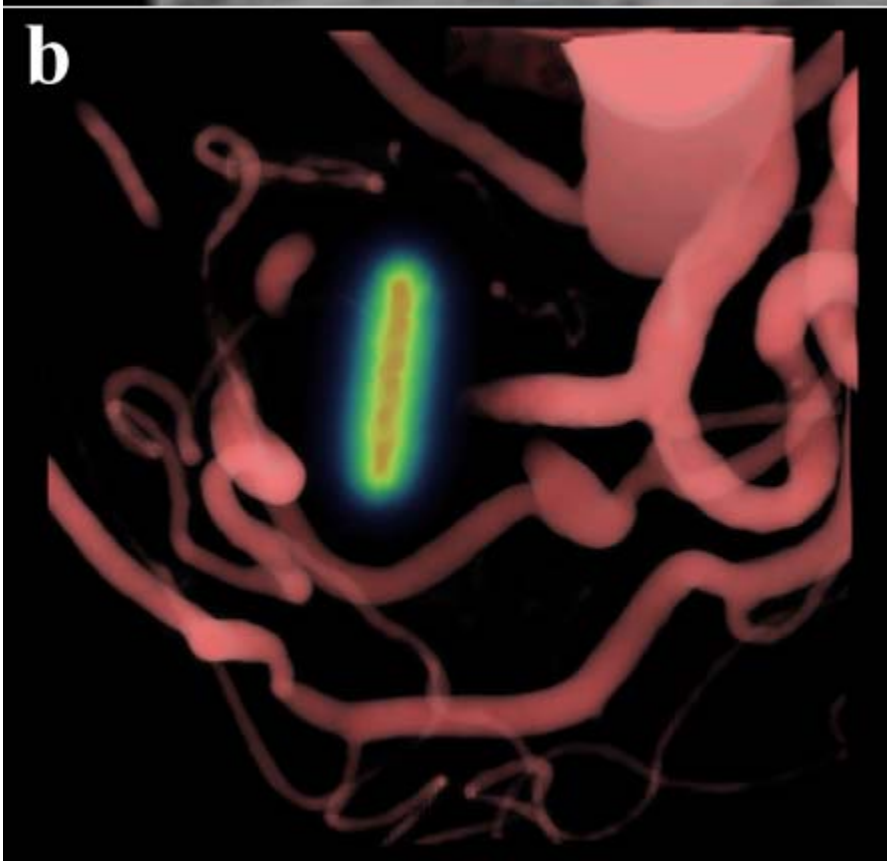
b

Figure 38. (a) A single axial slice of the pancreas from the pre-treatment CT scans is overlaid with computed contours of light fluence levels around the fiber location. This was simulated using blood content information for tissue absorption from contrast CT. (b) The fluence of the light-emitting fiber in a volume rendering of the area around the fiber in the pancreas, identifying major blood vessels.

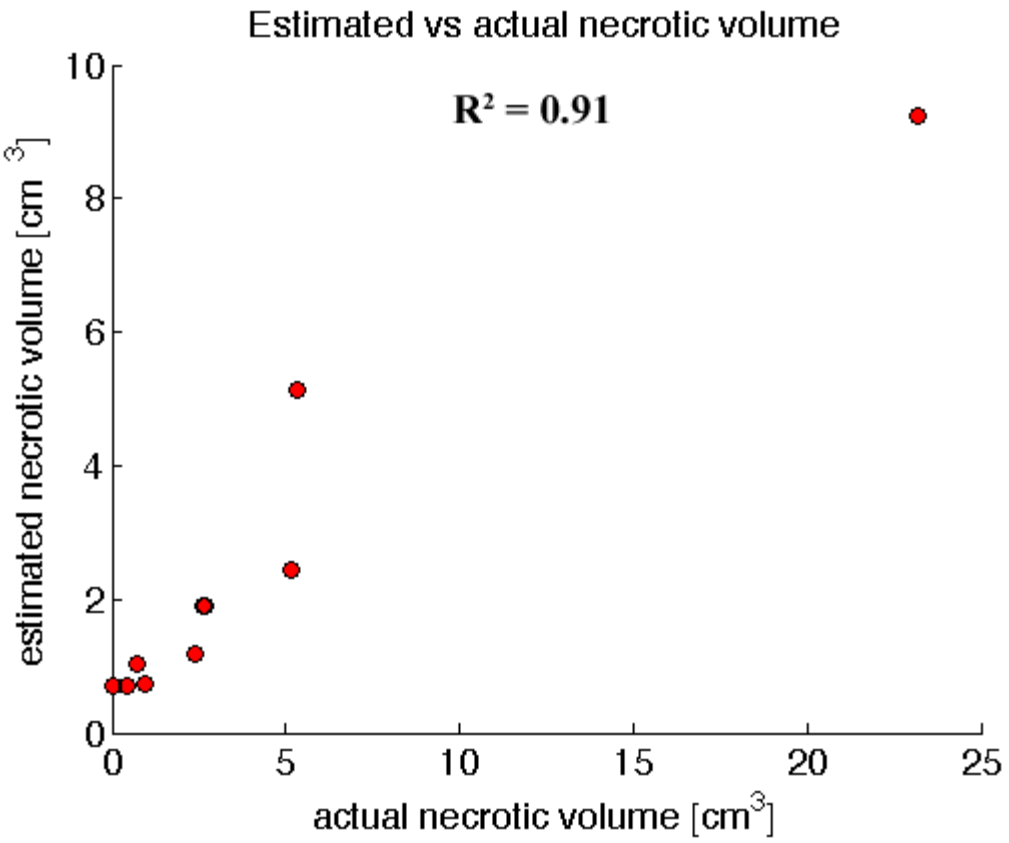

Figure 39. Correlating actual necrotic volume with the estimated necrotic volume from light modeling, using absorption values estimated from contrast CT information and literature values for scattering. A particular energy threshold, 0.003J/cm^3, with the highest correlation was picked to determine the estimated necrotic volume using the contour defined by this threshold.

4.11 Light modeling sensitivity analysis

The effect on light fluence from the presence of a nearby blood vessel was studied, using a simulated blood vessel of diameter 1cm. Figure 40 shows that the effect on light fluence is less than 2% if the blood vessel is at least 1.2cm away from the fiber. This minimum distance is maintained for all of the patients in this study, suggesting that it is likely unnecessary to segment and model blood vessels separately from pancreatic tissue. This could reduce the amount of time required to produce surrogate dosimetry information for estimating treatment response.

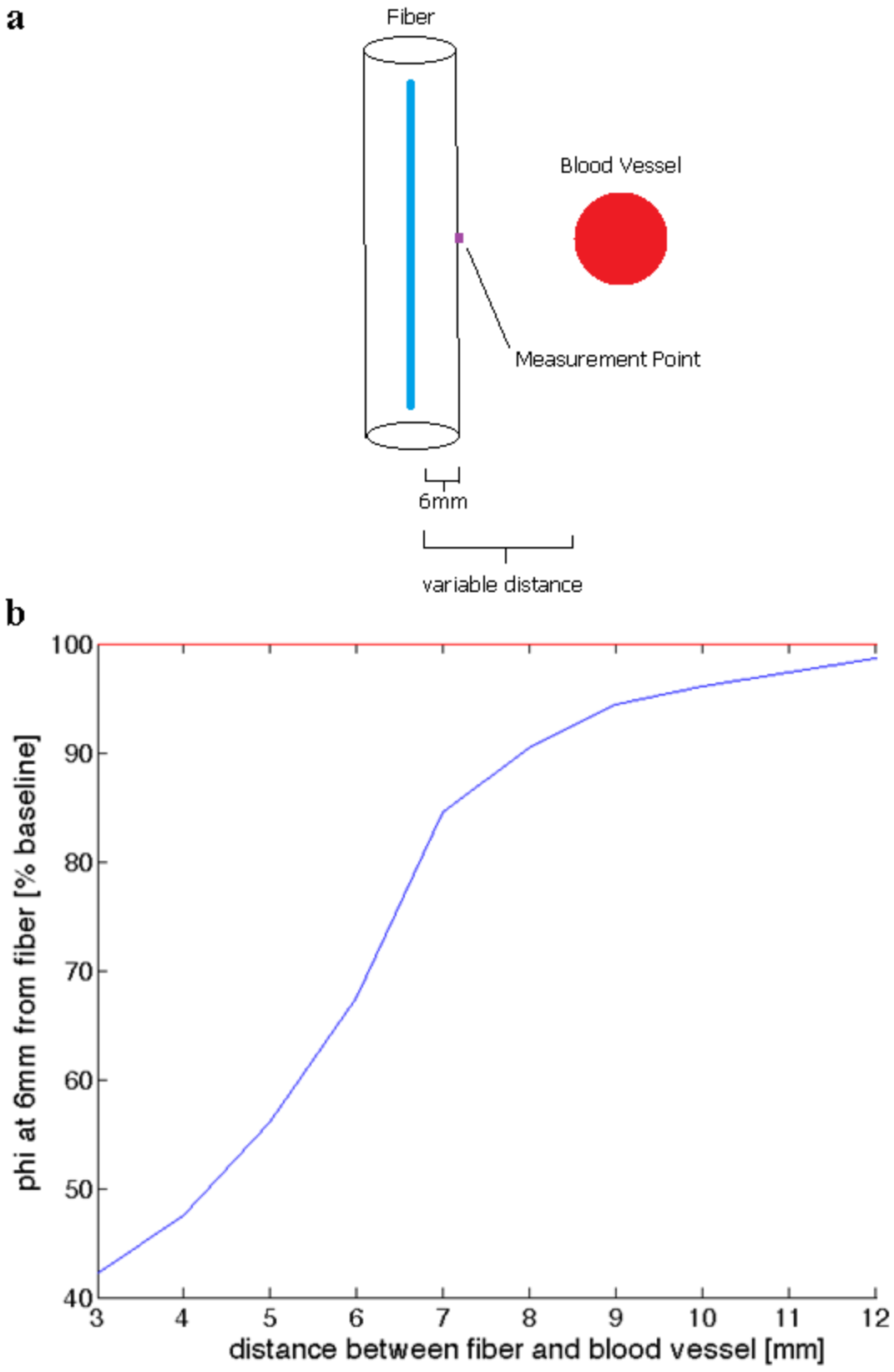
a
Fiber
Blood Vessel
Measurement Point
6mm
variable distance
b
100
90
80
70
60
50
40
phi at 6mm from fiber [% baseline]
3
4
5
6
7
8
9
10
11
12
distance between fiber and blood vessel [mm]

Figure 40. The effect of a nearby blood vessel on the light fluence field produced from light modeling. (a) Diagram of the relative locations of the blood vessel, light-emitting fiber, and point of measurement in the light fluence field. (b) Relative effect on the light fluence field, as compared with the light fluence unperturbed by the presence of a blood vessel.

There is a high amount of deformation observed between different sets of CT scans for the same patient. This is caused partly by biological functions such as breathing and motion, and also due to the needle placement grid used immediately prior to treatment. The grid compressed the chest, which deformed the body in the low resolution scans taken during needle placement. Due to this deformation, it is difficult to register scans in order to determine biological parameters or optical properties, for use in estimating necrotic volume. Therefore it is useful if pancreatic optical properties can be modeled homogeneously rather than heterogeneously. To determine this, a heterogeneous map of optical absorption was calculated based on an attempt to properly register pre- and post-contrast CT scans. The estimated necrotic volume determined using this map was compared with using a homogeneous map instead, with absorption equal to the mean value of the heterogeneous map. The same comparison was made for many different magnitudes of possible heterogeneous maps, by scaling the optical absorption values in the original heterogeneous map. The results are shown in Figure 41, along with a range specifying the expected amount of heterogeneity among the 15 patients, based on registration attempts. Within the expected range, there is less than 1% deviation observed in the estimate of necrotic volume. This indicates that it is reasonable to use bulk values for absorption in estimating necrotic volume produced by photodynamic therapy in the pancreas.

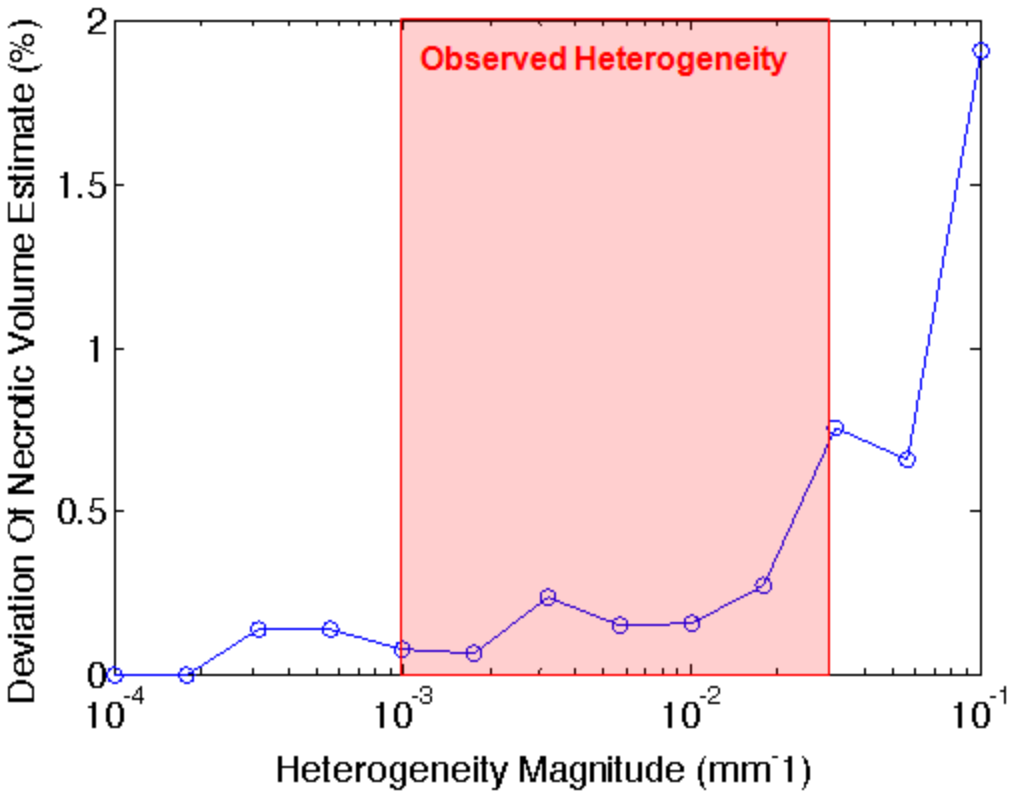

Figure 41. The effect of optical heterogeneity on estimated necrotic volume, as compared with optical homogeneity. The observed heterogeneity specifies the range of expected optical heterogeneity, as determined from the pre- and post-contrast CT scans of the 15 patients.

Figures 42-44 show the sensitivity of simulation-based necrotic volume estimates to changes in the bulk values of optical properties. Absorption and venous blood oxygen saturation have much more of an effect on the estimate for necrotic volume than reduced scattering, within expected ranges. The sensitivity graphs indicate that it is important to have good estimates of optical properties and biological parameters for accurate dosimetry.

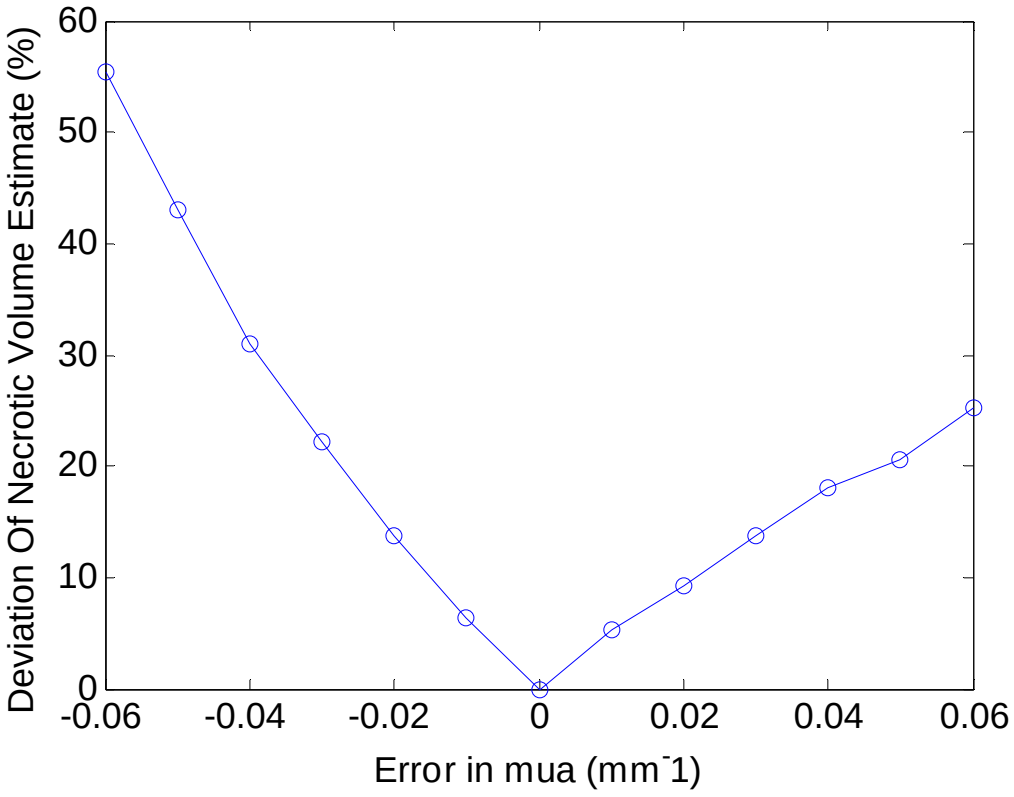

Figure 42. The effect of the absorption value used for optical simulation on estimated necrotic volume, as compared with a representative absorption value for the patients of 0.087mm^{-1}.

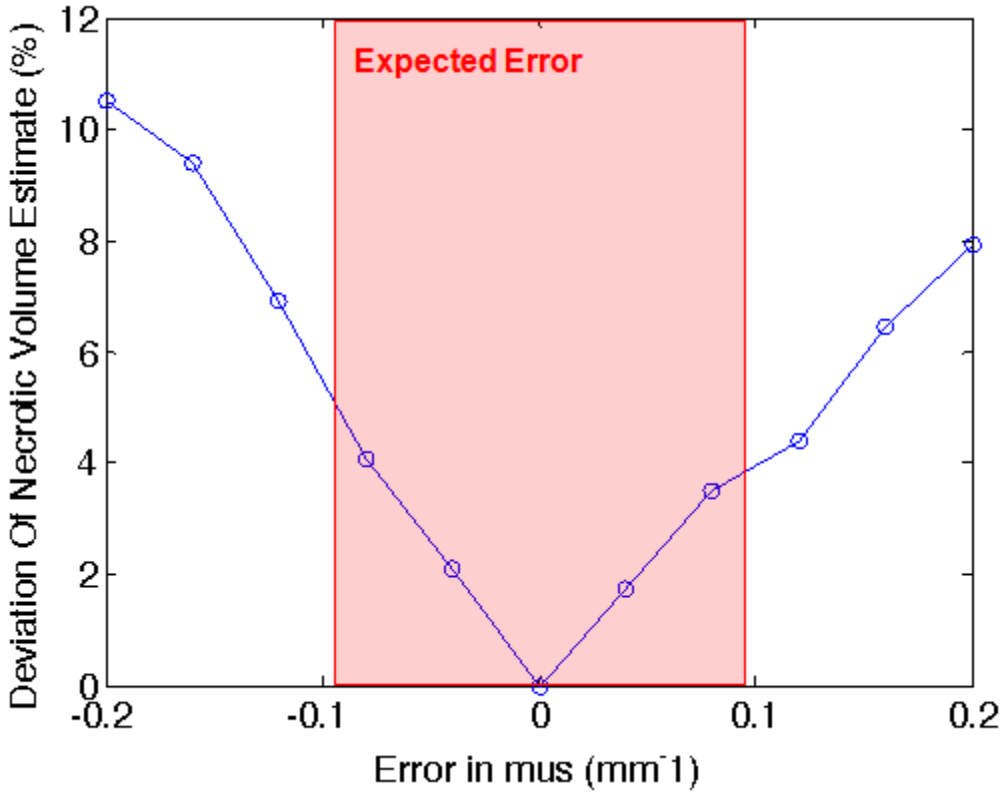

Figure 43. The effect of the reduced scatter value used for optical simulation on estimated necrotic volume, as compared with a literature-based reduced scatter value of 0.5mm^{-1} in pancreatic tissue and 0.98mm^{-1} in blood vessels. The expected error range indicates the range of values found in literature for the pancreas for reduced scattering.

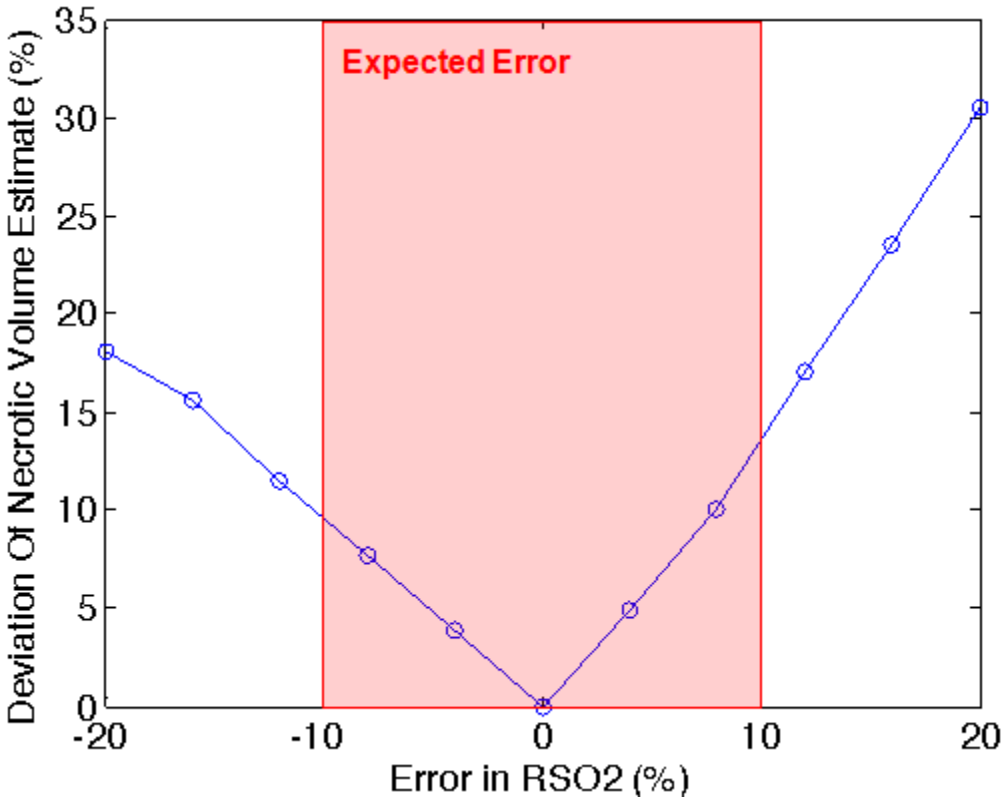

Figure 44. The effect of the venous oxygen saturation value used for optical simulation on estimated necrotic volume, as compared with a literature-based value of 70%. The expected error range indicates the range of values found in literature for venous blood oxygen saturation.

5. Discussion

Contrast derived venous blood content shows a high correlation with necrotic volume, with an R^2 value of 0.85. This suggests that the optical attenuation produced by venous blood content is a dominant factor in treatment response to photodynamic therapy in the pancreas as opposed to photosensitizer concentration. A strong correlation was observed between the volume of necrosis calculated using this surrogate estimate of venous blood content and standard light modeling tools and that measured by post-treatment CT, with an R^2 value of 0.91. This observation indicates that light attenuation, specifically that derived from venous blood, dictates the treatment volume for this therapy, and implies that this response can be reliably predicted using contrast CT. This would represent a major breakthrough in PDT for pancreas cancer and could facilitate light dose administration tailored to individual patients. .

A prior clinical pilot study for the use of photodynamic therapy in pancreatic cancer reported necrotic volume and energy delivered for 16 patients [17]. Correlating the logarithm of energy delivered vs. necrotic volume of these patients results in an R^2 value of 0.37 (larger than without taking the logarithm). Similarly, correlating the logarithm of energy delivered vs. necrotic volume in the VERTPAC-1 study gives an R^2 value of 0.67. Both of these values are considerably weaker than the R^2 values reported herein. This suggests that there is significant value in using contrast derived venous blood content to aid in predicting necrotic volume produced by treatment, rather than relying on estimates based upon energy delivered.

Raw venous grayscale values were compared with necrotic volume to determine whether pre-contrast CT scans are essential to the correlation observed between contrast-derived venous blood content and necrotic volume. Figures 45 and 46 show the correlation using venous grayscale values in the tumor location of the post-contrast CT scans (normalized by blood values for Figure 46). In both cases there is no correlation, indicating that both pre- and post-contrast CT scans are needed for producing a strong correlation to estimate necrotic volume.

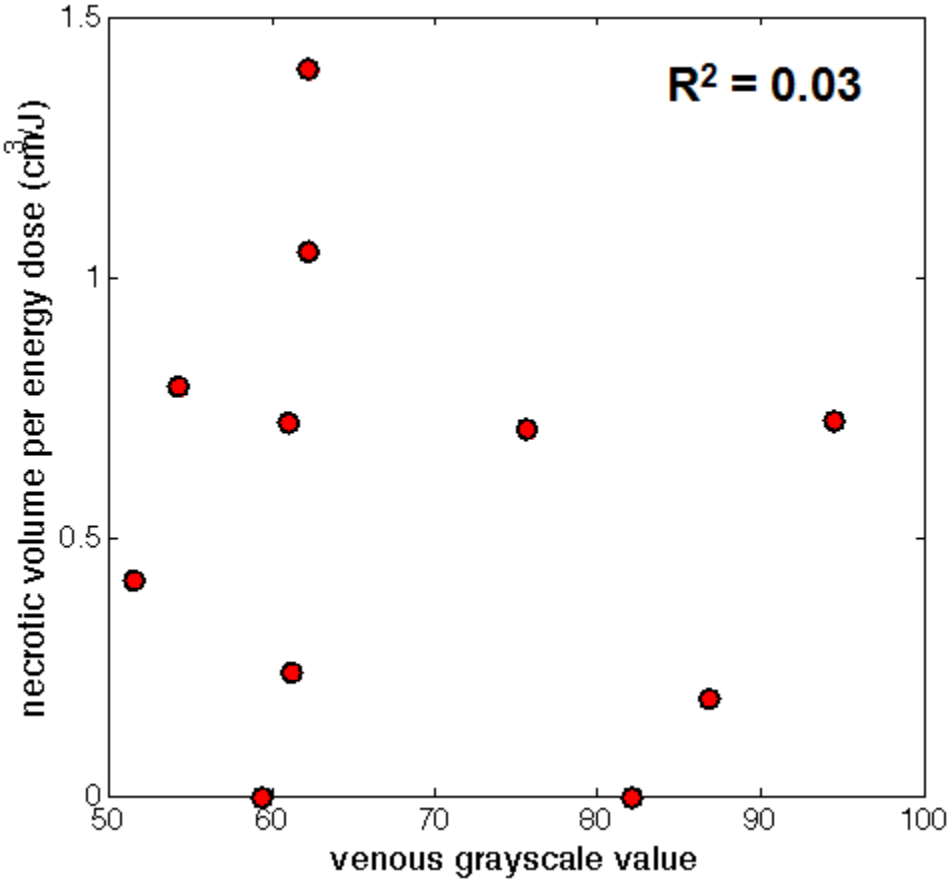

Figure 45. Correlating necrotic volume with venous grayscale values, as obtained from the post-contrast CT scans. Necrotic volume is normalized as V/(n*d*log(E)), where V is the necrotic volume in cm^3, n is the number of fibers used in treatment, d is the fiber size in cm, and E is the energy delivered over the fiber in J/cm.

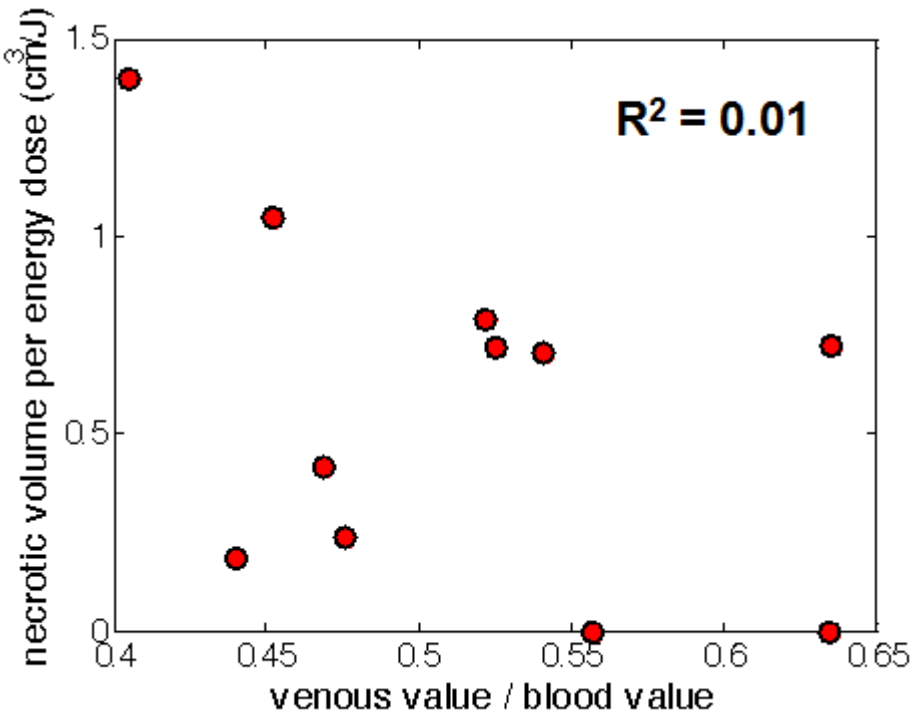

Figure 46. Correlating necrotic volume with venous grayscale values, as obtained from the post-contrast CT scans. Venous grayscale values are normalized by the grayscale values in a major blood vessel. Necrotic volume is normalized as V/(n*d*log(E)), where V is the necrotic volume in cm^3, n is the number of fibers used in treatment, d is the fiber size in cm, and E is the energy delivered over the fiber in J/cm.

Information from contrast CT provides the opportunity to assist in pre-treatment planning for photodynamic therapy of pancreatic cancer. Contrast derived venous blood content displays a significant correlation with necrotic volume, with an R^2 value of 0.85, indicating that light attenuation is the dominant factor in treatment response in the pancreas. Concomitantly, light modeling has the ability to determine this contribution and possibly yield further improvement in estimating necrotic volume, with an R^2 value of 0.91. Providing a seamless workflow from image processing to FEM mesh creation and

light modeling is essential in determining this correlation. Due to the presence of important structures in and around the pancreas, such as major blood vessels and the stomach wall, predicting the extent of necrosis is valuable in avoiding damage to these structures. Estimation of treatment response will also provide more confidence in treating the entire tumor, which will potentially improve the efficacy of this minimally invasive and nontoxic alternative to surgery for treating locally advanced cancer in the pancreas.

6. Recommendations for future work

The use of information derived from contrast CT to predict the extent of necrosis caused by photodynamic therapy has significant clinical potential. At a minimum, contrast-derived venous blood content as described in the work is an easily determined parameter which shows a high degree of correlation with necrotic volume. This could be used as a source of surrogate dosimetry information in pre-treatment planning for PDT. Using additional information from light modeling yields an improved correlation, but does introduce further complexity to the process. One source of possible error in using light modeling to create fluence maps around the fiber location is in the accuracy of the forward model used in NIRFAST as compared with the light-emitting fiber in the VERTPAC-01 trial, in terms of source strength and light profile. A study could be done to validate these parameters for the fiber used and ensure model accuracy.

It would be useful to investigate the applicability of these findings to other photosensitizers and in other types of cancer, to demonstrate consistency. The findings presented in this work demonstrate that in Verteporfin-based PDT of the pancreas, light attenuation dominates treatment response. This indicates that in the VERTPAC-01 trial it is likely that the photosensitizer was fairly evenly distributed within the pancreas. Studies focused on other types of cancer and photosensitizers would provide valuable information about the reliability of this phenomenon across different agents and organs. Another worthwhile inquiry would be a study like VERTPAC-01, with an added analysis of photosensitizer distribution. Other parameters which may affect the correlations found in this work include tumor volume, time between the photosensitizer administration and

treatment, tissue oxygenation, and photosensitizer dose given. It is likely that the clinical application of these dosimetry methods would benefit from a comprehensive case analysis. This analysis would choose treatment parameters based upon organ, tumor, photosensitizer, and optical properties, to ensure the effectiveness of the dosimetry methods.

7. Appendices

7.1 Appendix A: Scripts

Note that only code not distributed in version 8 of the NIRFAST package (nirfast.org) is shown below:

```
% PDT Simulations
% Michael Jermyn

%% The first two sections apply light modeling to each patient

%% homogeneous simulation used to determine light fluence maps for each
patient

mesh = load_mesh('seg1_nirfast_mesh');

% bulk values
mesh.mua(mesh.region==1) = mua_tissue;
mesh.mua(mesh.region==2) = mua_blood;
mesh.mus(mesh.region==1) = mus_tissue;
mesh.mus(mesh.region==2) = mus_blood;

data=femdata(mesh,100);
mesh.phi=sum(data.phi,2);
```

```
% scale field to total energy diffused
energy_total = 40*1; % energy in J/s/cm by fiber size in cm
% want integral(mesh.phi) = energy_total;
mesh.phi = mesh.phi.*energy_total/(sum(mesh.phi.*mesh.support/4));
% catch small negatives
mesh.phi(mesh.phi<0) = 0;

% display resulting field
plotmesh(mesh);

% save result
save_mesh(mesh,'result_mesh');


%% find bulk values using arterial/venous; the values here are
determined by looking at ROI grayscale values in contrast CT scans pre-
and post-treatment, for each patient

% average pre-contrast value
v_pre_blood = 84.4;
v_pre_tissue = 56.7;

v_post_blood_art = 297.9;
v_post_tissue_art = 59.4;

v_post_blood_ven = 111.6;
v_post_tissue_ven = 61.0;

% extinction coefficients at 690nm
E_water = 0.00046;
E_deoxyHb = 0.47256639;
E_HbO = 0.06356280;

% oxygen saturation
R_SO2_art = 0.99;
R_SO2_ven = 0.70;

% water concentration
C_water = 0.5;

% blood concentrations
v_blood_art = v_post_blood_art - v_pre_blood;
v_tissue_art = v_post_tissue_art - v_pre_tissue;

v_blood_ven = v_post_blood_ven - v_pre_blood;
v_tissue_ven = v_post_tissue_ven - v_pre_tissue;

% absorption
C_deoxyHb = (1-R_SO2_ven)*(v_tissue_ven/v_blood_ven) + (1-
R_SO2_art)*(v_tissue_art/v_blood_art);
C_HbO = R_SO2_ven*(v_tissue_ven/v_blood_ven) +
R_SO2_art*(v_tissue_art/v_blood_art);
mua_tissue = E_water*C_water + E_deoxyHb*C_deoxyHb + E_HbO*C_HbO;

C_deoxyHb = (1-R_SO2_ven) + (1-R_SO2_art);
C_HbO = R_SO2_ven + R_SO2_art;
mua_blood = E_water*C_water + E_deoxyHb*C_deoxyHb + E_HbO*C_HbO;
```

```
% scattering
mus_blood = 0.5;
mus_tissue = 0.98;
```

%% The below sections generate figures or data used for these figures which appear in the thesis (referred where applicable)

%% Normalized Energy vs Necrotic Volume

```
% energy (J/cm)
E = [5 5 5 10 10 10 20 20 20 40 40 40 40 40 40];
% fiber size (cm)
d = [1 1 1 1 1 1 1 1 1 1 1 1 2 1];
% number of fibers
n = [1 1 1 1 1 1 1 1 1 1 1 1 3 2];
% necrotic volume (cm^3)
V = [0 0 0 0.96 0.43 0 0.34 2.37 0.72 5.17 2.61 0 2.67 23.20 5.30];


x = n.*log(d.*E);
p = polyfit(x,V,1);
f = polyval(p,x);

figure
plot(x,V,'o','LineWidth',2,...
                'MarkerEdgeColor','k',...
                'MarkerFaceColor','r',...
                'MarkerSize',10);
hold on
plot(x,f,'-');
title('Normalized Energy vs Necrotic Volume','fontsize',14);
set(gca,'fontsize',14);
set(gcf,'color','white');
xlabel('normalized energy: n*log(d*E)','fontsize',14);
ylabel('volume of necrosis (cm^3)','fontsize',14);
```

%% Venous Blood Content vs Normalized Necrotic Volume (Fig 37b)

```
% energy (J/cm)
E = [10 10 10 20 20 40 40 40 40 40];
% fiber size (cm)
d = [1 1 1 1 1 1 1 1 2 1];
% number of fibers
n = [1 1 1 1 1 1 1 1 3 2];
% necrotic volume (cm^3)
V = [0.96 0.43 0 2.37 0.72 5.17 2.61 2.67 23.20 5.30];
%V = [1.19 0.43 0 2.37 0.72 5.17 2.61 2.67 23.20 5.75];
% venous blood content (%)
blood_ven = [34.09 60.90 73.28 36.49 52.03 3.59 37.00 37.80 12.13
15.81];
```

```
y = V./(n.*d.*log(E));

figure
plot(blood_ven,y,'o','LineWidth',2,...
                 'MarkerEdgeColor','k',...
                 'MarkerFaceColor','r',...
                 'MarkerSize',10);
%title('Venous Blood Content vs Necrotic Volume','fontsize',14);
set(gca,'fontsize',14);
set(gcf,'color','white');
xlabel('contrast derived venous blood content (%)','fontsize',14);
ylabel('necrotic volume per dose','fontsize',14);

[b,bint,r,rint,stats] = regress(y',[ones(size(blood_ven,2),1)
blood_ven']);
stats(1)
```

%% Venous Blood Content vs Raw Necrotic Volume (Fig 37a)

```
% energy (J/cm)
E = [10 10 10 20 20 40 40 40 40 40];
% fiber size (cm)
d = [1 1 1 1 1 1 1 1 2 1];
% number of fibers
n = [1 1 1 1 1 1 1 1 3 2];
% necrotic volume (cm^3)
V = [0.96 0.43 0 2.37 0.72 5.17 2.61 2.67 23.20 5.30];
% venous blood content (%)
blood_ven = [34.09 60.90 73.28 36.49 52.03 3.59 37.00 37.80 12.13
15.81];

y = V;

figure
hold on
plot(blood_ven(1:3),y(1:3),'o','LineWidth',2,...
                 'MarkerEdgeColor','k',...
                 'MarkerFaceColor','r',...
                 'MarkerSize',10);
plot(blood_ven(4:5),y(4:5),'o','LineWidth',2,...
                 'MarkerEdgeColor','k',...
                 'MarkerFaceColor','g',...
                 'MarkerSize',10);
plot(blood_ven(6:8),y(6:8),'o','LineWidth',2,...
                 'MarkerEdgeColor','k',...
                 'MarkerFaceColor','b',...
                 'MarkerSize',10);
plot(blood_ven(9),y(9),'o','LineWidth',2,...
                 'MarkerEdgeColor','k',...
                 'MarkerFaceColor','k',...
                 'MarkerSize',10);
plot(blood_ven(10),y(10),'o','LineWidth',2,...
                 'MarkerEdgeColor','k',...
                 'MarkerFaceColor','y',...
                 'MarkerSize',10);
%title('Venous Blood Content vs Necrotic Volume','fontsize',14);
```

```
set(gca,'fontsize',14);
set(gcf,'color','white');
xlabel('contrast derived venous blood content (%)','fontsize',14);
ylabel('necrotic volume (cm^3)','fontsize',14);

legend('10J/cm, one 1cm fiber',...
    '20J/cm, one 1cm fiber',...
    '40J/cm, one 1cm fiber',...
    '40J/cm, three 2cm fiber',...
    '40J/cm, two 1cm fiber');

[b,bint,r,rint,stats] = regress(y',[ones(size(blood_ven,2),1)
blood_ven']);
stats(1)
```

```
%% Arterial Blood Content vs Normalized Necrotic Volume

% energy (J/cm)
E = [10 10 10 20 20 40 40 40 40 40 40];
% fiber size (cm)
d = [1 1 1 1 1 1 1 1 1 2 1];
% number of fibers
n = [1 1 1 1 1 1 1 1 1 3 2];
% necrotic volume (cm^3)
V = [0.96 0.43 0 2.37 0.72 5.17 2.61 0 2.67 23.20 5.30];
% venous blood content (%)
blood_art = [7.86 7.99 8.33 7.73 15.24 0.92 6.68 0.36 2.18 0.61 1.26];

y = V./(n.*d.*log(E));

figure
plot(blood_art,y,'o','LineWidth',2,...
                 'MarkerEdgeColor','k',...
                 'MarkerFaceColor','r',...
                 'MarkerSize',10);
%title('Venous Blood Content vs Necrotic Volume','fontsize',14);
set(gca,'fontsize',14);
set(gcf,'color','white');
xlabel('contrast derived arterial blood content (%)','fontsize',16);
ylabel('necrotic volume per energy dose (cm^3/J)','fontsize',16);

[b,bint,r,rint,stats] = regress(y',[ones(size(blood_art,2),1)
blood_art']);
stats(1)
```

```
%% Threshold correlation between estimated and actual necrotic volume

hf = waitbar(0,'Loading meshes');

mesh1 = load_mesh('slab1'); % 1cm fiber
mesh2 = load_mesh('slab'); % 2cm fiber

mua = [0.069 0.119 0.142 0.073 0.107 0.008 0.074 0.151 0.072 0.088
0.031];
mus = 0.98;
```

```
volume_actual = [0.96 0.43 0 2.37 0.72 5.17 2.61 0 2.67 23.20 5.30];
fiber_size = [1 1 1 1 1 1 1 1 2 1];
num_fibers = [1 1 1 1 1 1 1 1 3 2];
energy = [10 10 10 20 20 40 40 40 40 40 40];

for i=1:size(mua,2)
    waitbar(0.1 + 0.9*i/size(mua,2),hf,['Simulation ' num2str(i) ' of '
num2str(size(mua,2))]);

    if fiber_size(i) == 1
        mesh{i} = mesh1;
    else
        mesh{i} = mesh2;
    end
    mesh{i}.mua(:) = mua(i);
    mesh{i}.mus(:) = mus;

    data=femdata(mesh{i},100);
    mesh{i}.phi=sum(data.phi,2);

    % scale field to total energy diffused
    energy_total = energy(i)*fiber_size(i); % energy in J/s/cm by fiber
size in cm
    % want integral(mesh.phi) = energy_total;
    mesh{i}.phi =
mesh{i}.phi.*energy_total/(sum(mesh{i}.phi.*mesh{i}.support/4));
    % catch small negatives
    mesh{i}.phi(mesh{i}.phi<0) = 0;
end

close(hf);


%% best correlation

threshold = 0.003;
mycolor = ['r'];
correlation = [];
figure
hold on

for i=1:size(threshold,2)
    volume_estimated = [];

    for j=1:size(mua,2)
        vol = 0.001*num_fibers(j)*sum(mesh{j}.support(mesh{j}.phi >
threshold(i))/4);
        volume_estimated = [volume_estimated vol];
    end




    x = volume_actual;
    y = volume_estimated;
    x(end-3) = [];
    y(end-3) = [];
```

```
    [b,bint,r,rint,stats] = regress(y',[ones(size(x,2),1) x']);
    correlation = [correlation stats(1)];
    plot(x,y,'o','LineWidth',1,...
                    'MarkerEdgeColor','k',...
                    'MarkerFaceColor',mycolor(i),...
                    'MarkerSize',7);

end

title('Estimated vs actual necrotic volume','fontsize',14);
set(gca,'fontsize',14);
set(gcf,'color','white');
xlabel('actual necrotic volume [cm^3]','fontsize',14);
ylabel('estimated necrotic volume [cm^3]','fontsize',14);
legend([num2str(threshold(1)) 'J, R^2 = ' num2str(correlation(1))]);


%% find best correlation

threshold = 0.001:0.002:0.010;
mycolor = ['r' 'g' 'b' 'k' 'y'];
correlation = [];
figure
hold on

for i=1:size(threshold,2)
    volume_estimated = [];

    for j=1:size(mua,2)
        vol = 0.001*num_fibers(j)*sum(mesh{j}.support(mesh{j}.phi >
threshold(i))/4);
        volume_estimated = [volume_estimated vol];
    end

    [b,bint,r,rint,stats] =
regress(volume_estimated',[ones(size(volume_actual,2),1)
volume_actual']);
    correlation = [correlation stats(1)];

    plot(volume_actual,volume_estimated,'o','LineWidth',1,...
                    'MarkerEdgeColor','k',...
                    'MarkerFaceColor',mycolor(i),...
                    'MarkerSize',7);

end

title('Estimated vs actual necrotic volume','fontsize',14);
set(gca,'fontsize',14);
set(gcf,'color','white');
xlabel('actual necrotic volume [cm^3]','fontsize',14);
ylabel('estimated necrotic volume [cm^3]','fontsize',14);
legend([num2str(threshold(1)) 'J, R^2 = ' num2str(correlation(1))],...
    [num2str(threshold(2)) 'J, R^2 = ' num2str(correlation(2))],...
    [num2str(threshold(3)) 'J, R^2 = ' num2str(correlation(3))],...
    [num2str(threshold(4)) 'J, R^2 = ' num2str(correlation(4))],...
    [num2str(threshold(5)) 'J, R^2 = ' num2str(correlation(5))]);
```

```
%% find best correlation continued

threshold = 0.0005:0.0005:0.014;
%threshold = 0.0001:0.0002:0.007;
correlation = [];

for i=1:size(threshold,2)
    volume_estimated = [];

    for j=1:size(mua,2)
        vol = 0.001*num_fibers(j)*sum(mesh{j}.support(mesh{j}.phi >
threshold(i))/4);
        volume_estimated = [volume_estimated vol];
    end

    v1 = volume_estimated;
    %v1(10)=[];
    v2 = volume_actual;
    %v2(10)=[];
    [b,bint,r,rint,stats] = regress(v1',[ones(size(v2,2),1) v2']);
    correlation = [correlation stats(1)];
end

figure
plot(threshold,correlation,'o','LineWidth',2,...
                    'MarkerEdgeColor','k',...
                    'MarkerFaceColor','r',...
                    'MarkerSize',8);
title('corelation between estimated and actual necrotic
volume','fontsize',14);
set(gca,'fontsize',14);
set(gcf,'color','white');
xlabel('energy threshold [J/cm^2]','fontsize',14);
ylabel('R^2','fontsize',14);


%% find best quantification

threshold = 0.0001:0.0001:0.004;
r = [];

for i=1:size(threshold,2)
    volume_estimated = [];

    for j=1:size(mua,2)
        vol = 0.001*num_fibers(j)*sum(mesh{j}.support(mesh{j}.phi >
threshold(i))/4);
        volume_estimated = [volume_estimated vol];
    end

    v1 = volume_estimated;
    %v1(10)=[];
    v2 = volume_actual;
    %v2(10)=[];
    r = [r sqrt(mean((v1-v2).^2))];
end
```

```
figure
plot(threshold,r,'o','LineWidth',2,...
                    'MarkerEdgeColor','k',...
                    'MarkerFaceColor','r',...
                    'MarkerSize',8);
title('RMS between estimated and actual necrotic
volume','fontsize',14);
set(gca,'fontsize',14);
set(gcf,'color','white');
xlabel('energy threshold [J/cm^2]','fontsize',14);
ylabel('RMS','fontsize',14);


%% correlation of log energy vs necrosis in Bown

energy = [240 320 480 160 240 160 80 80 40 320 240 320 320 240 320 160
280];
necrosis = [36 51 30 19 33 52 9 21 14 55 60 23 39 35 55 36 54];

energy = log(energy);

[b,bint,r,rint,stats] = regress(necrosis',[ones(size(energy,2),1)
energy']);
correlation = stats(1);

figure
plot(energy,necrosis,'o','LineWidth',1,...
                    'MarkerEdgeColor','k',...
                    'MarkerFaceColor','r',...
                    'MarkerSize',7);
title('Log Energy vs Necrotic Volume in Bown','fontsize',14);
set(gca,'fontsize',14);
set(gcf,'color','white');
xlabel('Log Total Energy Delivered [J]','fontsize',14);
ylabel('Necrotic Volume [cm^3]','fontsize',14);
legend(['R^2 = ' num2str(correlation)]);


%% correlation of log energy vs necrosis in Vertpac

energy = [80 240 40 40 40 40 20 20 20 10 10 10];
necrosis = [5.3 23.2 2.67 0 2.61 5.17 0.72 2.37 0.34 0 0.43 0.96];

energy = log(energy);

[b,bint,r,rint,stats] = regress(necrosis',[ones(size(energy,2),1)
energy']);
correlation = stats(1);

figure
plot(energy,necrosis,'o','LineWidth',1,...
                    'MarkerEdgeColor','k',...
                    'MarkerFaceColor','r',...
                    'MarkerSize',7);
title('Log Energy vs Necrotic Volume in Vertpac','fontsize',14);
set(gca,'fontsize',14);
```

```
set(gcf,'color','white');
xlabel('Log Total Energy Delivered [J]','fontsize',14);
ylabel('Necrotic Volume [cm^3]','fontsize',14);
legend(['R^2 = ' num2str(correlation)]);


%% venous value vs normalized necrotic volume (Fig 45)

% energy (J/cm)
E = [10 10 10 20 20 40 40 40 40 40 40];
% fiber size (cm)
d = [1 1 1 1 1 1 1 1 1 2 1];
% number of fibers
n = [1 1 1 1 1 1 1 1 1 3 2];
% necrotic volume (cm^3)
V = [0.96 0.43 0 2.37 0.72 5.17 2.61 0 2.67 23.20 5.30];
% venous blood content (%)
venous_blood = [110.1 197.3 106.7 104.0 128.7 153.6 139.9 129.4 148.7
137.5 116.11];
venous = [51.6 86.8 59.4 54.3 61.2 62.2 75.7 82.1 94.5 62.2 61.0];

y = V./(n.*d.*log(E));

figure
plot(venous,y,'o','LineWidth',2,...
                'MarkerEdgeColor','k',...
                'MarkerFaceColor','r',...
                'MarkerSize',10);
%title('Venous Blood Content vs Necrotic Volume','fontsize',14);
set(gca,'fontsize',14);
set(gcf,'color','white');
xlabel('venous grayscale value','fontsize',16);
ylabel('necrotic volume per energy dose (cm^3/J)','fontsize',16);

[b,bint,r,rint,stats] = regress(y',[ones(size(venous,2),1) venous']);
stats(1)


%% normalized venous value vs normalized necrotic volume (Fig 46)

% energy (J/cm)
E = [10 10 10 20 20 40 40 40 40 40 40];
% fiber size (cm)
d = [1 1 1 1 1 1 1 1 1 2 1];
% number of fibers
n = [1 1 1 1 1 1 1 1 1 3 2];
% necrotic volume (cm^3)
V = [0.96 0.43 0 2.37 0.72 5.17 2.61 0 2.67 23.20 5.30];
% venous blood content (%)
venous_blood = [110.1 197.3 106.7 104.0 128.7 153.6 139.9 129.4 148.7
137.5 116.11];
venous = [51.6 86.8 59.4 54.3 61.2 62.2 75.7 82.1 94.5 62.2 61.0];

venous = venous - venous_blood;

y = V./(n.*d.*log(E));
```

```
figure
plot(venous,y,'o','LineWidth',2,...
                'MarkerEdgeColor','k',...
                'MarkerFaceColor','r',...
                'MarkerSize',10);
%title('Venous Blood Content vs Necrotic Volume','fontsize',14);
set(gca,'fontsize',14);
set(gcf,'color','white');
xlabel('venous value - blood value','fontsize',16);
ylabel('necrotic volume per energy dose (cm^3/J)','fontsize',16);

[b,bint,r,rint,stats] = regress(y',[ones(size(venous,2),1) venous']);
stats(1)
```

References

[1] Hariharan D., Saied A., and Kocher H.M., "Analysis of mortality rates for pancreatic cancer across the world," HPB (Oxford), 10(1), 58-62 (2008).

[2] Howlader N., Noone A.M., Krapcho M., Neyman N., Aminou R., Altekruse S.F., Kosary C.L., Ruhl J., Tatalovich Z., Cho H., Mariotto A., Eisner M.P., Lewis D.R., Chen H.S., Feuer E.J., Cronin K.A., "SEER Cancer Statistics Review," National Cancer Institute (2012).

[3] Wilson B.C., and Patterson M.S., "The physics of photodynamic therapy," Phys. Med. Biol. 31, 327-360 (1986).

[4] Weishaupt K.R., Gomer C.J., and Dougherty T.J., "Identification of singlet oxygen as the cytotoxic agent in photo-inactivation of a murine tumor," Cancer Res. 36, 2325-2329 (1976).

[5] Barr H., Tralau C.J., Boulos P.B., MacRobert A.J., Tilly R., Bown S.G., "The contrasting mechanisms of colonic collagen damage between photodynamic therapy and thermal injury," Photochem. Photobiol. 46(5), 795-800 (1987).

[6] Dehghani H., Eames M.E., Yalavarthy P.K., Davis S.C., Srinivasan S., Carpenter C.M., Pogue B.W., and Paulsen K.D., "Near infrared optical tomography using NIRFAST: Algorithm for numerical model and image reconstruction," Communications in Numerical Methods in Engineering 25, 711-732 (2009).

[7] Carpenter C, et al., Inspired gas-induced vascular change in tumors with magnetic-resonance-guided near-infrared imaging: human breast pilot study, *In Journal of Biomedical Optics*, volume 15, 2010.

[8] Boas DA, Chen K, Grebert D, Franceschini MA. Improving the diffuse optical imaging spatial resolution of the cerebral hemodynamic response to brain activation in humans. *Optics Letters* 2004; 29(13):1506–1508.

[9] Zacharakis G, Kambara H, Shih H, Ripoll J, Grimm J, Saeki Y, Weissleder R, Ntziachristos V. Volumetric tomography of fluorescent proteins through small animals in vivo. *Proceedings of the National Academy of Sciences of the United States of America* 2005; 102:18252–18257.

[10] Arridge S. R. & Schweiger M. Image reconstruction in optical tomography. *Phil. Trans. R. Soc. Lond.* 1997; B 352, 717–726.

[11] Hebden J.C., Gibson A., Yusof R., Everdell N., Hillman E.C., Delpy D.T., Arridge S.A., Austin T., Meek J.H., and Wyatt J.S., "Three-dimensional optical tomography of the premature infant brain," Physics in Medicine and Biology, vol. 47(23), 4155 (2002).

[12] Gibson A.P., Hebden J.C., and Arridge S.R., "Recent advances in diffuse optical imaging," Physics in Medicine and Biology, vol. 50, R1-R43 (2005).

[13] Srinivasan S., Pogue B.W., Jiang S., Dehghani H., Kogel C., Soho S., Gibson J.J., Tosteson T.D., Poplack S.P., and Paulsen K.D., "Interpreting Hemoglobin and Water Concentration, Oxygen Saturation and Scattering Measured In Vivo by Near-Infrared Breast Tomography," PNAS, vol. 100, 12349-12354 (2003).

[14] Davis S.C., Pogue B.W., Dehghani H., and Paulsen K.D., "Contrast-detail analysis characterizing diffuse optical fluorescence tomography image reconstruction," Journal of Biomedical Optics Letters, vol. 10(5), 050501 (2005).

[15] Milstein A.B., Oh S., Webb K.J., Bouman C.A., Zhang Q., Boas D.A., and Millane R.P., "Fluorescence optical diffusion tomography," Applied Optics, vol. 42(16), 3081-3094 (2003).

[16] Hoyert D.L., and Xu J., "Deaths:Preliminary Data for 2011," National Vital Statistics Reports, vol. 61(6) (2012).

[17] Bown S.G., Rogowska A.Z., Whitelaw D.E., Lees W.R., Lovat L.B., Ripley P., Jones L., Wyld P., Gillams A., Hatfield W.R., "Photodynamic therapy for cancer of the pancreas," Gut 50(4), 549-557 (2002).

[18] Raab O., "Uber die Wirkung Fluoreszierender Stoffe auf Infusorien," Z. Biol., 39, 524-546 (1900).

[19] Tappeiner H. von, Jesionek A., "Therapeutische Versuche Mit Fluoreszierenden Stoffen," Muench. Med. Wochenschr, 47, 2042-2044 (1903).

[20] Prime J., "Les Accidentes Toxiques Par L'eosinate de Sodium," Jouve & Boyer, Paris (1900).

[21] Hausman W., "Die sensibilisierende wirkung des hematoporphyrins," Biochem. Z., vol. 30, 276 (1911).

[22] Figge F.H., Weiland G.S., "The Affinity of Neoplastic Embryonic and Traumatized Tissue for Porphyrins and Metalloporphyrins," Anat. Rec., vol. 100, 659 (1948).

[23] Dougherty T.J., Kaufman J.E., Goldfarb A., Weishaupt K.R., Boyle D., and Mittleman A., "Photoradiation Therapy for the Treatment of Malignant Tumors," Cancer Res., vol. 38, 2628-2635 (1978).

[24] Huggett M.T., Jermyn M., Gillams A., Mosse S., Kent E., Bown S.G., Hasan T., Pogue B.W., Pereira S.P., "Photodynamic therapy of locally advanced pancreatic cancer (VERTPAC study): final clinical results," SPIE Proc. Paper 8568-49 (2013).

[25] Chen B., Pogue B.W., Goodwin I.A., O'Hara J.A., Wilmot C.M., Hutchins J.E., Hoopes P.J., and Hasan T. "Blood flow dynamics after photodynamic therapy with verteporfin in the RIF-1 tumor," Radiation research. 160(4)**:** 452-9 (2003).

[26] Samkoe K.S., Chen A., Rizvi I., O'Hara J.A., Hoopes P.J., Pereira S.P., Hasan T., Pogue B.W. "Imaging tumor variation in response to photodynamic therapy in pancreatic cancer xenograft models," International journal of radiation oncology, biology, physics. 76(1)**:** 251-9 (2010).

[27] Patterson M.S., Wilson B.C., and Graff R., "In vivo tests of the concept of photodynamic threshold dose in normal rat liver photosensitized by aluminum chlorosulphonated phthalocyanine," Photochem. and Photobiol. 51(3), 343-349 (1990).

[28] Ligle L., Wilson B.C., "Photodynamic therapy of intracranial tissues: a preclinical comparative study of four different photosensitizers," J. Clin. Laser Med. Surg., 16, 81-91 (1998).

[29] Orenstein A., Kostenich G., Roitman L., Shechtman Y., Kopolovic Y., Ehrenberg B., and Malik Z., "A comparative study of tissue distribution and photodynamic therapy selectivity of chlorin e_6, Photofrin II and ALA-induced protoporphyrin IX in a colon carcinoma model," British Journal of Cancer, 73, 937-944 (1996).

[30] Farrell T.J., Wilson B.C., Patterson M.S., Olivo M.C., "Comparison of the in vivo photodynamic threshold dose for photofrin, mono- and tetrasulfonated aluminum phthalocyanine using a rat liver model," Photochem. Photobiol., 68(3), 394-9 (1998).

[31] van Gemert J.C., Berenbaum M.C., Gijsberg G.H.M., "Wavelength and light-dose dependence in tumour phototherapy with haematoporphyrin derivative," Br. J. Cancer 52, 43-49 (1985).

[32] Berenbaum M.C., Bonnett R., and Scourides P.A., "In vivo biological activity of the components of haematoporphyrin derivative," Br. J. Cancer 45, 571-581 (1982).

[33] Potter W.R., "PDT dosimetry and response," Photodynamic Therapy: Mechanisms (SPIE), 88-99 (1989).

[34] MeshLab, http://meshlab.sourceforge.net.

[35] Materialise: Mimics, http://biomedical.materialise.com/mimics.

[36] Hp-FEM: Netgen, http://www.hpfem.jku.at/netgen.

[37] UC Berkeley: Distmesh, http://persson.berkeley.edu/distmesh.

[38] Iso2mesh, http://iso2mesh.sourceforge.net/cgi-bin/index.cgi.

[39] Cornell: QMG, http://www.cs.cornell.edu/home/vavasis/qmg-home.html.

[40] Washington University: MCML, http://oilab.seas.wustl.edu/mc.html.

[41] UCL: TOAST, http://web4.cs.ucl.ac.uk/research/vis/toast/index.html.

[42] NIRx: NAVI, http://www.nirx.net/software/navi.

[43] COMSOL: Multiphysics, http://www.comsol.com/comsol-multiphysics.

[44] Jermyn M., Pogue B.W., Ghadyani H., Davis S.C., Mastanduno M., and Dehghani H., "A User-Enabling Visual Workflow for Near-Infrared Light Transport Modeling in Tissue," Biomedical Optics, OSA Technical Digest, paper BW1A.7 (Optical Society of America, 2012).

[45] Xu H., Springett R., Dehghani H., Pogue B.W., Paulsen K.D., and Dunn J.F., "MRI coupled Broadband Near Infrared Tomography System for Small Animal Brain Studies," Applied Optics, vol. 44(11), 2177-2188 (2005).

[46] Davis S.C., Pogue B.W., Springett R., Leussler C., Mazurkewitz P., Tuttle S.B., Gibbs-Strauss S.L., Jiang S.S., Dehghani H., and Paulsen K.D., "Magnetic resonance-coupled fluorescence tomography scanner for molecular imaging of tissue," Rev. Sci. Instrum., vol. 79(6), 064302 (2008).

[47] Kepshire D., Mincu N., Hutchins M., Gruber J., Dehghani H., Hypnarowski J., Leblond F., Khayat M., and Pogue B.W., "A microcomputed tomography guided fluorescence tomography system for small animal molecular imaging," Rev. Sci. Instrum., vol. 80(4), 043701 (2009).

[48] Tichauer K.M., Holt R.W., Samkoe K.S., El-Ghussein F., Gunn J.R., Jermyn M., Dehghani H., Leblond F., and Pogue B.W., "Computed tomography-guided time-domain diffuse fluorescence tomography in small animals for localization of cancer biomarkers," J. Vis. Exp., vol. 65, Jul. 17 (2012).

[49] Dehghani H., Pogue B.W., Poplack S.P., and Paulsen K.D., "Multiwavelength three-dimensional near-infrared tomography of the breast: initial simulation, phantom, and clinical results," Applied Optics, vol 42(1), 135-145 (2003).

[50] Leung T.S., Tachtsidis I., Smith M., Delpy D.T., and Elwell C.E., "Measurement of the absolute optical properties and cerebral blood volume of the adult human head with hybrid differential and spatially resolved spectroscopy," Physics in Medicine and Biology, vol. 51, 703-717 (2006).

[51] Schweiger M., and Arridge S., "Comparison of two- and three-dimensional reconstruction methods in optical tomography," Appl. Opt., vol. 37, 7419-7428 (1998).

[52] Jermyn M., Ghadyani H., Mastanduno M.A., Turner W., Davis S.C., and Pogue B.W., "Fast segmentation and high-quality three-dimensional volume mesh creation from medical images for diffuse optical tomography," J. Biomed. Opt. 18(8), 086007 (August 12, 2013), doi: 10.1117/1.JBO.18.8.086007.

[53] Krishnan K., Ibanez L., Turner W.D., Jomier J., and Avila R.S., "An open-source toolkit for the volumetric measurement of CT lung lesions," Optics Express, vol. 18(14), 15256-15266 (2010).

[54] Hartigan J., and Wong M., "Algorithm AS 136:A K-Means Clustering Algorithm," Journal of the Royal Statistical Society, vol. 28(1), 100-108 (1979).

[55] Sled J.G., Zijdenbos A.P., and Evans A.C., "A Nonparametric Method for Automatic Correction of Intensity Nonuniformity in Data," IEEE Transactions on Medical Imaging, vol. 17(1) (1998).

[56] Tustison N.J., Avants B.B., Cook P.A., Zheng Y., Egan A., Yushkevich P.A., and Gee J.C., "N4ITK: Improved N3 Bias Correction," IEEE Transactions on Medical Imaging, vol. 29(6), 1310-1320 (2010).

[57] Sezgin M., and Sankur B., "Survey over image thresholding techniques and quantitative performance evaluation," Journal of Electronic Imaging, vol. 13(1), 146-165 (2004).

[58] Serra J., and Soille P., "Mathematical Morphology and Its Applications to Image Processing," Proc. 2nd International Symposium on Mathematical Morphology (1994).

[59] Computational Geometry Algorithms Library (CGAL), http://www.cgal.org.

[60] Paul Chew L., "Guaranteed-quality mesh generation for curved surfaces," SCG Proceedings of the 9th annual symposium on Computational Geomotry, 274-280 (1993).

[61] Jean-Daniel Boissonnat, and Oudot S.. "Provably good sampling and meshing of surfaces," Graphical Models, 67:405-451 (2005).

[62] Oudot S., Rineau L., and Yvinec M.. "Meshing volumes bounded by smooth surfaces," In Proc. 14th International Meshing Roundtable, pages 203-219 (2005).

[63] Klingner M., "Improving Tetrahedral Meshes," Ph.D. Thesis, Department of Electrical Engineering and Computer Sciences, University of California, Berkeley (2008).

[64] Davis S.C., Samkoe K.S., O'Hara J.A., Gibbs-Strauss S.L., Payne H.L., Hoopes J., Paulsen K.D., and Pogue B.W., "MRI-coupled fluorescence tomography quantifies EGFR activity in brain tumors," Academic Radiology, vol. 17(3), 271-276 (2010).

[65] Materialise; Mimics, http://biomedical.materialise.com/mimics.

[66] Mastanduno M., Jiang S., DiFlorio-Alexander R., Pogue B.W., and Paulsen K.D., "Remote positioning optical breast magnetic resonance coil for slice-selection during image-guided near-infrared spectroscopy of breast cancer," J Biomed Opt., vol. 16(6), 066001 (2011).

[67] Dehghani H., Pogue B.W., Jiang S., Brooksby B., and Paulsen K.D., "Three-dimensional optical tomography: resolution in small-object imaging," Applied Optics, vol. 42(16), 3117 (2003).

[68] Jermyn M., Davis S.C., Dehghani H., Huggett M., Hasan T., Pereira S.P., and Pogue B.W., "Photodynamic therapy light dose analysis of a patient based upon arterial and venous contrast CT scan information," SPIE Proc. Paper 8568-10 (2013).

[69] Medical Expo, www.medicalexpo.com, COOK Medical Biliary Stent (April 2013).

[70] Boston Scientific, www.boston-scientific-international.com, WallFlex RX Biliary Stent (April 2013).

[71] Baele P.L., McMichan J.C., Marsh H.M., Sill J.C., and Southorn P.A., "Continuous monitoring of mixed venous oxygen saturation in critically ill patients," Anesth. Analg. 61(6), 513-517 (1982).

[72] Miller M., "Tissue oxygenation in clinical medicine: an historical review", Anesth. Analg. 61(6), 527-535 (1982).

[73] Huckabee W., "Metabolic consequences of chronic hypoxia," Ann NY Acad Sci 121, 723-730 (1965).

[74] Stainsby W., Otis A., "Blood flow, blood oxygen tension, oxygen uptake and oxygen transport in skeletal muscle," Am J Physiol 206, 858-866 (1964).

[75] "Understanding continuous mixed venous oxygen saturation (SvO2) monitoring with the swan-ganz oximetry TD system," Edwards Lifesciences, 2nd Ed. (2002).

[76] Wilson R.H., Chandra M., Scheiman J., Simeone D., McKenna B., Purdy J., and Mycek M., "Optical spectroscopy detects histological hallmarks of pancreatic cancer," Optics Express 17 (20), 17502 (2009).

[77] Sandell J.L, and Zhu T.C., "A review of in-vivo optical properties of human tissues and its impact on PDT," Journal of Biophotonics 4(11-22), 773-787 (2011).

[78] Cheong W., Prahl S.A., and Welch S.J., "A review of the optical properties of biological tissues," IEEE Journal of Quantum Electronics 26(12), 2166 (1990).

[79] Pedersen G.D., McCormick N.J., and Reynolds L.O., "Transport calculations for light scattering in blood," Biophys. J. 16, 199-207 (1976).

[80] Adams R., and Bischof L., "Seeded region growing," IEEE Trans. On Pattern Analysis and Machine Intelligence, 16(6), 641-647 (1994).

[81] Canny J., "A computational approach to edge detection," IEEE Trans. On Pattern Analysis and Machine Intelligence," 8:679-714, (1986).

[82] Malladi R., Sethian J., and Vemuri B., "Shape Modeling with Front Propagation: A Level Set Approach," IEEE Trans. On Pattern Analysis and Machine Intelligence, 17(2), 158-175 (1995).